BIOMEDICAL APPLICATIONS OF SHARKSKIN MIMICKED POLYMERIC MEMBRANES

by

Sabra Rostami

B. S. in Chemical Engineering, Sahand University of Technology, 2012

M. S. in Biomedical Engineering, Bogaziçi University, 2016

Submitted to the Institute of Biomedical Engineering

in partial fulfillment of the requirements

for the degree of

Doctor

of

Philosophy

Boğaziçi University

2022

BIOMEDICAL APPLICATIONS OF SHARKSKIN MIMICKED POLYMERIC MEMBRANES

APPROVED BY:

Assoc. Prof. Dr. Bora Garipcan ..... (Thesis Advisor)

Assoc. Prof. Dr. Ahmet İlker Tekkeşin .....

Assoc. Prof. Dr. Özgür Kocatürk .....

Assoc. Prof. Dr. Utku Kürşat Ercan .....

Assist. Prof. Dr. Banu İyisan .....

DATE OF APPROVAL: 01 April 2022

Part of the journey is the end...

Tony Stark

ACKNOWLEDGMENTS

I would like to express my utmost thanks and sincere gratitude to my supervisor, Dr. Bora Garipcan for his continuous support, patience, and guidance that inspired me all the way. You helped me to find the true extent of my abilities and allowed me to learn how to be a true scientist. Your constitutive criticisms in every research project I was involved in were instrumental and encouraging.

I extend my thanks and gratitude to Dr. Ahmet İlker Tekkeşin, Dr. Utku Kürşat Ercan, Dr. Özgür Kocatürk, and Dr. Banu İyisan for their contributions and guidance. The studies in this thesis were supported by funds from the Scientific and Research Council of Turkey (TUBITAK) (grant number 117R055) and Bogaziçi University Research Fund (grant number 6701). Much gratitude goes to my colleagues. To Gizem Dilara Özdemir and Gencay Yasav, thank you for your friendship, your hospitality, and for all the wonderful memories. To my dearest friends Roya, Altay, Nasim, Sepideh, Sevil, Metehan, Naghme, and Shabnam, I am and forever will be deeply grateful for having you guys. Thank you for your unwavering support and friendship, constant encouragement, and life-lasting memories.

To Ulduz and Ali, you two have always been my role models. Thank you for every advice you have ever given me and for every single minute, you spent with me.

Last and most important of all, I have to thank my parents for their endless love, support, and encouragement throughout my life. Thank you both for believing in me, giving me the strength to reach for the stars, pursue my dreams and thrive in every aspect of my life. Thank you for being right by my side every step of the way and reminding me that I can do anything as long as I keep pushing myself and concentrate on all positive aspects of life. You are the reason for who I am today, and I dedicate this thesis to you both with all my heart and soul. I love you both more than life itself.

ACADEMIC ETHICS AND INTEGRITY STATEMENT

I, Sabra Rostami, hereby certify that I am aware of the Academic Ethics and Integrity Policy issued by the Council of Higher Education (YÖK) and I fully acknowledge all the consequences due to its violation by plagiarism or any other way.

Name :

Signature:

Date:

ABSTRACT

BIOMEDICAL APPLICATIONS OF SHARKSKIN MIMICKED POLYMERIC MEMBRANES

Infection is one of the biggest challenges of implantable biomaterials. The difficulty of eliminating implant-associated infection imposes a huge burden onto the patient's life quality aside from the considerable financial cost of the treatment. Thus, effective approaches must be explored to design biomaterials with enhanced antibacterial activity. Sharks have been investigated via biomimetic and bioinspiration approaches and discoveries have shown that sharkskin possess antibacterial effects due to reduced drag force on the skin whilst swimming which is because of their skin's surface micro-structure . In this thesis the antibacterial properties of sharkskin mimicked polymeric membranes in static conditions, with and without the aid of antibacterial and bactericidal chemicals was studied. The aim was to understand the adhesion behavior of both bacteria and mammalian cells onto the biomimicked polymeric membranes and how the surface topography affected these properties. Moreover, the impact of surface topography on drug release and bactericidal activity of these membranes was investigated by examining the physicochemical, antibacterial, and cytocompatibility properties of fabricated membranes. *In vitro* experiments were conducted to evaluate cellular responses of mammalian cells along with bactericidal properties using human keratinocyte (HaCaT), mouse fibroblast (L929), and human dermal primary fibroblast (HDFa) cell lines as model cells and Gram-negative *Escherichia coli* and Gram-positive *Staphylococcus aureus* bacterial strains as model bacteria species. The results presented in this thesis show that sharkskin polymeric membranes have great potential for reducing bacterial biofilm formation most probably via preventing bacterial adhesion. Also, the cell adhesion on these membranes can be enhanced via chemical modifications.

Keywords: Sharkskin, Biomimetic, Antibacterial, Cytocompatibility, Chitosan, Graphene Oxide, Ampicillin Sodium Salt, Caffeic Acid Phenethyl Ester.

ÖZET

KÖPEKBALIĞI DERİSİ TAKLİT EDİLEN MEMBRANLARIN BİYOMEDİKAL UYGULAMALARI

Enfeksiyon, implante edilebilir biyomalzemelerin karşılaştığı en büyük sorunlardan birisidir. İmplanta bağlı enfeksiyonu ortadan kaldırmanın zorluğu, tedavinin önemli ekonomik maliyetinin yanı sıra hastanın yaşam kalitesine de büyük bir yük getirmektedir. Bu nedenle, geliştirilmiş antibakteriyel biyomalzemeler tasarlamak için etkili yaklaşımlar araştırılmaktadır. Köpekbalığı derisi, biyotaklit ve biyoesinlenme yaklaşımlarıyla araştırılmış ve yapılan çalışmalar, yüzerken derinin yüzey mikro yapısı nedeniyle sürtünme kuvvetini azaltmasından kaynaklı, antibakteriyel etki gösterdiği bulunmuştur. Bu tezde, köpekbalığı derisi taklitli polimerik membranların statik koşullarda antibakteriyel ve bakterisidal kimyasalların yardımı ile ve yardımı olmadan antibakteriyel özellikleri incelenmiştir. Tezin amacı ise, bakterilerin ve memeli hücrelerinin biyotaklit edilen polimerik membranlar üzerine yapışma davranışını ve yüzey topografyasının etkisi araştırılmasıdır. Ayrıca, yüzey topografisinin bu membranların ilaç salımı ve bakterisidal aktivitesi üzerindeki etkisi, üretilen membranların fizikokimyasal, antibakteriyel ve sitouyumluluk özellikleri incelenmiştir. Model hücreler olarak insan keratinositi (HaCaT), fare fibroblastı (L929) ve insan dermal primer fibroblast (HDFa) hücreleri ve model bakteri türleri olarak Gram-negatif *Escherichia coli* ve Gram pozitif *Staphylococcus aureus* bakteri suşları kullanılarak, memeli hücrelerinin hücresel tepkilerinin yanı sıra bakterisidal özelliklerin değerlendirilmesi için *in vitro* deneyler yapılmıştır. Sunulan tezin sonuçları, köpekbalığı derisi taklit polimerik membranlarının, büyük olasılıkla bakteriyel yapışmayı önleyerek bakteriyel biyofilm oluşumunu azaltmak için bir potansiyele sahip olduğunu göstermektedir. Ayrıca bu membranlar üzerindeki hücre yapışması kimyasal modifikasyonlar ile ayarlanabildiği gösterilmiştir.

Anahtar Sözcükler: Köpekbalığı Derisi, Biyo-taklit, Antibakteriyel, Sitouyumluluk, Kitosan, Grafen Oksit, Ampisilin Sodyum Tuzu, Kafeik Asit Fenetil Ester

TABLE OF CONTENTS

ACKNOWLEDGMENTS iv
ACADEMIC ETHICS AND INTEGRITY STATEMENT v
ABSTRACT vi
ÖZET vii
LIST OF FIGURES xii
LIST OF TABLES xx
LIST OF SYMBOLS xxi
LIST OF ABBREVIATIONS xxii
1. INTRODUCTION 1
1.1 Motivation 2
1.2 Objectives and Outline 5
2. BACKGROUND 7
2.1 Sharkskin: Anatomy and Characteristics 7
2.2 Bacterial Colonization and Biofilm Formation on Surfaces: A Short Summary of Mechanisms and Impacts 9
2.2.1 Bacterial Biofilm: Structure and Properties 10
2.2.2 Implant Associated Bacterial Infection 11
2.3 Sharkskin Patterned Surfaces: Methods of Fabrication and Their Antibacterial, Anti-Biofouling and Other Biological Properties 13
2.4 Sharkskin Bioinspired Surfaces: Fabrication and Bio-fouling Properties 14
2.4.1 Marine Biofouling on Sharkskin Bioinspired Surfaces 14
2.4.2 Bacterial Adhesion on Sharkskin Bioinspired Surfaces: Mere Effect of Topography 15
2.4.3 Bacterial Adhesion on Sharkskin Bioinspired Surfaces: Dual Effect of Topography and Chemistry 17
2.4.4 Sharkskin Bioinspired Surfaces: Potentials of Usage in Medical Instruments 18
2.4.5 Sharkskin Bioinspired Surfaces: Adhesion of Viruses and Mammalian Cells 20

2.5 Sharkskin Biomimicked Surfaces 22
2.5.1 Antibacterial Activities of Sharkskin Biomimicked Surfaces . . . 23
2.5.2 Medical Applications of Sharkskin Biomimicked Surfaces 25
2.6 Surface Associated Infection 27
2.7 Chitosan 28
2.8 Graphene Oxide 29
2.9 Caffeic acid phenethyl ester (CAPE) 30
2.10 Ampicillin Sodium Salt 30
3. BIFUNCTIONAL SHARKSKIN MIMICKED CHITOSAN/GRAPHENE OXIDE MEMBRANES: REDUCED BIOFILM FORMATION AND IMPROVED CYTOCOMPATIBILITY 32
3.1 Experimental 32
3.1.1 Materials 32
3.1.2 Preparation of Chitosan-Based Membrane 32
3.1.3 Fourier-Transform Infrared Spectroscopy (FTIR) 34
3.1.4 Water Contact Angle (WCA) 34
3.1.5 L929 and HaCaT Cell Culture on Plain Membranes 34
3.1.5.1 Cell Viability (MTT Assay) 35
3.1.5.2 Cell Proliferation (AlamarBlue Assay) 35
3.1.5.3 Immunofluorescent (IF) Staining 36
3.1.6 Bacterial Culture Tests 36
3.1.6.1 Antibacterial Activity Test (ISO 22196) 36
3.1.6.2 Bacterial Biofilm Formation (MTT Assay) 36
3.1.6.3 Morphology of Adhered Bacteria 37
3.1.7 L929 and HaCaT Cell Culture on Sharkskin Mimicked Membranes 37
3.1.8 Statistical Analysis 38
3.2 Results 38
3.2.1 FTIR and Water Contact Angle 38
3.2.2 L929 and HaCaT Cell Culture on Plain Membranes 39
3.2.3 Bacterial Culture Tests 42
3.2.3.1 ISO 22196 Test 42
3.2.3.2 Biofilm Growth (MTT assay) 44

3.2.3.3 Biofilm Morphology 47
3.2.4 Mammalian Cell Culture on Sharkskin Mimicked Membranes . . 48
3.2.5 Morphology of Adhered Cells 50
3.3 Discussion 54
4. BIOMIMETIC SHARKSKIN SURFACES WITH ANTIBACTERIAL, CYTO-COMPATIBILE, AND DRUG DELIVERY PROPERTIES 59
4.1 Experimental 59
4.1.1 Materials 59
4.1.2 Preparation of Sharkskin Biomimicked Membranes 60
4.1.3 Physicochemical Characterization 60
4.1.3.1 Swelling Ratio 62
4.1.3.2 X-Ray Photoelectron Spectroscopy (XPS) 62
4.1.3.3 FTIR 62
4.1.3.4 Tensile Strength 63
4.1.3.5 Atomic Force Microscopy (AFM) 63
4.1.4 Drug Release Rate 63
4.1.5 Zone of Inhibition 63
4.1.6 Bacterial Studies 64
4.1.6.1 Biofilm Growth (MTT Assay) 64
4.1.6.2 Morphology of Bacterial Adhesion 64
4.1.7 HDFa and HaCaT Cell Culture 65
4.1.7.1 Cell Viability (MTT Assay) 65
4.1.7.2 Cell Proliferation (AlamarBlue Assay) 65
4.1.7.3 HDFa and HaCaT Cell Morphology 66
4.1.8 *In vitro* Enzymatic Degradation 66
4.1.9 Statistical Analysis 67
4.2 Results 67
4.2.1 Chemical and Mechanical Characterization 67
4.2.2 Drug Release and Zone of Inhibition 73
4.2.3 Bacterial Biofilm Growth (MTT assay) and Morphology 77
4.2.4 HDFa and HaCaT Cell Culture Tests 84
4.2.5 *In vitro* Enzymatic Degradation 85

4.3 Discussion 91
5. CONCLUSION 99
REFERENCES 101

LIST OF FIGURES

Figure 2.1 **A)** Layers of sharkskin [73]; **B)** Shape and dimensions of the a single blacktip *Carcharhinus limbatus* shark's skin denticle (B, base; BL, base length; BW, base width; C, crown; CL, crown length; CW, crown width; N, neck; RS, riblet spacing) [73]; **C)** Sharkskin morphology at different regions on shark's body [74]. 8

Figure 2.2 **A)** Illustration of stages of full thickness bacterial biofilm formation (Created in Biorender.com); **B)** Various surfaces of implantable medical devices prone to bacterial biofilm formation (Created in Biorender.com). 12

Figure 2.3 **A)** Sharklet micropatterns and the bead transfer method; **B)** Transfer of *S. aureus* on silicone surfaces (*** $p < 0.001$; **** $p < 0.0001$); **C)** Transfer of *Bacteriophage T4* on silicone surfaces. Smooth or SK2x2 micropatterned silicone samples were tested against *Bacteriophage T4* using beads transfer method; **D-E)** Transfer of human viruses on silicone surfaces [125]. 21

Figure 2.4 **A)** SEM images of algal cells adhered onto the surfaces of flat PDMS (F-PDMS) surfaces after being immersed in the Pearl River for various durations. (a) 1 day, (b) 21 days, (c) 70 days, (d) after being washed [27]; **B)** SEM images of algal cells adhered onto the biomimetic shark skin PDMS (S-PDMS) surfaces post immersion in the Pearl River for various durations. (a) 7 days, (b) 21 days, (c) 70 days, (d) after being washed [27]. 24

Figure 2.5 **A)** SEM (upper) and CLSM (lower) images of the Mako shark skin surface at different body locations; **B)** The residual biofilm of (a) *S. aureus* and (b) *E. coli* was quantified by crystal-violet staining; **C)** Investigation of biofilm formation by (a) *S. aureus* and (b) *E. coli* on smooth and biomimetic shark skin surfaces. Scale bar = 100 μm [127]. 25

Figure 2.6 **A)** SEM images of the actual skin topography of *Etmopterus Lucifer* (a), *Alopias superciliosus* (b), and *Prionace glauca* sharks (c), Biomimicked PDMS surfaces with microtopography of *Etmopterus Lucifer* (d), *Alopias superciliosus* (e), and *Prionace glauca* (f) [130]; **B)** *E. coli* adhesion on the surface of (a) *Alopias superciliosus*, (b) *Prionace glauca* and (c) *Etmopterus Lucifer* and (d) pristine PDMS membrane [130]. 27

Figure 3.1 Schematic representation of overall experimental procedures. 33

Figure 3.2 FTIR spectra of CH, GO and GOc membranes (CH: chitosan, GO2: 0.2%wt graphene oxide/chitosan nanocomposite, GOc: graphene oxide coated chitosan). 39

Figure 3.3 Water contact angle results for plain and sharkskin mimicked membranes (Mean ± SD, n=5) (CH: chitosan, GO: graphene oxide, GO1, GO2, GO3: 0.1, 0.2, 0.3 %wt graphene oxide/chitosan nanocomposites, GOc: graphene oxide coated) 40

Figure 3.4 Cell culture results of HaCaT and L929 on plain membranes. **A)** Cell viability of HaCaT on plain membranes (MTT assay), **B)** Cell viability of L929 on plain membranes (MTT assay), (Mean ± SD, n=4; CH: chitosan, GO1, GO2, GO3: 0.1, 0.2 and 0.3%wt graphene oxide/chitosan nanocomposite, GOc: graphene oxide coated chitosan) 41

Figure 3.5 Cell culture results of HaCaT and L929 on plain membranes. **A)** Cell proliferation of HaCaT on plain membranes (AlamarBlue assay), **B)** Cell proliferation of L929 on plain membranes (AlamarBlue assay), (Mean ± SD, n=4; CH: chitosan, GO1, GO2, GO3: 0.1, 0.2 and 0.3%wt graphene oxide/chitosan nanocomposite, GOc: graphene oxide coated chitosan) 41

Figure 3.6 IF staining images of HaCaT and L929 cells stained with Alexa Fluor 488 phalloidin (green) and DAPI (blue) on day 3. Scale bars: 200μm and 50μm. 43

Figure 3.7 ISO 22196 test results, **A)** *E. coli*, **B)** *S. aureus*, (Mean ± SD, p<0.05, n=4; CH: chitosan, GO2: 0.2 %wt graphene oxide/chitosan nanocomposite, GOc: graphene oxide coated chitosan, GO2c: graphene oxide coated 0.2 %wt graphene oxide/chitosan nanocomposite) 45

Figure 3.8 Bacterial biofilm growth on plain and sharkskin mimicked membranes (MTT assay) **A)** *E. coli*, **B)** *S. aureus*, (Mean ± SD, p<0.05, n=4; CH: chitosan, GO2: 0.2 %wt graphene oxide/chitosan nanocomposite, GOc: graphene oxide coated chitosan, GO2c: graphene oxide coated 0.2 %wt graphene oxide/chitosan nanocomposite) 46

Figure 3.9 SEM images of *E. coli* on membranes. Scale bars: 50μm and 10μm (CH: chitosan, GO2: 0.2 %wt graphene oxide/chitosan nanocomposite, GOc: graphene oxide coated chitosan, GO2c: graphene oxide coated 0.2 %wt graphene oxide/chitosan nanocomposite). 47

Figure 3.10 SEM images of *S. aureus* on membranes. Scale bars: 50μm and 10μm (CH: chitosan, GO2: 0.2 %wt graphene oxide/chitosan nanocomposite, GOc: graphene oxide coated chitosan, GO2c: graphene oxide coated 0.2 %wt graphene oxide/chitosan nanocomposite). 48

Figure 3.11 HaCaT and L929 cell culture tests results on sharkskin mimicked membranes. **A)** Cell viability of HaCaT on Sharkskin mimicked membranes (MTT assay), **B)** Cell viability of L929 on Sharkskin mimicked membranes (MTT assay) (Mean ± SD, p<0.05, n=4; CH: chitosan, GO2: 0.2 %wt graphene oxide/chitosan nanocomposite, GOc: graphene oxide coated chitosan, GO2c: graphene oxide coated 0.2 %wt graphene oxide/chitosan nanocomposite). 49

Figure 3.12 Cell culture results of HaCaT and L929 on SSM membranes. **A)** Cell proliferation rate of HaCaT on SSM membranes (AlamarBlue assay), **B)** Cell proliferation rate of L929 on SSM membranes (AlamarBlue assay), (Mean ± SD, $p<0.05$, n=4; CH: chitosan, GO2: 0.2 %wt graphene oxide/chitosan nanocomposite, GOc: graphene oxide coated chitosan, GO2c: graphene oxide coated 0.2 %wt graphene oxide/chitosan nanocomposite) 50

Figure 3.13 SEM images of HaCaT and L929 cultured on sharkskin mimicked membranes 1 day post culture. Scale bars: 100μm and 10μm. 51

Figure 3.14 SEM images of HaCaT and L929 cultured on sharkskin mimicked membranes 3 days post culture. Scale bars: 100μm and 10μm. 52

Figure 3.15 SEM images of HaCaT and L929 cultured on sharkskin mimicked membranes 5 days post culture. Scale bars: 100μm and 10μm. 53

Figure 4.1 Schematic representation of experimental procedures for SSM CH/Amp/CAPE membrane preparation. **A)** Sharkskin mimicked negative mold preparation, **B)** Amp-CAPE loaded CH membrane fabrication, **C)** Bacterial biofilm growth test, and **D)** HaCaT and HDFa cell culture experiments. 61

Figure 4.2 Swelling ratio results (SSM: sharkskin mimicked, CH: chitosan, Amp: Ampicillin sodium salt, CAPE: Caffeic acid phenethyl ester, A1: 1 mg/mL Amp, A2.5: 2.5 mg/mL Amp, C200: 200 μM CAPE, C500: 500 μM CAPE, C1000: 1000 μM CAPE, A1-C200: 1 mg/mL Amp + 200 μM CAPE, A1-C500: 1 mg/mL Amp + 500 μM CAPE, A1-C1000: 1 mg/mL Amp + 1000 μM CAPE, A2.5-C200: 2.5 mg/mL Amp + 200 μM CAPE, A2.5-C500: 2.5 mg/mL Amp + 500 μM CAPE, A2.5-C1000: 2.5 mg/mL Amp + 1000 μM CAPE). 68

Figure 4.3 Tensile strength results of plain membranes of all chemical compositions (Mean ± SD, *p < 0.05, CH: chitosan, Amp: Ampicillin sodium salt, CAPE: Caffeic acid phenethyl ester, A1: 1 mg/mL Amp, A2.5: 2.5 mg/mL Amp, C200: 200 μM CAPE, C500: 500 μM CAPE, C1000: 1000 μM CAPE, A1-C200: 1 mg/mL Amp + 200 μM CAPE, A1-C500: 1 mg/mL Amp + 500 μM CAPE, A1-C1000: 1 mg/mL Amp + 1000 μM CAPE, A2.5-C200: 2.5 mg/mL Amp + 200 μM CAPE, A2.5-C500: 2.5 mg/mL Amp + 500 μM CAPE, A2.5-C1000: 2.5 mg/mL Amp + 1000 μM CAPE). 69

Figure 4.4 XPS survey spectra (SSM: sharkskin mimicked, CH: chitosan, Amp: Ampicillin sodium salt, CAPE: Caffeic acid phenethyl ester, A2.5: 2.5 mg/mL Amp, C500: 500 μM CAPE, A2.5-C500: 2.5 mg/mL Amp + 500 μM CAPE). 70

Figure 4.5 FTIR spectra of CH, A 2.5, C500, and A2.5-C500 membranes (CH: chitosan, Amp: Ampicillin sodium salt, CAPE: Caffeic acid phenethyl ester, A2.5: 2.5 mg/mL Amp, C500: 500 μM CAPE, A2.5-C500: 2.5 mg/mL Amp + 500 μM CAPE) 72

Figure 4.6 AFM results (10 μm x 10 μm scan area) of plain membranes (CH: chitosan, Amp: Ampicillin sodium salt, CAPE: Caffeic acid phenethyl ester, A2.5: 2.5 mg/mL Amp, C500: 500 μM CAPE, A2.5-C500: 2.5 mg/mL Amp + 500 μM CAPE). 73

Figure 4.7 Drug release results of Amp (μg Amp per mg sample) after 24 h incubation in dH_2O at 37°C); **A)** Amp-only groups, **B)** A1-CAPE groups, **C)** A2.5-CAPE groups (Mean ± SD, *p< 0.05, **p< 0.001, SSM: sharkskin mimicked, Amp: Ampicillin sodium salt, CAPE: Caffeic acid phenethyl ester, A1: 1 mg/mL Amp, A2.5: 2.5 mg/mL Amp, A1-C200: 1 mg/mL Amp + 200 μM CAPE, A1-C500: 1 mg/mL Amp + 500 μM CAPE, A1-C1000: 1 mg/mL Amp + 1000 μM CAPE, A2.5-C200: 2.5 mg/mL Amp + 200 μM CAPE, A2.5-C500: 2.5 mg/mL Amp + 500 μM CAPE, A2.5-C1000: 2.5 mg/mL Amp + 1000 μM CAPE). 74

Figure 4.8 Drug release of CAPE (μM CAPE per mg sample) after 24 h incubation in dH_2O at 37°C); **A)** CAPE-only groups, **B)** A1-CAPE groups, **C)** A2.5-CAPE groups (Mean ± SD, *p < 0.05, **p < 0.001, SSM: sharkskin mimicked, Amp: Ampicillin sodium salt, CAPE: Caffeic acid phenethyl ester, C200: 200 μM CAPE, C500: 500 μM CAPE, C1000: 1000 μM CAPE, A1-C200: 1 mg/mL Amp + 200 μM CAPE, A1-C500: 1 mg/mL Amp + 500 μM CAPE, A1-C1000: 1 mg/mL Amp + 1000 μM CAPE, A2.5-C200: 2.5 mg/mL Amp + 200 μM CAPE, A2.5-C500: 2.5 mg/mL Amp + 500 μM CAPE, A2.5-C1000: 2.5 mg/mL Amp + 1000 μM CAPE). 76

Figure 4.9 Zone of inhibition of plain and SSM samples against *S. aureus* bacteria on TSA plate after 24 h incubation at 37°C. 77

Figure 4.10 Bacterial biofilm growth of *S. aureus* in TSB over 24 h (MTT assay). **A)**Amp-only SSM and plain membrane, **B)** CAPE-only SSM and plain membrane, **C)** A1-CAPE SSM and plain membrane, **D)** A2.5-CAPE SSM and plain membrane (Mean ± SD, *p < 0.05, **p < 0.001, #p < 0.001 compared to the control group, plain CH, SSM: sharkskin mimicked, Amp: Ampicillin sodium salt, CAPE: Caffeic acid phenethyl ester, CH: chitosan, A1: 1 mg/mL Amp, A2.5: 2.5 mg/mL Amp, C200: 200 μM CAPE, C500: 500 μM CAPE, C1000: 1000 μM CAPE, A1-C200: 1 mg/mL Amp + 200 μM CAPE, A1-C500: 1 mg/mL Amp + 500 μM CAPE, A1-C1000: 1 mg/mL Amp + 1000 μM CAPE, A2.5-C200: 2.5 mg/mL Amp + 200 μM CAPE, A2.5-C500: 2.5 mg/mL Amp + 500 μM CAPE, A2.5-C1000: 2.5 mg/mL Amp + 1000 μM CAPE). 79

Figure 4.11 SEM images of *S. aureus* growth on plain and SSM CH membranes after 24 h incubation at 37°C. Red arrows indicate layers of bacteria on the surface of the membranes. Scale bars: 20 μm, 5 μm, and 2 μm (SSM: sharkskin mimicked, Amp: Ampicillin sodium salt, CAPE: Caffeic acid phenethyl ester, CH: Chitosan, A1: 1 mg/mL Amp, A2.5: 2.5 mg/mL Amp, C200: 200 μM CAPE, C500: 500 μM CAPE, C1000: 1000 μM CAPE). 81

Figure 4.12 SEM images of *S. aureus* growth on plain and SSM CH membranes after 24 h incubation at 37°C. Red arrows indicate layers of bacteria on the surface of the membranes. Scale bars: 20 μm, 5 μm, and 2 μm (SSM: sharkskin mimicked, Amp: Ampicillin sodium salt, CAPE: Caffeic acid phenethyl ester, CH: Chitosan, A1-C200: 1 mg/mL Amp + 200 μM CAPE, A1-C500: 1 mg/mL Amp + 500 μM CAPE, A1-C1000: 1 mg/mL Amp + 1000 μM CAPE, A2.5-C200: 2.5 mg/mL Amp + 200 μM CAPE, A2.5-C500: 2.5 mg/mL Amp + 500 μM CAPE, A2.5-C1000: 2.5 mg/mL Amp + 1000 μM CAPE). 83

Figure 4.13 **A)** HDFa cell viability (MTT assay) results, **B)** HaCaT cell viability (MTT assay) results, **C)** HDFa cell proliferation (AlamarBlue assay) results, **D)** HaCaT cell proliferation (AlamarBlue assay) results (Mean ± SD, *p $<$ 0.05, **p $<$ 0.001, $^{\#}$p $<$ 0.001 compared to the CH control, n=3, Amp: Ampicillin sodium salt, CAPE: Caffeic acid phenethyl ester, CH: Chitosan, A2.5: 2.5 mg/mL Amp, C1000: 1000 μM CAPE, A1-C500: 1 mg/mL Amp + 500 μM CAPE, A1-C1000: 1 mg/mL Amp + 1000 μM CAPE, A2.5-C500: 2.5 mg/mL Amp + 500 μM CAPE, A2.5-C1000: 2.5 mg/mL Amp + 1000 μM CAPE). 86

Figure 4.14 SEM images of HDFa and HaCaT on SSM CH membranes on day 1. Scale bars: 200 μm and 50 μm (CH: Chitosan, A2.5: 2.5 mg/mL Amp, C1000: 1000 μM CAPE, A1-C500: 1 mg/mL Amp + 500 μM CAPE, A1-C1000: 1 mg/mL Amp + 1000 μM CAPE, A2.5-C500: 2.5 mg/mL Amp + 500 μM CAPE, A2.5-C1000: 2.5 mg/mL Amp + 1000 μM CAPE, Control: glass slide). 87

Figure 4.15 SEM images of HDFa and HaCaT on SSM CH membranes on day 3. Scale bars: 200 μm and 50 μm (CH: Chitosan, A2.5: 2.5 mg/mL Amp, C1000: 1000 μM CAPE, A1-C500: 1 mg/mL Amp + 500 μM CAPE, A1-C1000: 1 mg/mL Amp + 1000 μM CAPE, A2.5-C500: 2.5 mg/mL Amp + 500 μM CAPE, A2.5-C1000: 2.5 mg/mL Amp + 1000 μM CAPE, Control: glass slide). 88

Figure 4.16 SEM images of HDFa and HaCaT on SSM CH membranes on day 5. Scale bars: 200 μm and 50 μm (CH: Chitosan, A2.5: 2.5 mg/mL Amp, C1000: 1000 μM CAPE, A1-C500: 1 mg/mL Amp + 500 μM CAPE, A1-C1000: 1 mg/mL Amp + 1000 μM CAPE, A2.5-C500: 2.5 mg/mL Amp + 500 μM CAPE, A2.5-C1000: 2.5 mg/mL Amp + 1000 μM CAPE, Control: glass slide). 89

Figure 4.17 Lysozyme-induced enzymatic degradation (CH: Chitosan, A2.5: 2.5 mg/mL Amp, C1000: 1000 μM CAPE, A1-C500: 1 mg/mL Amp + 500 μM CAPE, A1-C1000: 1 mg/mL Amp + 1000 μM CAPE, A2.5-C500: 2.5 mg/mL Amp + 500 μM CAPE, A2.5-C1000: 2.5 mg/mL Amp + 1000 μM CAPE). 90

LIST OF TABLES

Table 3.1	Experimental groups of CH/GO nanocomposites and their chemical contents.	34
Table 4.1	Chemical compositions of experimental groups.	60
Table 4.2	Atomic ratios of CH, A2.5, C500 and A2.5-C500 membrane obtained from XPS analysis.	71
Table 4.3	Characteristic FTIR peaks and their corresponding wavenumbers (cm^{-1}).	71

LIST OF SYMBOLS

°C	Degree Celsius
μ	micro
C	Carbon
D	Depth
g	gram
H	Hydrogen
H_2O	Dihydrogen monoxide (water)
k	kilo
L	Liter
L	Length
M	Molar
m	milli
N	Nitrogen
Na	Sodium
O	Oxygen
V	Volt
W	Watt
w	weight

LIST OF ABBREVIATIONS

2D	Two Dimensional
3D	Three Dimensional
A. baumannii	*Acinetobacter baumannii*
AFM	Atomic Force Microscopy
Amp/A	Ampicillin Sodium Salt
ANOVA	Analysis of Variance
ATCC	American Type Culture Collection
AU	Artificial Urine
BSA	Bovine serum albumin
CAPE/C	Caffeic Acid Phenethyl Ester
CFU	Colony Forming Units
CH	Chitosan
CO_2	Carbon dioxide
CVC	Central Venous Catheters
DAPI	4', 6-diamidino-2-phenylindole
dH_2O	Distilled water
DMEM	Dulbecco's Modification of Eagle Medium
DMSO	Dimethyl sulfoxide
DRIs	Device-related infections
E. coli	*Escherichia coli*
EPS	Extracellular Polymeric Substance
ETTs	Endotracheal Tube
FBS	Fetal Bovine Serum
FPPS	Flexible Piezoresistive Pulse Sensor
FTIR	Fourier-Transform Infrared Spectroscopy
GO	Graphene Oxide
GOc	Graphene Oxide coated
HaCaT	Human dermal keratinocyte

HAIs	Hospital Acquired Infections
HDFa	Human dermal fibroblast
HMDS	Hexamethyldisilazane
IC50	Half-maximal inhibitory concentration
IF	Immunofluorescence
ISK	Inversed Sharklet
K. pneumonia	*Klebsiella pneumonia*
L929	Mouse fibroblast
LB	Lysogeny broth
MPC	2-methacryloyloxyethyl phosphorylcholine
MRO	multi-antibiotic resistant organism
MRSA	methicillin-resistant *Staphylococcus aureus*
MSSA	methicillin-sensitive *Staphylococcus aureus*
MTT	3-(4,5-dimethylthiazol-2-yl)-2,5-diphenyltetrazolium bromide
NaOH	Sodium hydroxide
OD_{600}	Optical Density at 600nm
P. aeruginosa	*Pseudomonas aeruginosa*
PBS	Phosphate Buffer Saline
PDMS	Polydimethylsiloxane (Sylgard 184)
PDO3	Poly (disperse orange 3)
PET	Poly (ethylene terephthalate)
PMMA	Polymethyl methacrylate
PVA	Polyvinyl alcohol
QS	Quorum Sensing
R.I.	Reflection Index
ROS	Reactive Oxygen Species
RPMI	Roswell Park Memorial Institute Medium
Rq	Surface roughness
RT	Room Temperature
RTV	Room Temperature Vulcanized
S. aureus	*Staphylococcus aureus*

S.I.	Stiffness Index
SD	Standard Deviation
SEM	Scanning Electron Microscopy
SSM	Sharkskin Mimicked
TCP	Tissue Culture Plate
TiO_2	Titanium dioxide
TSA	Tryptic Soy Agar
TSB	Tryptic Soy Broth
UV-VIS	Ultra Violet-Visable
WCA	Water Contact Angle
XPS	X-Ray Photoelectron Spectroscopy

1. INTRODUCTION

Biomaterial associated infections occur when microorganisms (primarily bacteria) adhere to the surface and form a biofilm [1]. The bacterial biofilm layer could result not only in localized infection but also in systemic infection and inflammation [2]. Preventing the formation of bacterial biofilm on implantable biomaterials has been a major challenge in healthcare for years [3],[4]. Common examples of implantable biomaterial associated infection are cardiac assist device infection and pacemaker pocket infection. These type of infections are very difficult to eliminate and, in most cases, result in prolonged hospitalization [1],[3]. Most common approaches to prevent implant-associated infection are the use of antibiotics and antibacterial agents whether released from the implant or administered as a drug which in most cases result in overuse of drug, causing toxicity and inflammation [5]. A combination of these two approaches is also a widely utilized treatment [6].

Over the past decades there has been many studies aiming at the development of antibacterial materials that promote cell growth as well. Unfortunately, in spite of all these efforts biomaterial-associated infection and inflammation still inflicts serious discomfort to the patient's quality of life, not to mention its high financial burden both for the patient and the healthcare system [4],[7]. Moreover, the prolonged use of antibiotics presents the risk of development of resistance by bacteria such as evident in Methicillin-resistant *Staphylococcus aureus* (MRSA) [8]. Increasing the dose of antibiotics in turn can cause serious adverse effects for patients, leading to more harm which outweighs the benefits of using the drug in the first place [9],[10]. Thus, it is of paramount importance to minimize the use of antibiotics in implantable biomaterials while maintaining the antibacterial, anti-inflammatory, and bio/cytocompatibility properties of said materials for healthcare applications [1],[11].

In this regard, utilizing unique surface topographies has become widely explored during the past two decades as a novel alternative [12–14] Biomimicked nano- and

micropatterned surfaces such as sharkskin, dragonfly wing [15], and gecko skin which have shown remarkable potential in reducing bacterial adhesion [16],[17] are the front-runners of this race [18]. Moreover, recent studies have shown that these surface topographies can influence bacterial adhesion and biofilm formation via either reduction or inhibition of bacterial settlement [19],[20]. Hence, taking advantage from natural phenomena in order to design and fabricate biomaterials with enhanced antibacterial and cytocompatibility is worthy endeavor.

1.1 Motivation

Sharks have attracted the attention of many researchers for the past few decades due to two main characteristic features of their skin: drag-reduction and antifouling properties [21–23]. Sharkskin microtopography has been investigated in the two forms of biomimicked and bioinspired [19] for its biological properties [17] as well as hydrodynamic characteristics [24],[25]. The procedure of biomimicking sharkskin only replicates the epidermis (the outermost layer) of the skin which is in contact with water and it does not include replicating the dermis [26],[27]. Studies on sharkskin mimicked surfaces have proven that the unique microstructures on the sharkskin surface known as "denticle" decreases the friction forces at the interface of water and skin leading to reduced drag force and increased swimming speed of the shark [17],[28]. Consequently, it is hypothesized that the antibacterial effect of sharkskin topography occurs via prevention of adhesion of microorganisms to the surface of the shark's skin as a result of increased flow rate at the interface [29],[27].

Numerous studies have used sharkskin mimicked or bioinspired structures for fabrication of antibacterial surfaces using Polydimethylsiloxane (PDMS) and other non-biodegradable hydrophobic materials as the substrate. Nevertheless, the true mechanism of antibacterial activity of sharkskin is yet unknown despite the reported high anti-biofouling results in the literature [27],[30],[31]. So far, antibacterial properties of sharkskin mimicked substrates made of natural and hydrophilic polymers, such as Chitosan (CH), have not been studied. Moreover, there is not sufficient information

in the literature regarding the effects of sharkskin mimicked or bioinspired topography on cell adhesion and proliferation. Furthermore, despite extensive knowledge available regarding the use of CH constructs for delivery of a wide range of antibacterial agents, the effect of surface topography on the release rate of drugs is still unknown.

While focusing on achieving antibacterial characteristics in an implantable biomaterial, it is of utmost importance to not only prevent cytotoxicity but also to enhance the adhesion and growth of mammalian cells as much as possible. Achieving such a duo in a cost-effective and straight-forward manner would have tremendous biomedical applications [15].

To this end, inspired from nature, design and fabrication of sharkskin mimicked polymeric hydrogel membranes using CH is studied in terms of reducing bacterial adhesion and biofilm formation as well as promoting cellular viability and proliferation [31],[32].

CH is a biodegradable natural polymer which has antibacterial properties rising from its chemical structure [33]. It is well-known that CH owes its antibacterial activity against a wide range of microorganisms to the presence of its cationic groups. The ionic interactions of these charged groups with bacteria cell wall constituents damages the bacteria leading to its death. Thus, the highest antibacterial activity of chitosan is reported in its solution or gel form rather that solid film form [34],[35]. Due to the presence of numerous functional groups within CH structure [36],[37], many studies have been conducted on crosslinking it with antibacterial agents such as Graphene Oxide (GO). Conjugation of CH and GO in form of nanocomposites has been studied by many with the aim of enhancing CH membranes'physicochemical and antibacterial properties [38],[39]. Based on previous reports, conjugation of GO into CH polymeric membranes does indeed enhance its mechanical and chemical properties, but the amount of GO required to induce such changes is rather high [40] and might cause cytotoxicity and tissue damage in case of degradation after implantation. Also, most of the techniques for the fabrication of these composites utilize various cross-linkers [41] which are cytotoxic and most probably unnecessary. Furthermore, there is very little

information regarding the antibacterial and chemical characteristics of GO coated onto CH membrane and its advantages and disadvantages compared to GO/CH nanocomposite. Therefore, antibacterial and cytotoxicity properties of GO/CH composites with low GO concentrations without the use of cross-linkers are needed to be investigated in two distinct forms: nanocomposite and surface coating. In addition to chemical modifications, the antibacterial potentials of CH membrane can be enhanced via utilizing biomimetic techniques and shaping it into a surface with the unique surface topography of sharkskin. In order to fill in all the aforementioned gaps, a part of the presented thesis was designed to investigate not only the individual effect of GO and sharkskin topography on antibacterial and biocompatibility characteristics of CH membranes but also evaluate the dual effect of chemical and topographical cues on these properties.

As mentioned before, due to the presence of numerous oxygen-containing functional groups within its chemical structure [42], CH can interact with a wide variety of chemicals and has a high capacity for modifications [43], thus providing a vast range of applications as a compatible biomaterial for healthcare applications namely drug carrier, wound patch, etc. [44],[45]. Ease of conjugation of CH with Ampicillin sodium salt (Amp), a water-soluble drug [46],[47], along with Caffeic Acid Phenethyl Ester (CAPE), the active component of propolis [48], gives rise to countless designs for drug-loaded polymeric substrates [42],[45].

Amp, which is a well-known broad-spectrum and potent antibiotic, has been used to treat bacterial infections for many years [49]. Amp-loaded polymeric microgranules and fibers, for instance, have been used as local delivery for treatments of infection in many cases such as wound healing [50],[51]. In this regard, it has been reported that polymers like CH provide a matrix for the controlled release of Amp which is a crucial property for implantable biomaterials [52]. Aside from Amp, CAPE which is the extract of honey bee propolis has been known to act as an antioxidant, antibacterial, anti-inflammatory, and cytotoxic compound against mammalian and bacterial cells [53–55]. The necessity of CAPE extraction arose from some standardization complications of using propolis due to the differences in its chemical composition based on the origin [56],[57]. The extent of CAPE's effect is highly dependent on the dose at

which it is administered as well as the means of delivery [56],[58]. Since CAPE is not a water-soluble compound, it extremely difficult for IV administration at high doses, hence it requires a vehicle to carry it and release it in a timely manner at the target location [56],[59]. Such a problem can be resolved by loading a polymer-based carrier with high doses of CAPE that would allow for its local delivery at controlled rates [60]. Therefore, loading CAPE into the CH network and fabricating membranes from this mixture is a potential approach for the delivery of the otherwise undeliverable high doses of CAPE [20].

Overall, the goal of this thesis was to fabricate an implantable and biodegradable biomaterial via utilizing sharkskin surface micropattern along with bactericidal agents, which possesses enhanced antibacterial characteristics as well as investigating the effect of sharkskin topography on drug release and antibacterial activity and cytocompatibility of the membranes.

1.2 Objectives and Outline

The objective of this thesis was to obtain polymeric membranes with enhanced antibacterial and cytocompatible properties. Properties which will make these membranes potential candidates for fabrication of other polymeric structure having enhanced antibacterial properties and *in vivo* application (implantation). This will be achieved by using and combining CH as the biodegradable component of the hydrogel membrane, and GO, Amp, and CAPE as chemical antibacterial agents, along with the presence of the unique surface micropattern of shark skin as the morphological aspect of the thesis.

The outline of this thesis is as following:

- Chapter 2: Delivering a comprehensive and thorough summary of the literature on sharkskin biomimicked and bioinspired surfaces and their applications in in-

dustry so far to demonstrate their potentials along with brief introduction of the used materials and their properties.

- Chapter 3: Presenting the data obtained for antibacterial and cytocompatibility study of sharkskin mimicked CH/GO membranes.
- Chapter 4: Presenting the data obtained for antibacterial and cytotoxicity study of sharkskin mimicked CH/Amp, CH/CAPE, and CH/Amp/CAPE membranes.

2. BACKGROUND

2.1 Sharkskin: Anatomy and Characteristics

In most animals, the skin is known to play the roles of both a sensory mechanism for detecting changes in the environmental factors, like humidity, temperature fluctuations, and pressure changes, and as a shield against harmful stimlui [61]. This means that the skin is not directly involved in locomotion. However, in most fish, the skin has an active role in regulating motion in addition to sensing and protecting. This happens via the muscles which are attached to the skeletal structure on the inner side and to the skin on the outer side through collagenous myosepta [62]. This implies that the muscle contractions which initiate the motion directly affect the skin. The skin of fish is basically a matrix of reinforced collagen fibers and the composition of the collagen within this fibrous structure greatly depends on the structure of the muscles attached to it [62],[63]. Particularly, in sharks, the entire skin acts as a wide exotendon, with collagen type I [64] as the main component, that regulates the motion forces generated by muscle contractions during swimming. This coordination at different speeds occurs via the shortening and lengthening of muscle fibers which passes along to the tail [65],[66].

Similar to any other marine vertebrates, the skin of sharks is composed of three layers, epidermis (outermost layer), dermis (middle layer) which includes *Stratum laxum* and *Stratum Compactum*, and flesh [67]. The *Stratum Compactum*, which is the bottom layer of the dermis, consists of layers upon layers of collagen fibers in helical formation as if it is an external skeleton all over the shark's body [26] (Figure 2.1A).

Like most fish, the shark skin surface is not smooth. In fact, micro-scale placoids called “dermal denticles” cover the entire exterior surface of all sharks regardless of species [68] (Figure 2.1B). Each of these small denticles consists of a dentine vascular core, which is made of apatite, and an outer layer made of enamel, resembling the

human tooth, hence the name [66],[69]. Since apatite core is housed within a collagen shell in the denticle, each individual denticle is significantly hard yet not brittle [70]. The arrangement of these denticles is rather heterogeneous and occasionally there are gaps. Also, the appearance of these placoids vary in dimensions (depth and height of grooves), size, and shape from one part of the shark to another, in addition to the morphological differences between different species [71],[72] (Figure 2.1C).

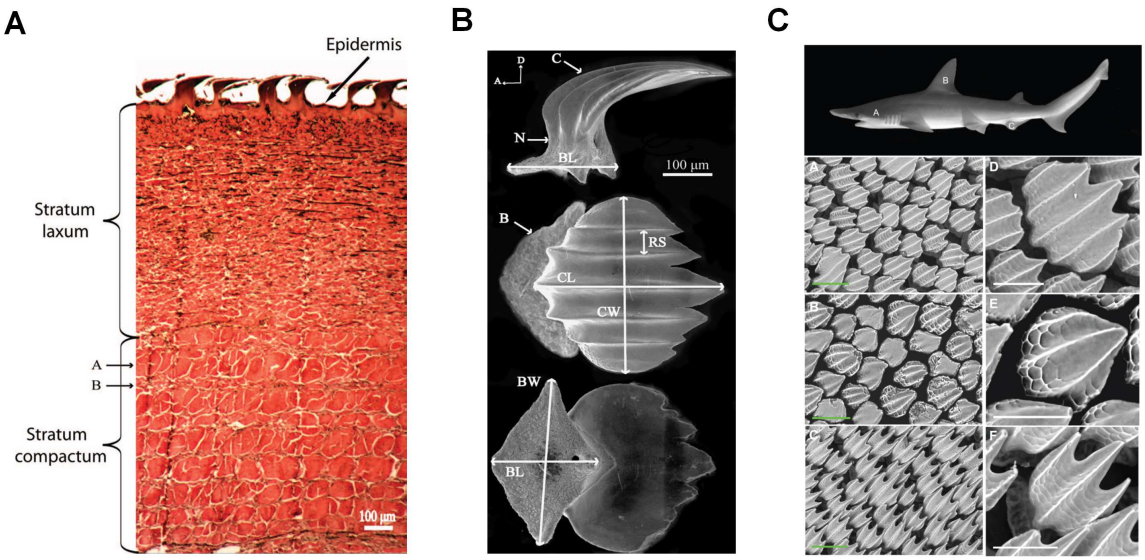


Figure 2.1 **A)** Layers of sharkskin [73]; **B)** Shape and dimensions of the a single blacktip *Carcharhinus limbatus* shark's skin denticle (B, base; BL, base length; BW, base width; C, crown; CL, crown length; CW, crown width; N, neck; RS, riblet spacing) [73]; **C)** Sharkskin morphology at different regions on shark's body [74].

As seen in Figure 2.1A, the root of every denticle is deep-seated within the *Stratum Compactum*, whereas the tip, which is also known as the crown, is in direct contact with water relatively parallel to the direction of water flow pointing to the opposite direction of the swimming [73]. The surface of each crown has a few riblets which create grooves and hills. Due to these tiny dermal placoids, the highly active skin of sharks has two very important functions which are drag reduction [74],[75] and anti-biofouling [17],[66].

The speed of swimming of sharks was the first attribute that was noticed and extensively studied by scientists. These studies led to the discovery of the drag force

reduction property of the shark's skin [24]. Researchers found that the dermal denticles covering the surface of sharkskin regulate the flow of water while the shark is swimming so that the drag forces at the interface reduce significantly, consequently making sharks one of the fastest swimmers among the marine animals [76]. For instance, the shortfin mako shark (*Isurus oxyrinchus*), which is the fastest among all sharks, is reported to have reached the speed of approximately 50 km/hour (31 miles/hour) [77].

Following drag reduction findings, scientists realized that the skin of sharks remains free of microorganism attachment and biofouling which was a rare phenomenon among large marine animals [78]. The anti-biofouling attribute of sharkskin has been recognized rather recently and is still being studied [79],[80]. During the past two decades, studies have been conducted on understanding the extent and the mechanism of the anti-biofouling effect of sharkskin micropatterns and whether they can be translated into healthcare applications namely wound healing patches [81], antibacterial plastic medical equipment such as cathaters [82], biodegradable implantable antibacterial materials [17], and covering sheets for the prevention of surface contamination in healthcare centers [83].

Contrary to the reduced drag force property where a great number of articles have been published over the years [69],[76],[84–86], there is not a comprehensive study on the antibacterial and anti-biofouling effects of sharkskin, even though numerous studies have been conducted on designing sharkskin bioinspired and biomimicked structures for several medical applications [87].

2.2 Bacterial Colonization and Biofilm Formation on Surfaces: A Short Summary of Mechanisms and Impacts

Microorganisms are found everywhere in our surroundings, on all kinds of surfaces, and even on our skin [88]. Biofouling, which refers to the "*undesirable accumulation of biotic deposit on a surface*", is a common phenomenon in healthcare. Biofouling

of bacteria on any type of surface results in the formation of fullthickness bacterial biofilms on the surface, causing serious problems [89] (Figure 2.2A).

2.2.1 Bacterial Biofilm: Structure and Properties

Bacterial biofilm formation requires the initial settlement of planktonic bacteria on the surface on a surface, either biotic or abiotic [90], that is in contact with aqueous medium [91]. This transition from floating or planktonic stage to sessile or immobile stage is the first step towards bacterial biofilm formation. Following the initial adhesion, the bacterium starts to divide and within a few hours, the surface is nearly fully covered with a layer of bacteria. As time passes, the Extracellular Polymeric Substance (EPS) is produced by the bacteria, which acts as an impenetrable protective layer for all bacteria ensuring its prolonged viability especially in hostile environments [92],[93]. Individual bacterium within the EPS can communicate with each other through biochemical signals [94]. This internal signaling network within the EPS is known as Quorum Sensing (QS) [95]. Additionally, the components of the EPS regulate the metabolic activities of the enclosed bacteria. Growth and maturation of the biofilm depends on several factors namely medium pH level, nutrients, temperature, surface roughness, surface wettability, and surface chemistry [93]. It has been hypothesized that changes in environmental factors induces stress upon the bacteria encased inside the EPS and as a result of QS, the bacteria activate stress response genes to protect themselves [96]. These environmental factors and the resulting changes within the EPS-enclosed bacteria regulates the shape and morphology of the biofilm [97].

The EPS, which is self-produces and slimy in nature, is comprised of many types of macromolecules such as nucleic acids, polysaccharides, proteins, enzymes, lipids, along with ions [90]. Forces like electrostatic force and hydrogen bonds keep the internal structure of the EPS together and provide its integrity. Moreover, the water content of the EPS and its interstitial voids play a vital role in providing a constant and effective nutrient circulation along the biofilm [98]. The amount of EPS increases as the biofilm ages [99]. The composition of EPS differs from one strain of bacteria to

the another, however, the main component is polysaccharide. For instance, the biofilm in Gram negative strains is either neutral or polyanionic [100]. On the other hand, Gram positive bacteria have cationic chemistry [101]. Additionally, it is the structure and composition of these polysaccharides that dictate the primary configuration of the biofilm layer. The backbone of the majority of biofilm types consist hexose residues. These residues give rigidity to the biofilm resulting in its low solubility in water [102].

Although the morphology and number of layer of bacteria within the EPS varies from one strain to another, biofilms are usually heterogeneous and sophisticated. A biofilm normally is comprised of layer upon layers of bacterial cells with interconnected water channels [90]. The biofilm thickness as well as its shape is highly dependent on the strain type. A biofilm layer may house more than one type of bacteria. In case of mixed culture biofilms, it has been reported that neither one enhances the stability of the other species [103].

There have been several studies on the mechanisms by which biofilm resists the antibacterial agents and antibiotics [104–106]. Some of these findings are as follows: i. EPS prevents and/or delays the penetration of antibiotics [106], ii. In case of sensing the presence of antibiotics, bacterial cells activate multidrug efflux pump to pump out the antibacterial chemicals that has penetrated the biofilm in order to save the biofilm [105], and iii. Activation of horizontal gene transfer by the bacteria leading to development of resistance [104].

2.2.2 Implant Associated Bacterial Infection

A medical device is "*an instrument, apparatus, appliance, tool or equipment used in the prevention, diagnosis, treatment, mitigation, rehabilitation and/or generation of information of a disease or medical condition*" [107]. Any of these devised that can be implanted within the human body is referred to as "implantable medical device". Most notable of these devices are cardiac assist devises, various catheters, bone and hip implants, and intrauterine devices. Adhesion and colonization of any kind of bacteria on

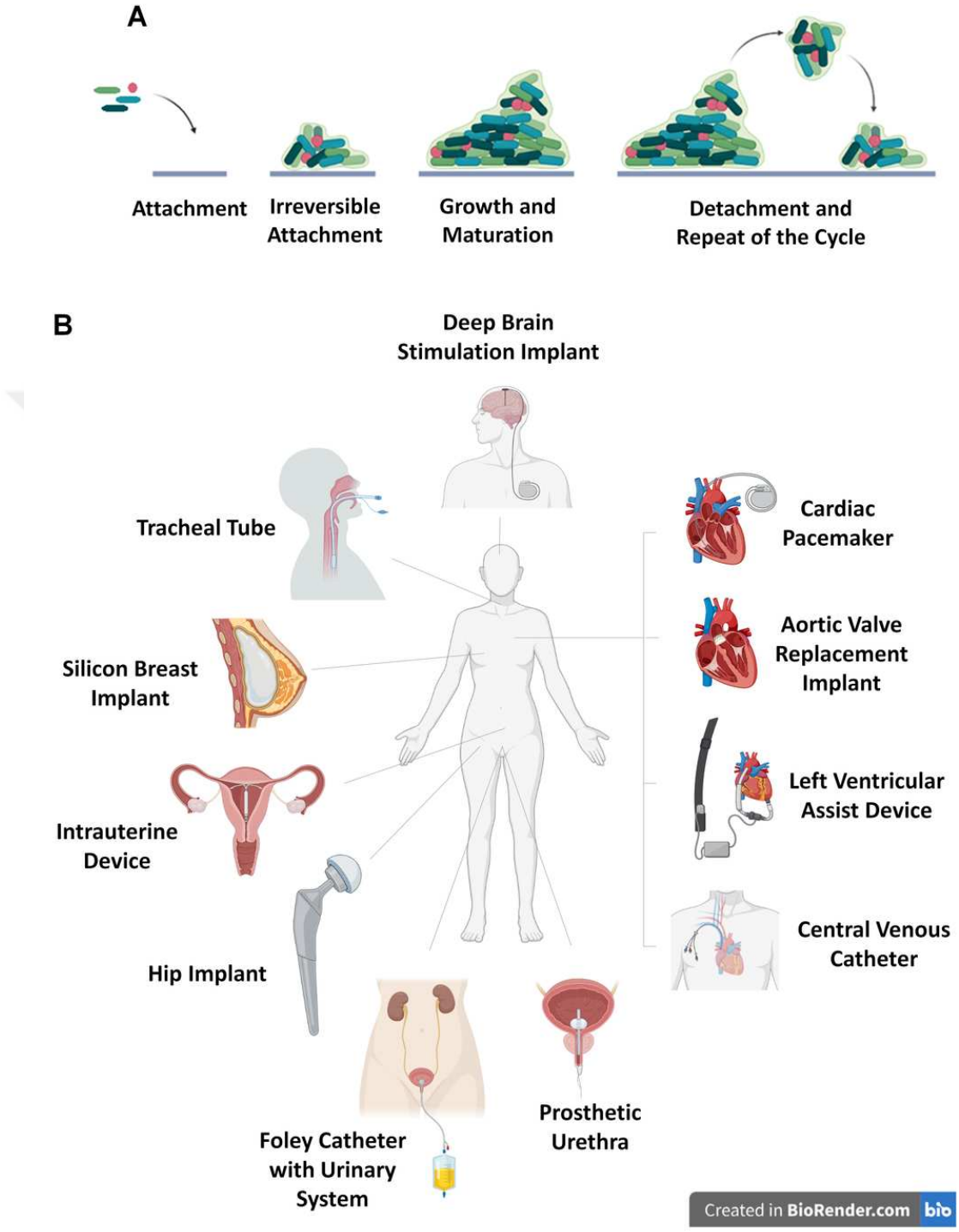


Figure 2.2 **A)** Illustration of stages of full thickness bacterial biofilm formation (Created in Biorender.com); **B)** Various surfaces of implantable medical devices prone to bacterial biofilm formation (Created in Biorender.com).

these devices poses the great risk of formation of biofilm on them which in severe cases leads to systemic infection. Examples of most common surface-associated bacterial infection of implants are infected pacemakers, single-use plastic products like urinary catheters, and silicon breast implants [108] (Figure 2.2B). This type of infections lead to prolonged hospitalization and in severe cases even the death of the patient [109]. Moreover, the cost of hospitalization for treating implant related systemic infection is very high [110]. Antibiotics and antibacterial agents have been sought as the solution for this issue for many decades, which unfortunately gave rise to the development of resistance in some of the most dangerous and pathogenic strains of bacteria such as methicillin-resistant *Staphylococcus aureus* (MRSA) [111],[112]. Hence, defeating these types of infections without overuse of antibiotics is of utmost importance and urgency.

Apart from these types of infections, Hospital Acquired Infections (HAIs) are other issues with formation of bacterial biofilms on medical devices and hospital surfaces [113]. Examples of these surfaces are hygiene sink drain and inanimate environment around patients [114],[115]. According to a report by Carling *et al.* there is an approximate 74% chance of transfer of infection from one infected patient with multi-antibiotic resistant organism (MRO) to a healthy patient due to HAIs [116].

All these infections start with the adhesion of bacteria to the surface. Thus, preventing the adhesion of planktonic bacteria in the first place would hinder the formation of the biofilm altogether. To do so, making use of unique natural or engineered surface micro and nano-topographies such as sharkskin pattern could be very helpful.

2.3 Sharkskin Patterned Surfaces: Methods of Fabrication and Their Antibacterial, Anti-Biofouling and Other Biological Properties

Bionic is a term that describes any engineered design that is either mimicked, inspired or guided by nature [117],[118]. As the need for anti-biofouling, antiviral and

antibacterial surfaces increased, scientific inquiries were made into how animals and plants deal with the issue of microorganism adhesion and infection [119]. Sharks have been at the epicenter of this quest for some years now and many have tried fabricating surfaces that mimic the exact surface topography of sharkskin or create structures that resemble the shape of sharkskin microstructure at various scales and dimensions [86].

One of the first studies on the anti-biofouling properties of sharkskin itself was conducted by Peng *et al.* [23]. The authors conducted a study on the attachment of *Mytilus edulis* byssus along with the adhesion of diatoms on the sharkskin via optical and SEM image acquisition. The authors'reported results revealed an obvious reduction of diatom adhesion on the skin of a live shark compared to a dead one. Authors hypothesized that the high speed of the shark while swimming which is a direct result of water flow on the placoid microstructures, also known as dermal denticles, result in a very strong momentum exchange at the surface of the skin resulting in decreased chances of diatom attaching to the surface in addition to ease of detachment of those already settled on the skin [23].

2.4 Sharkskin Bioinspired Surfaces: Fabrication and Bio-fouling Properties

2.4.1 Marine Biofouling on Sharkskin Bioinspired Surfaces

To the best of our knowledge, Š . Petronis *et al.* [120] conducted the first study on naturally occurring topographical features inspired by sharkskin and its bioadhesive characteristics. They created pyramids and riblets structures separately at various dimensions using room temperature vulcanized (RTV) silicone surfaces along with Polydimethylsiloxane (PDMS) was used as the material to prepare these surfaces via solution casting (molding) technique. The height of both shapes was in the range of 23 - 69 μm and the width was between 33 - 97 μm. The authors measured the macrofouling of barnacles *Balanus improvises* in a field study at the west coast of

Sweden. The objective was to optimize the surface feature dimensions for minimum adhesion. Electron spectroscopy, dynamic contact angle, and time-of-flight secondary ion mass spectroscopy measurements were taken. It is reported that the 69 μm-high riblet features reduced the larvae settling by nearly 67%. It was concluded that the feature dimension plays a vital role in controlling and inhibiting larvae settlement [120].

2.4.2 Bacterial Adhesion on Sharkskin Bioinspired Surfaces: Mere Effect of Topography

Following the initial findings on the anti-bioadhesive properties of Sharklet AF^{TM} design against *Ulva linza* zoospores and its superiority among other engineered surface topographies, Chung *et al.* [32] reported that the sharkskin pattern inspired surface topography, Sharklet AF^{TM}, successfully reduces the rate of biofilm formation of *Staphylococcus aureus* (*S. aureus*) over the course of 21 days of incubation in stationary conditions. Sharklet micropatterned PDMS substrate was tested for bacterial coverage over a prolonged culture period of 21 days against a smooth PDMS surface as a control. The authors'aim was to understand the effectiveness of surface topography on the inhibition of bacterial adhesion to the surface. Based on their reported results, bacteria covered nearly 54% of the smooth surface after 14 days of culture while the coverage on the Sharklet patterned surface was only 7%. The remarkable decrease in the bacterial growth on the surface indicated the positive impact of the Sharklet micropattern in disrupting bacterial biofilm formation of *S. aureus* [32].

One of the most susceptible locations for bacterial colonization and biofilm formation is the inside of catheters. In urinary catheters, for instance, bacterial adhesion moslty leads to urinary tract infection which imposes serious risks and complications for patients. In this regard, Reddy *et al.* [82] investigated the potentials of Sharklet AF^{TM} design in preventing catheter-associated urinary tract infection by inhibiting bacterial colonization and biofilm formation. To do so, 3 versions of Sharklet pattern varying in pillar width and protrusion were used along with the smooth surface. All of them were made of silicone and uropathogenic *Escherichia coli* (*E. coli*) strain was

used. The colony size, number of bacteria, and area coverage of bacteria were measured to evaluate the colonization along with its migration on the prepared surfaces. Incubation of *E. coli* took place in two mediums: Tryptic Soy Broth (TSB) and artificial urine (AU). According to the reported data, bacterial colonization was reduced on all three patterns compared to the smooth surface with protruded Sharklet having the highest reduction rate. However, for migration assay, Inversed Sharklet pattern (ISK) and enlarged pillars (SK10x2) resulted in a higher decrease in migration rate in AU in comparison to Sharklet AF^{TM}. Another interesting reported finding was the difference between bacterial migration through the Sharklet pattern when patterns were parallel to the direction of migration vs. transversed condition which resulted in a more than 80% reduction in migration rate for the transversed positioning. The importance of inhibiting bacterial colonization in the prevention of catheter-associated infections is of utmost importance hence, the proposed surface pattern has great potentials for this application since it requires to merely pattern the surface without the need for any antibacterial agent [82].

Sakamoto *et al.* [121] investigated the antibacterial effects of sharkskin bioinspired polyacrylate surfaces that were either protruding or recessed. Two types of topographies were designed: one was aligned protruded or recessed lines with equal length, and the other one was sharkskin micropatterned either recessed or protruded. Dimensions of the sharkskin inspired pattern were 0.4 μm in height, and 2 μm in width with 2 μm spacings which was the same as Sharklet AF^{TM} from Chung *et al.*'s work [32] on silicon elastomer Sharklet AF^{TM} (3 μm) surfaces. Linear ridged patterns with dimensions of 2 μm wide, 16 μm long, and 0.4 μm high with 2 μm spacing were used as an alternative pattern. The smooth surface was used as the control group. The authors studied biofilm formation using *Pseudomonas aeruginosa* (*P. aeruginosa*) and *S. aureus* bacteria strains along with a swarming motility test. Their results indicates that despite the shallowness of the patterns in sharkskin patterned surface compared to Sharklet AF^{TM}, the surface exhibited significant inhibitory effects on reducing bacterial biofilm formation for both Gram-negative and Gram-positive strains in comparison to ridged pattern and smooth surfaces. No statistical significance has been reported between biofilm formation on protruding sharkskin pattern and recessed one. The au-

thors concluded that the shape and arrangement of the pattern plays a more important role in reducing bacterial biofilm formation and their motility than their height [121].

2.4.3 Bacterial Adhesion on Sharkskin Bioinspired Surfaces: Dual Effect of Topography and Chemistry

Although sharkskin bioinspired surfaces considerably reduce bacterial adhesion and biofilm formation, they fail to prevent bacterial settlement all together. Thus, combination of chemical cues and sharkskin bioinspired topography needed to be studied. In this regard, Arisoy *et al.* [19] enhanced antibacterial properties of Sharklet patterned surfaces by adding titanium dioxide (TiO_2) nanoparticles. This approach decreased bacterial settlement while eliminating already attached bacteria. To this end, poly (ethylene terephthalate) (PET) composite substrates containing 0, 10, or 50 wt % TiO_2 nanoparticles with sharkskin inspired patterns (Sharklet AF) were fabricated. Furthermore, the surface of these substrates was coated with 90 wt % TiO_2 nanoparticles and 10 wt % tetraethyl orthosilicate. The authors reported that the presence of TiO_2 at only 10wt % concentration was significantly effective in the inactivation of *E. coli* and *S. aureus* up to 95% and 80%, respectively. This technique allows for the mass fabrication of high-performance antibacterial surfaces on large scales [19].

Inspired by sharkskin denticle microtopography, Miyazaki *et al.* [79] designed and fabricated riblet-patterned surfaces that could reduce bacterial colonization on the surface. Samples were produced via a nanoimprinting technique using cycloolefin polymer. To test the antibacterial properties of the fabricated surfaces, *S. aureus* bacteria strain was used and the ratio at which the bacteria cover the surface was measured over a 5-day incubation period under dynamic culture conditions. The result of crystal violet staining of formed biofilms indicated a reduction in the area of the surface covered with bacteria on patterned surfaces as opposed to smooth control groups. This reduction varied as a function of the nonuniformity of the riblets and grooves, which was measured by feature height ratios. It was concluded that a longitudinal vortex is created on the sharkskin-inspired surfaces as a result of liquid flow on the surface,

causing the adhered bacteria to detach, thus suppressing the formation of a bacterial biofilm layer [79].

2.4.4 Sharkskin Bioinspired Surfaces: Potentials of Usage in Medical Instruments

So far, the production of sharkskin patterned polymeric surface (Sharklet) was proven to be rather a straightforward and low-cost procedure. Hence, May *et al.* [31] tested the effect of Sharklet pattern in a more practical setting, the interior of the endotracheal tube (ETTs). The authors aimed to study the reduction in bacterial colonization on said tubes in order to reduce Ventilator-Associated Pneumonia, which is mostly caused due to biofilm formation and infection within the ETT. Several bacterial species are involved in ETT infections among which Gram-negative *E.coli*, *Klebsiella pneumonia* (*K. pneumonia*), *P. aeruginosa*, *Acinetobacter baumannii* (*A. baumannii*), and MRSA are on top of the list. May *et al.* investigated the antibacterial activity of Sharklet microtopography toward all of these bacteria via studying bacterial colonization. Bacterial experiment owed a reduction in colonization percentages of 99.2% for MRSA, 97.2%, 95.6%, and 99.4% for three types of *P. aeruginosa*, 99.5% for *E. coli*, 99.9% for *K. pneumonia*, and 98.6% for *A. baumannii*. The biofilm formation tests also showed a significant reduction in bacterial biofilm on Sharklet micropatterned surfaces with values of 67% and 52% for MRSA and *P. aeruginosa* strains, respectively compared to unpatterned control [31].

In a follow-up study May *et al.* [87] studied the potentials of sharkskin micropattern in reducing colonization of bacteria as well as platelet adhesion on central venous catheters. In an attempt to resolve issues of biofilm formation inside the central venous catheters (CVC), thermoplastic polyurethane Sharklet substrates were fabricated and used for platelet adhesion, bacterial colonization, and fibrin formation tested for two model skin flora bacteria strains, *S. aureus* (ATCC 6538) and *Staphylococcus epidermidis* (*S. epidermidis*) (ATCC 35984). Reported results showed an approximately 70% reduction in bacterial colonization after 18 h incubation for both strains. Fur-

thermore, 86% and 80% reduction of platelet adhesion and fibril sheet formation was observed for *S. aureus* and *S. epidermidis*, respectively. May *et al.* concluded that sharkskin patterned catheters may prevent catheter-related thrombosis and catheter-related bloodstream infections, which are the two main problems of CVC by inhibiting the initial bacterial and platelet adhesion [87].

For evaluating the effectiveness of surface topography in preventing or controlling infection on medical devices, Xu *et al.* [122] developed flat and cylindrical Sharklet micropatterned surfaces and conducted several *in vitro* and *in vivo* experiments to characterize them with respect to the smooth surface as the control. For the *in vitro* bacterial tests, Gram-negative *P. aeruginosa* and Gram-positive *S. aureus* strains were used and colonization assay along with transference assay tests were done. The authors reported a 92.3% and 90.5% reduction in *S. aureus* colonization on a patterned flat surface and patterned cylindrical surface, respectively. As for the transference assay, transference of *S. aureus* was reduced by 95.1%. Approximately 99.9% and 95.5% reductions were reported for colonization of *P. aeruginosa* on the patterned flat surface and patterned cylindrical surface, respectively whereas the transference reduction was found at 94.9%. As for the *in vivo* tests, a percutaneous rat model including healthy or immunocompromised rats was used. Patterned silicone rods were inserted percutaneously into the healthy rats, then the skin of their back was inoculated with *S. aureus*. Examination of spleen and tissue in contact with the rods revealed 88% less *S. aureus* in the spleen and 91% less *S. aureus* in the subcutaneous tissue compared to the smooth surfaces which was a remarkable decrease in infection. The same test was done on immunocompromised rats, which resulted in a 99.5% reduction in bacterial presence on the external segments of the micropatterned implant and 99.9 % fewer bacteria on the internal sections. The quantitative values of bacterial presence detected in the spleen and subcutaneous tissue of immunocompromised rats were 90.7% and 97.8%, respectively [122].

Following the conclusive studies into the effectiveness of sharkskin micropattern in reducing bacterial colonization, Magin *et al.* [81] designed and fabricated a unique gelatin-based hydrogel dressing with Sharklet micropattern to heal full-thickness

wounds. The authors designed Sharklet patterned surfaces with dimensions different than standard Sharklet AF^{TM}. The two pattern types were designated as +1SK10x5, with features measurements of 1 μm in height, 10 μm in width, 5 μm in spacing, and 0.1 aspect ratio, and +10SK50x50 which had 10 μm in feature height, 50 μm in width, 5 μm in spacing, and 0.2 aspect ratio. The designed wound dressing was intended to guide the re-epithelialization and revascularization phases, which are two vital steps in wound healing. *In vitro* cell migration assay experiments were conducted along with a bipedicle ischemic rat wound model for the *in vivo* tests. Approximately 64% increase in wound coverage for Sharklet patterned wound dressing was reported. Additionally, larger features seemed to allow for better migration and surface coverage for the human keratinocyte cells. Moreover, results of rat wound closing and tissue histology revealed that the bilayered Sharklet patterned dressing improved the overall healing of the wound in comparison to untreated control which suggested the high potentials of this micropatterned scaffold for healthcare uses [81].

2.4.5 Sharkskin Bioinspired Surfaces: Adhesion of Viruses and Mammalian Cells

Since the transfer of pathogens is a key effector in the spread of infection, utilizing surface topographies that prevent such transmission is necessary. Liu *et al.* [123] investigated the potential of Sharklet patterned surfaces in the transference of influenza B virus and human coronavirus as well as *S. aureus*, *Bacteriophage T4* microorganisms. To do so, the bead transfer method was used to evaluate pathogen transference on Sharklet patterned surfaces from polypropylene and silicone. Surfaces made from polypropylene, designated as "Sharklet Shield polypropylene", reduced the transfer of influenza B virus and human coronavirus by 82.8% and 85.1% respectively as shown in Figure 2.3. As for *S. aureus* and *Bacteriophage T4*, 97.8% and 93.0% were the values obtained for reduction of transfer rate on silicon surfaces. Results signify the importance of surface topography in micron-scale on the transfer of pathogens and spread of infection [123] (Figure 2.3).

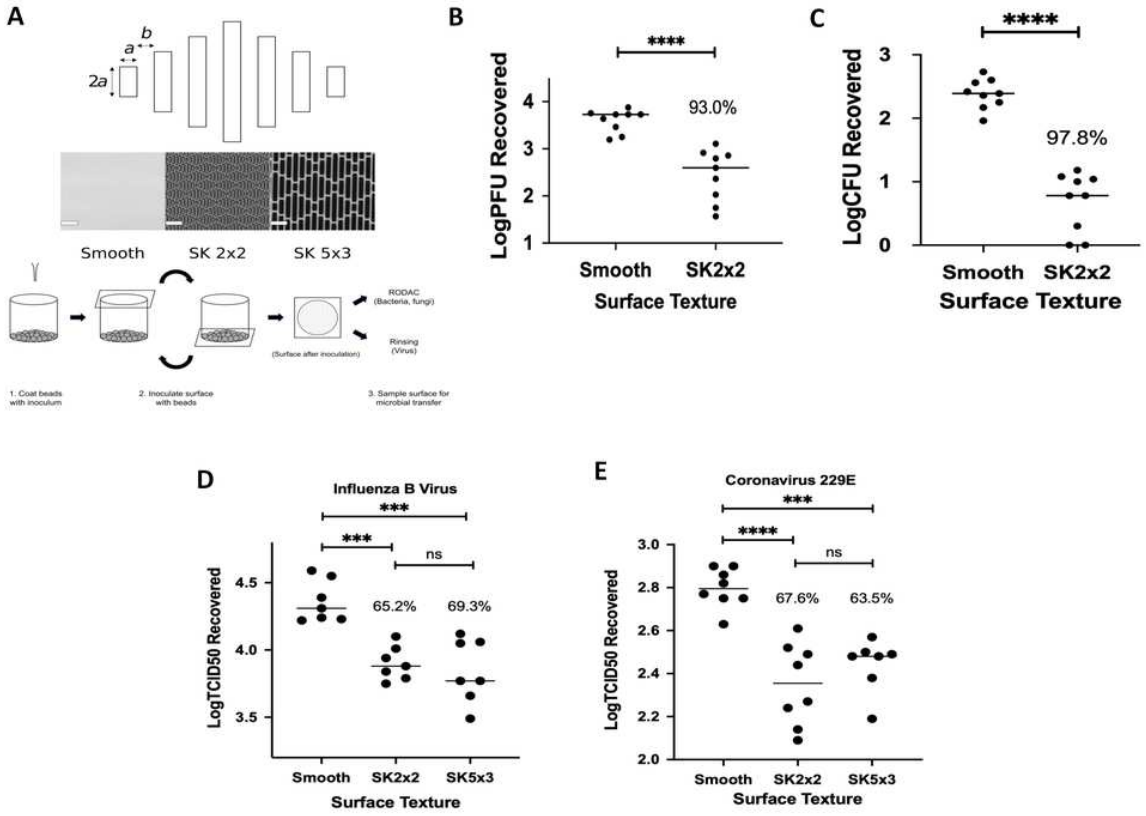


Figure 2.3 **A)** Sharklet micropatterns and the bead transfer method; **B)** Transfer of *S. aureus* on silicone surfaces (*** $p < 0.001$; **** $p < 0.0001$); **C)** Transfer of *Bacteriophage T4* on silicone surfaces. Smooth or SK2x2 micropatterned silicone samples were tested against *Bacteriophage T4* using beads transfer method; **D-E)** Transfer of human viruses on silicone surfaces [125].

Effects of Sharklet surface topography on mammalian cell adhesion and proliferation were studied by Mobini *et al.* [124] using fibroblasts and Schwann cells. With the aim of producing a neural interface substrate that inhibited fibroblasts involved in foreign body reactions while promoting neural cells, various patterned Polyimide surfaces were designed and fabricated. For *in vitro* cell culture tests fibroblast and Schwann cell lines from adult rats were used and metabolic activity, immunocytochemistry, and morphology of adhered cells were studied. Results indicated that on patterned surfaces with 20 μm-wide channels with 2 μm spacing strongly promoted adhesion and alignment of Schwann cells while inhibiting fibroblasts at the same time. Overall, it was found that cell alignment and spreading on patterned surfaces with feature sizes at the range of 2-20 μm were indeed regulated by the pattern arrangement. For each topographical pattern this regulation varied among different cell types, however, no statistical differences were found between cellular responses based on the pattern of the surface which is due to the ability of cells to change their shape and adapt to the environment [124].

Based on the data reported for antibacterial properties of various sharkskin bioinspired designs, it is evident that sharklet pattern has superior potentials to be used in reducing surface associated bacterial infection. This product can be used to cover the surface of hospital beds, medical instruments, and walls but their lifespan and effectivity must be further studied under different environmental conditions like high or low heat and humidity, or different wards within the hospitals. As for non-medical uses, these antibacterial surfaces can be used to cover elevator buttons and door handles, subway train chairs and handles, and public bathrooms. But, prior to applying, an extensive field study must be conducted regarding their feasibility and cost effectiveness.

2.5 Sharkskin Biomimicked Surfaces

Contrary to the considerably high number of studies on sharkskin bioinspired surfaces, there have not been as many researches on the biological attributes of shark-

skin biomimicked surfaces. This phenomenon is most probably due to the standardization of prepared surfaces via biomimetic technique as a result of variation in topography shape and dimension between different shark types and the location on the body (Figure 2.1C).

2.5.1 Antibacterial Activities of Sharkskin Biomimicked Surfaces

Pu *et al.* [27] studied the anti-biofouling of sharkskin mimicked surfaces made of PDMS and polyurethane and their effect on wettability and drag reduction. By utilizing PDMS embedded elastomeric stamping (PEES) method, the authors produced flat and sharkskin mimicked surfaces that were later characterized by SEM images, water contact angle, protein adhesion, and algae adhesion tests. Reported data based on the Wenzel model of hydrophobic theory showed a significant difference between hydrophobicity of flat (WCA = 101°) and sharkskin mimicked (WCA = 119°) PDMS surfaces. Furthermore, the anti-biofouling properties of sharkskin mimicked PDMS was found to be superior to its flat counterpart (Figure 2.4A and 2.4B). It was reported that the layer of air fixated at the interface of the surface and the liquid is the key player in the reduced biofouling as well as increased WCA. Moreover, a 12.5% reduction in drag force was observed on sharkskin mimicked PDMS surfaces. It was addressed that the three factors of surface microtopography, air pockets at the interface, and hydrophobicity simultaneously lead to reduced bioadhesion [27].

In a similar study, H.-W. Chien *et al.* [125] studied the dimensions, roughness, wettability, and antibacterial properties of sharkskin mimicked PDMS surfaces with two distinct patterns. As shown in Figure 2.5, differences between patterns arose from the location on the body from where the skin piece was collected, the abdomen (A), and the fin (F). For the samples of abdomen skin, the following values were obtained for single denticle dimensions: 165-180 μm in length, 86 - 100 μm in width, and 10.5 - 13.5 μm in height. As for the fin, the length, width, and height were recorded at 145 - 165 μm, 64 - 70 μm, and 6.2 - 8.8 μm, respectively. The density of denticles was also measured and reported at 110-130 denticles/mm^2 for the abdomen sample and

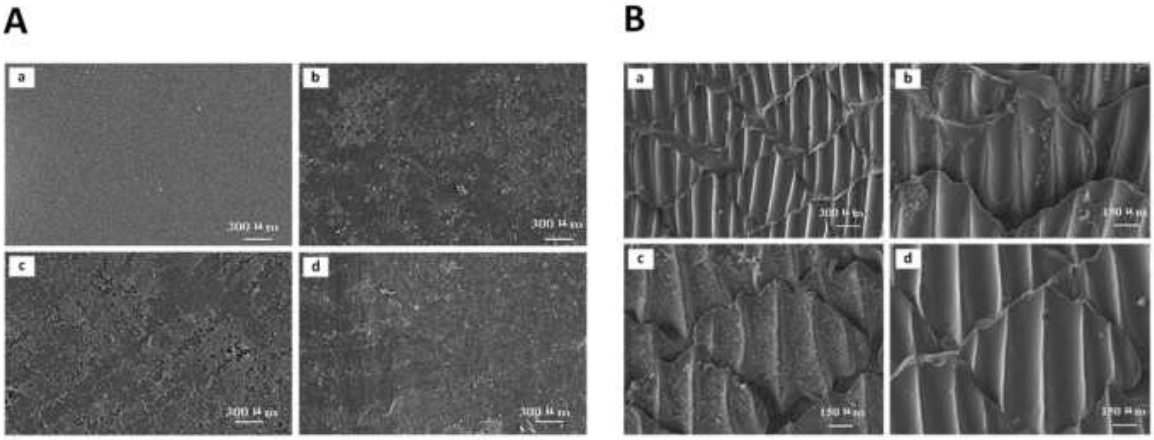


Figure 2.4 A) SEM images of algal cells adhered onto the surfaces of flat PDMS (F-PDMS) surfaces after being immersed in the Pearl River for various durations. (a) 1 day, (b) 21 days, (c) 70 days, (d) after being washed [27]; **B)** SEM images of algal cells adhered onto the biomimetic shark skin PDMS (S-PDMS) surfaces post immersion in the Pearl River for various durations. (a) 7 days, (b) 21 days, (c) 70 days, (d) after being washed [27].

80 - 130 denticles/mm^2 for the fin sample. The anti-biofouling test was conducted for two model bacteria stains, *S. aureus* and *E. coli*. Samples were incubated in 2 mL of the bacterial in a shaking incubator at 85 rpm for up to 14 days. According to the results, the dimensional variations, as well as denticle surface density, greatly affect its wettability and roughness properties as well as early-stage bacterial settlement and biofilm formation under dynamic culture conditions [125].

H-W Chien *et al.* [126] also produced sharkskin mimicked surface from photocatalytic titanium dioxide (TiO_2) nanoparticles at 0, 4, and 8 wt% concentration in polymethyl methacrylate (PMMA) via replication from PDMS negative mold. *In vitro* bacterial biofilm formation test was performed using *E. coli*. Sharkskin mimicked 8 wt% PMMA/TiO_2 nanocomposite surfaces prevented full-thickness biofilm formation for up to 14 days which was attributed to the synergistic antibacterial, photocatalytic, and structural effects [126].

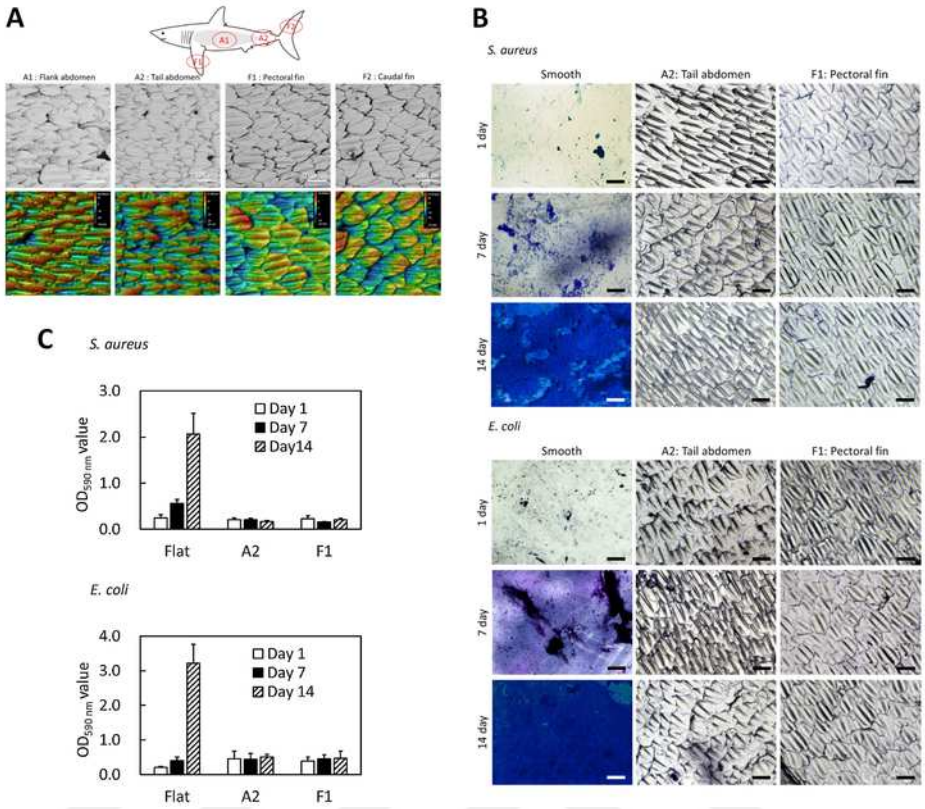


Figure 2.5 **A)** SEM (upper) and CLSM (lower) images of the Mako shark skin surface at different body locations; **B)** The residual biofilm of (a) *S. aureus* and (b) *E. coli* was quantified by crystal-violet staining; **C)** Investigation of biofilm formation by (a) *S. aureus* and (b) *E. coli* on smooth and biomimetic shark skin surfaces. Scale bar = 100 μm [127].

2.5.2 Medical Applications of Sharkskin Biomimicked Surfaces

A study into possible medical application of sharkskin-inspired surfaces in biosensors was done by H.-H. Jang *et al.* [127]. Using a negative PDMS mold of sharkskin, a flexible piezoresistive pulse sensor (FPPS) was designed and fabricated. The potentials of this sharkskin biomimicked sensor in *in vivo* detection and quantification of physiological cues were studied. The sensor part was made of PEDOT:PSS thin film which was coated onto the negative PDMS mold. The contact resistance which is a major issue of sensors was reduced by nearly 700 fold at a pressure below 500 Pa as a result of sharkskin topography as opposed to PEDOT:PSS flat control sensor. Additionally, the Reflection Index (R.I.) and Stiffness Index (S.I.) of the physiological pulse signal of a human subject were measured at 64.03% and 6.73 m/s, respectively. The

actual reading of these values were 48.19 ± 9.51% and 5.72 ± 0.28 m/s which in the authors'opinion were very close to the FPPS readings. The obtained data suggested that sharkskin topography can be useful in troubleshooting standard sensors [127].

Y.-T. Lin *et al.* [128] designed a novel wound dressing with sharkskin biomimicked topography on one side and a micro-channled 3D structure on the other. The authors studied the impact of sharkskin micropattern wound repair characteristics. PDMS was used to produce the bionic polymeric surface which was modified firstly with polyvinyl alcohol (PVA) and then again with 2-methacryloyloxyethyl phosphorylcholine (MPC) in the form of surface coatings applied to the surface via atmospheric plasma-induce surface activation and polymerization technique. Apart from chemical modifications, the surface topography of 3 different species of the sharkskin was replicated as shown in Figure 2.8 and bacterial adhesion on *Etmopterus Lucifer* proved to have the least bacterial adhesion rate. The final product named "PDMS-PVAPMPC" membranes acted as a double-sided substrate which exhibited superhydrophobic antibacterial properties on the outer layer and superhydrophilic characteristics on the inner layer, suitable for absorption of wound exudates, eventually accelerating the repair process. In addition to its antibacterial feature, the fabricated membrane showed acceptable biocompatibility, making them a high-potential candidate for bifunctional wound dressings, one which increases the speed of healing, due to the presence of PMPC and PVA, at the same time as it prevents bacterial infection at the wound site, as a result of sharkskin micropattern [128].

The overall findings suggest that similar to sharkskin bioinspired surfaces, sharkskin biomimicked surfaces possess remarkable potentials in reducing bacterial colonization and biofilm formation. Unlike sharkskin bioinspired surfaces that did not have any effect on mammalian cells, the sharkskin mimicked membranes enhance mammalian cell growth and proliferation.

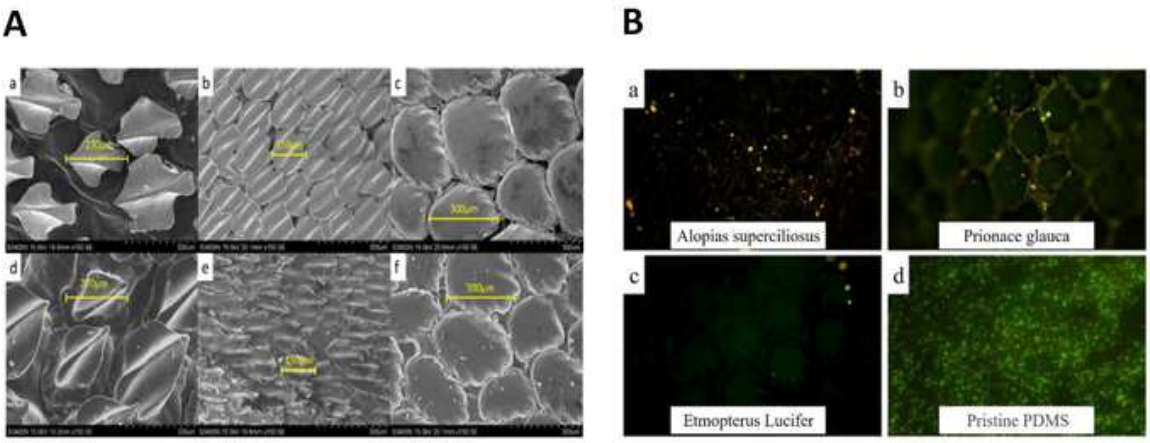


Figure 2.6 **A)** SEM images of the actual skin topography of *Etmopterus Lucifer* (a), *Alopias superciliosus* (b), and *Prionace glauca* sharks (c), Biomimicked PDMS surfaces with microtopography of *Etmopterus Lucifer* (d), *Alopias superciliosus* (e), and *Prionace glauca* (f) [130]; **B)** *E. coli* adhesion on the surface of (a) *Alopias superciliosus*, (b) *Prionace glauca* and (c) *Etmopterus Lucifer* and (d) pristine PDMS membrane [130].

2.6 Surface Associated Infection

Among all possible surgical complication, device related infections play a major role. Device-related infections (DRIs) essentially arise from surface infection which occur after bacterial adhesion and proliferation on the surfaces of biomedical devices and implants. These infections are a significant issue in implantable device surgeries as well as with biomaterials. Surface associated infection of implants often are diagnosed at late stages, hence they pose a considerable risk to patients'health. Therefore, they often requiring re-operation and replacement of the infected device, and are very costly. The severity of these infections varies greatly among devices and patients, however it can be serious and/or even fatal in some cases. Unfortunately, since most implantable devices lack the means by which early warning symptoms of bacterial infection can be detected, the onset of an infection is mostly concealed with the continued post-surgery inflammatory events. As a result, DRI diagnosis is frequently made only after a full-blown infection has already caused substantial tissue damage. The re-operation of contaminated implants has resulted in the death of elderly individuals who were already vulnerable due to the previous surgery or other factors.

2.7 Chitosan

The alkaline deacetylation of chitin, which is a major component of the protective cuticles of many crustaceans such as crabs, shrimps, prawns, and lobsters, as well as the cell walls of several fungi such as aspergillus and mucor, produces a natural linear bio-polyaminosaccharide known as Chitosan (CH). CH is a low-cost, biodegradable, and a non-toxic substance. CH, as a result of its deacetylation, has the additional features of water solubility, biodegradability, and biocompatibility, and is known to have several interesting biological activities, including antibacterial, anticancer, and hemostatic activity, as well as the acceleration of wound-healing process. Due to these properties CH has shown remarkable applications in the biomedical field. In this instance bone tissue, skin tissue, Tendon and ligament, Cartilage, Liver are fields in tissue engineering that have been using CH as a suitable choice among other polymers [129].

Moreover, CH possess numerous advantages over other type of polymers because it has a higher antibacterial activity and a broader spectrum of activity against several bacterial strains with a relatively high killing rate, and a extremely low toxicity toward mammalian cells [130],[131]. In some researches, it has been shown that the presence of quaternary ammonium salts, such as N,N,N-trimethyl , N-propyl-N,Ndimethyl , and N-furfuryl-N,N-dimethyl increased the antibacterial activity of CH against *Escherichia coli* when CH is dissolved in acidic medium compared to when it is dissolved in water. Thus, it was concluded that there is a correlation between the antibacterial activity of CH solution and potency of the solvent. In terms of antibacterial activity, CH is more soluble and has better antimicrobial action than chitin at pH values below 6 which is most probably due to the positive charge on the C-2 of the glucosamine monomer. The specific mechanism of chitin, CH, and their derivatives'antibacterial effect is unknown, but various processes have been hypothesized [132].

Interaction between positively charged CH molecules and negatively charged microbial cell membranes leads to the leakage of proteinaceous and other intracellular constituents. For example, fermentation with baker's yeast is inhibited by certain cations that act at the surface of the yeast cell in order to prevent glucose from entering

the cell. Furthermore, the impact of molecular weight on antibacterial and antifungal activity has been investigated. CH with a molecular weight of 10000 to 100000 would be beneficial in limiting bacterial development. Furthermore, the antibacterial activity of CH is affected by its degree of deacetylation, the CH concentration in the solution, and the acidity of the solvent [131],[133].

All these properties and characteristics make CH an ideal choice for our purposes. But CH alone is not capable of terminating bacteria to the necessary extent. Therefore, in the process of preparing membranes with antibacterial properties using polymers, some pre- and post- modifications must be done in order to increase the antimicrobial property of the fabricated membrane such as addition of chemicals with antibacterial property like Graphen Oxide (GO), Caffeic acid phenethyl ester (CAPE) and Ampicillin sodium salt (Amp).

2.8 Graphene Oxide

GO, a carbon based substance with large surface area and numerous functional groups in its structure, will also be used in order to enhance cyto-compatibility and antibacterial activity at the surface of the fabricate envelope [134–136]. GO, a well-known derivative of graphite, is in the form of pseudo-two-dimensional oxygencontaining sheets or flakes at nano-scale thickness with sharp edges which possesses multiple functional groups, namely hydroxyl, epoxy, and carboxyl [32]. Moreover, GO flakes own nano-scale surface roughness and due to their high surface area, they can impose strong geometric restrictions to the mobility of polymer molecules [137–139]. Recent studies have attributed antibacterial effect of GO to membrane stress induced by sharp edges of its flakes and presence of highly active functional groups at the edges which most probably induces physical damages to the cell wall, resulting in the loss of bacterial membrane integrity, leading to the leakage of RNA [139],[140].

2.9 Caffeic acid phenethyl ester (CAPE)

In recent years, many studies about natural products have been conducted; one of these components is CAPE, which is known to be a potent inhibitor of activation of NF-κB [141]. A major part of CAPE bioactivities is thought to be related to NF-kB inhibition [142]. CAPE is also an anti-inflammatory and antioxidant agent with antiviral, antibacterial, and antifungal effects, according to studies [143].

CAPE's antibacterial mechanism of action was discovered in studies on the *in vitro* inhibitory effects of an aqueous extract of CAPE against distinct Gram positive and Gram negative bacteria. According to the findings, CAPE efficiently suppressed the growth of the majority of Gram positive bacteria tested, while having a modest effect on a subset of Gram positive bacteria and all Gram negative bacteria tested. The authors theorized that this selective effect was due to the presence of a capsule surrounding these bacteria, which prevented the tested items from penetrating the bacteria. Hence, only little amounts of the compounds could permeate into the capsular bacteria and somewhat alter their growth at very high doses of the products [144].

2.10 Ampicillin Sodium Salt

Amp also has antibacterial property except in this case, the mechanism of defeating bacteria differs in a way that ampicillin is a drug synthesized for killing bacteria. Ampicillin sodium salt is a β-lactam antibiotic that works against both gram-positive and gram-negative bacteria. It is commonly used to treat infections. The majority of medications can be administered through a variety of routes, which are essentially classified as local and systemic. Because systemic antibiotic treatment can result in a variety of side effects (sensitivity, resistant strains, and super infections), local antibiotic administration has gotten a lot of the attention. For instance, an adequate drug concentration at the site of action, as well as a way of maintaining that level for a long enough duration to allow the agent to act, are required for the efficient use

of antibacterial agents in the treatment of periodontal disorders. Studies conducted on antibacterial effects of ampicillin sodium salt have concluded that it retains its antimicrobial efficacy after being incorporated into the polymer solution and twisted into yarns, and released this antimicrobial agent is considerably effectively against *S. aureus* [145],[146].

So far, it can be proposed that presence of CAPE, GO, and Amp will equip the shark skin mimicked polymeric membranes with antibacterial property. The proposed hypothesis in this thesis aims to investigate whether addition of antibacterial agents and antibiotics can be ruled out due to the significance of sharkskin micro-pattern's antibacterial effect. By combining these materials and sharkskin topography, antibacterial surfaces with numerous biomedical applications can be fabricated namely surface covering material for implantable cardiovascular devices.

3. BIFUNCTIONAL SHARKSKIN MIMICKED CHITOSAN/GRAPHENE OXIDE MEMBRANES: REDUCED BIOFILM FORMATION AND IMPROVED CYTOCOMPATIBILITY

The two most significant features that an ideal implanted biomaterial must have at the same time are antibacterial activity and cytocompatibility. Biomaterials with these qualities can be made by combining chemical and topographical factors. This research looked at the design and fabrication of a sharkskin-like GO-modified CH membrane with improved antibacterial and cytocompatibility properties. The viability of planktonic and bacterial biofilm was tested against Gram-positive *S. aureus* and Gram-negative *E. coli* to determine antibacterial capabilities. Furthermore, cell viability and proliferation of cultured HaCaT and L929 cell lines were studied both on plain and sharkskin mimicked membranes.

3.1 Experimental

3.1.1 Materials

A Basking Shark (*Cetorhinus maximus*) was supplied from a local fisherman. Low molecular weight chitosan (50,000-190,000 Da), Glacial acetic acid (99%), Absolute ethanol, Glutaraldehyde (25% in H_2O), Sodium hydroxide (NaOH) (anhydrous, pellets), and Graphene Oxide (2 mg/mL) were purchased from Sigma Aldrich. Sylgard 184 PDMS was bought from Dow Chemical.

3.1.2 Preparation of Chitosan-Based Membrane

Chitosan solution was prepared by dissolving 2.5 g of purified chitosan in 2.5% aqueous acetic acid solution and stirred overnight. To prepare CH/GO nanocomposites,

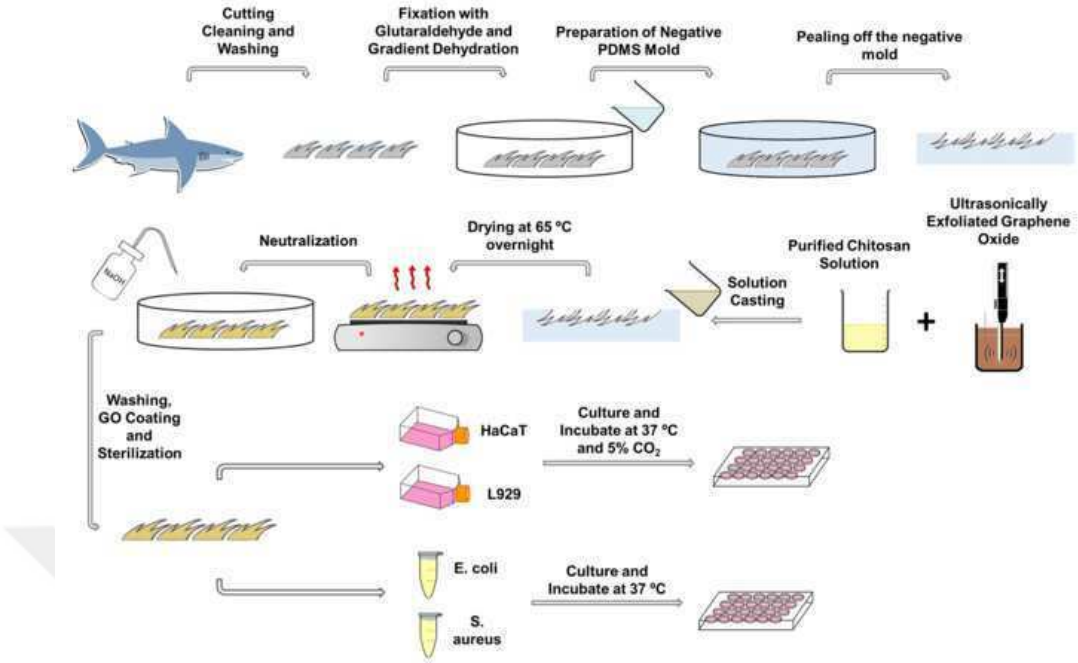


Figure 3.1 Schematic representation of overall experimental procedures.

GO solution was exfoliated using an ultrasonic homogenizer at 50 kHz for 30 min in an ice bath prior to addition to CH solution. GO/CH nanocomposite solutions were prepared by addition of GO to CH at 3 different concentrations: 0.1, 0.2 and 0.3 %wt which were designated as GO1, GO2, and GO3, respectively (Table 3.1). Then, the solution was ultrasonicated for 1 h in ice bath followed by mixing for another 3 h by magnetic stirring [35],[147]. CH based membranes were prepared by solution casting method. Briefly, solutions were poured onto sharkskin negative mold and smooth PDMS substrate to fabricate sharkskin mimicked and plain membranes, respectively. Samples were degassed for 60 min under vacuum to remove air bubbles and then dried in the oven at 65°C overnight. Afterwards, dried membranes were collected and submerged in 1M NaOH solution for 60 min, followed by rinsing with dH_2O prior storing at +4°C for further use [148],[149]. In order to coat the CH membranes with GO, 0.5 mg/mL solution of GO was prepared and exfoliated using an ultrasonic homogenizer at 50 kHz for 60 min in ice bath. Afterwards, the dried membranes were subjected to UV-Ozone treatment for 2 min, then submerged in the solution of exfoliated GO and kept at 4°C overnight. Samples were then washed twice with dH_2O and stored at 4°C

for further use [150].

Table 3.1
Experimental groups of CH/GO nanocomposites and their chemical contents.

Abb.	g CH	mg GO
CH	2	0
GO1	2	2
GO2	2	4
GO3	2	6
GOc	2	Coated

3.1.3 Fourier-Transform Infrared Spectroscopy (FTIR)

In order to study the intermolecular interactions between CH and GO in fabricated membranes, FTIR spectra of were examined using Perkin Elmer, Spectrum 100, USA in the range of 4000 - 400 cm^{-1} [151],[152].

3.1.4 Water Contact Angle (WCA)

Water contact angles were measured by Biolin Scientific Attension Theta instrument using dH_2O at room temperature (RT). Samples were put on an adjustable sample stage then a drop of approximately 15 μL of distilled water was placed on the surface of the samples using a micro-syringe [153].

3.1.5 L929 and HaCaT Cell Culture on Plain Membranes

In order to understand the effect of chemistry regardless of surface topography, the interactions between mammalian cell lines and plain membranes were investigated by measuring cell viability, proliferation and morphology. To this aim, mouse fibroblast

from mouse adipose tissue (L929) and Human Keratinocyte (HaCaT) cell lines were chosen as mammalian model cell lines. All other chemicals and supplements used in the cell culture were purchased from Sigma Aldrich unless mentioned otherwise. Both L929 and HaCaT cells were seeded at cell density of $1.5x10^4$ cells per well in 24 cell culture treated well plates using DMEM (Dulbecco's modification of Eagle medium) and RPMI-1640 Medium, respectively. Growth mediums were supplemented with 10% v/v Fetal Bovine Serum (FBS) and 1% v/v antibiotic (penicillin-streptomycin) and viability, proliferation and morphology tests were performed on days 1, 3, and 5 [20],[41],[154].

3.1.5.1 Cell Viability (MTT Assay). Viability and proliferation of cells were quantified using 3-(4,5-dimethylthiazol-2-yl)-2,5-diphenyltetrazolium bromide (MTT) and AlamarBlue assays. To this end, MTT solution with concentration of 5 mg/mL was prepared in filtered Phosphate Buffer Saline (PBS) (pH = 7.2) and added to the cell medium at the ratio of 1:10 followed by 3.5 h incubation at 37°C. Then, the medium was disposed and Dimethyl sulfoxide (DMSO) was added to dissolve formazan crystals. Absorbance measurements were done using a Bio-Rad iMark Microplate Reader at 570 nm and 750 nm wavelengths as measurement and reference filters, respectively [155],[156].

3.1.5.2 Cell Proliferation (AlamarBlue Assay). The AlamarBlue assay, which uses a water-soluble colorimetric oxidation-reduction indicator to measure cytotoxicity or proliferation using spectrophotometry, includes a colorimetric oxidation-reduction indicator that changes color in response to the chemical reduction of the culture medium caused by cell growth (metabolic activity). To perform this assay on days 1, 3, and 5, a 10% v/v mixture of AlamarBlue reagent in culture medium was prepared and added to each test well of 24 well plate. After 3 h incubation at 37°C, 5% CO_2, absorbance of supernatant was at 570 nm measurement filter (reduction) and 590 nm background filter (oxidation). Relative cytotoxicity was calculated with respect to tissue culture plate (TCP) [157].

3.1.5.3 Immunofluorescent (IF) Staining. Cultured cells on membranes were stained with Alexa Fluor 488 conjugated phallotoxin to stain actin filaments of cytoskeleton and DAPI (4', 6-diamidino-2-phenylindole) in order to observe cell nucleus. Prior to staining, samples were immersed in fixation solution (3.7% w/v Formaldehyde in PBS) for 10 min at RT and washed with PBS twice afterwards and kept at 4°C for future staining. Briefly, cells were permeabilized using 0.1% v/v Triton X-100 solution in PBS and blocked with 1% v/v Bovine serum albumin (BSA) solution in PBS. Then 9 μL of stock solution of Alexa 488 stain was added to fresh BSA solution of each well and incubated at RT on a gentle shaker for 20 minutes [158]. After washing the samples twice with PBS, DAPI counter stain was added and gently shook for 3 minutes. Fluorescence microscope (Leica DFC 295) was used for imaging.

3.1.6 Bacterial Culture Tests

3.1.6.1 Antibacterial Activity Test (ISO 22196). Loss of planktonic bacterial viability during first few hours of contact was measured according to the ISO 22196 international standard [159],[160]. Briefly, bacteria suspensions with 0.5 OD_{600} of *S. aureus*(ATCC 6538P) and *E. coli* (ATCC 8739) were prepared in PBS. Then 10 μL of each bacteria suspension was placed on each sample of sterilized plain and shark-skin mimicked membranes and a non-adherent plastic sheet (1cm x 1cm) was placed on the droplet to ensure the even spread of droplet on the surface for all samples. After incubation at RT for 3 h, samples were washed with 10 mL PBS and shook for 10 min at 200 rpm to detach adhered bacteria. Finally, 100μL of each solution was spread on Lysogeny broth (LB) agar and incubated at 37°C overnight. Colony Forming Units (CFU) were counted and normalized with respect to control group, droplet spread on non-adherent plastic sheet, to calculate loss of viability [159],[160].

3.1.6.2 Bacterial Biofilm Formation (MTT Assay). Bacterial biofilm formation rate was measured as an indicator of biofilm formation on CH-based membranes. *S. aureus* and *E. coli* were used as gram-positive and gram-negative model organisms,

respectively. 100 μL of overnight grown suspensions of each strain were added in 10 mL LB medium and supplemented by 100 μL of 50% w/v glucose solution to support biofilm formation. Then sterilized plain and sharkskin mimicked membranes were placed in wells of 24 well plates and 750 μL of prepared bacterial suspension (pH=7.0) was added onto each sample. Plates were incubated at 37°C for 24 h in stationary incubator. Afterwards, samples were removed from 24 well plates, gently immersed in PBS 3 times to remove the unattached bacteria. Then MTT [3-(4,5-dimethylthiazol-2-yl)-2,5-diphenyl-tetrazolium bromide] assay was performed to evaluate the viability by means of percentage metabolic activity of the biofilm formed on the membranes in comparison to that of TCP which was the control group [161].

3.1.6.3 Morphology of Adhered Bacteria. SEM imaging was used to obtain information regarding bacterial adhesion behavior of plain and sharkskin mimicked membranes. To this, a suspension of 10^4 bacteria/mL was prepared by serial dilutions from an overnight grown culture. Plain and sharkskin mimicked membranes were sterilized by immersion in ethanol for a few hours followed by UV treatment of each side of membranes for 2 h. Then 2.5 mL LB was added to each 15 mL conical test tube and 100 μL of bacterial suspension was added and mixed. After 24 h incubation at 37°C in a stationary incubator, samples were fixated using glutaraldehyde solution, prepared in PBS, at RT for 30 min followed by PBS washes twice and dehydration with 30%, 50%, 75%, 80%, 95% and 100% v/v ethanol aqueous solutions each for 15 min. Then samples were treated with Hexamethyldisilazane (HMDS) and dried slowly under fume hood overnight. Prior to imaging, all samples were coated with a 5 nm-thick layer of gold and SEM images were captured at 5.00 kV voltage and 15mm working distance.

3.1.7 L929 and HaCaT Cell Culture on Sharkskin Mimicked Membranes

In order to study the dual effect of sharkskin surface microtopography and GO, the interactions between mammalian cell lines and biomimicked membranes was investigated by measuring cell viability (MTT assay), proliferation and adhesion morphology

(SEM imaging) as mentioned above. L929 and HaCaT cells were cultured at cell density of $1.5x10^4$ cells per well in 24 well plates and all measurements were done on days 1, 3, and 5 [162],[163]. Cell viability and proliferation were measured via MTT and AlamarBlue assays respectively, as mentioned in section 3.1.5. Morphology of adhered cells was studied via SEM imaging. (See section 3.1.6.3)

3.1.8 Statistical Analysis

All data are presented as mean ± SD for 3 biological repetitions and statistical evaluations were done using one-way ANOVA with p-value<0.05 was considered statistically significant. Statistical significances are designated with letters. Groups with different letter designations are statistically significantly different.

3.2 Results

3.2.1 FTIR and Water Contact Angle

FTIR spectra of CH, GO and GOc membranes were obtained to detect structural changes in the functional groups of CH-based polymeric membranes. Results are shown in Figure 3.2. The spectrum of CH shows its characteristic peaks at 1022 and 1158 cm^{-1} attributed to alcoholic group of C6-OH and secondary alcoholic group of C3–OH, 1075 cm^{-1} related to stretching vibration of C–O–C functional group, 1398 cm^{-1} assigned to stretching and vibration of C-O and C-H, 1573 cm^{-1} corresponding to primary amine ($-NH_2$), 1642 cm^{-1} assigned to amide groups (carbonyl stretching vibration of -HNCOgroups), 2937 and 2972 cm^{-1} representing symmetric aliphatic -CH, asymmetric aliphatic -CH bands, and 3317 cm^{-1} , and 3394 cm^{-1} corresponding to N-H and -OH stretching vibrations, respectively [153],[164]. In GO and GOc spectra, all characteristic peaks of CH appear to have slightly shifted. It can be seen from the spectra that all peaks assigned to amine and amide groups become sharper because of the presence of GO in the polymeric network of CH. This higher intensity is observed

in GOc groups with even sharper peaks than that of GO2. This increase in peaks intensity suggests that conjugation of GO with CH took place via formation of chemical bonds between -NH_2 groups of CH and functional groups of GO [164],[165].

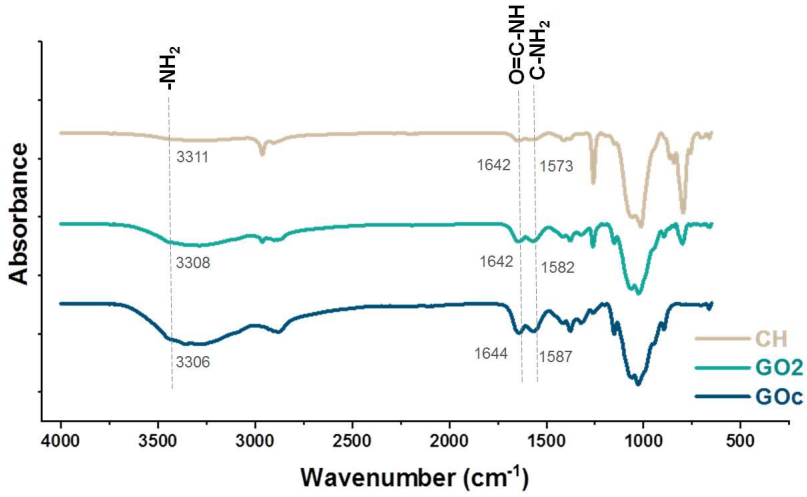


Figure 3.2 FTIR spectra of CH, GO and GOc membranes (CH: chitosan, GO2: 0.2%wt graphene oxide/chitosan nanocomposite, GOc: graphene oxide coated chitosan).

Water contact angle measurements were performed for both plain and sharkskin mimicked membranes. It is evident from the obtained results (Figure 3.3) that in plain membranes addition of GO to CH changes the water contact angle, significantly. Water contact angle of plain CH membrane was measured as 81.85°which is in agreement with reported literature [153],[166]. After GO is added to CH and as its concentration increases from 0.0 to 0.1% wt and again to 0.2% wt, the contact angle decreases but when the GO content reaches 0.3% wt (GO3), the contact angle increases and the hydrophilic surface suddenly becomes hydrophobic [153]. Similar fluctuation in WCA values for GO/CH composites is reported by Maraschin *et al.* [167].

3.2.2 L929 and HaCaT Cell Culture on Plain Membranes

Cell viability and proliferation rate of cultured HaCaT and L929 cell lines on plain membranes were evaluated. Cells were seeded at the cell density of $1.5x10^4$ for duration of 5 days. On days 1, 3, and 5, MTT and AlamarBlue tests were performed for

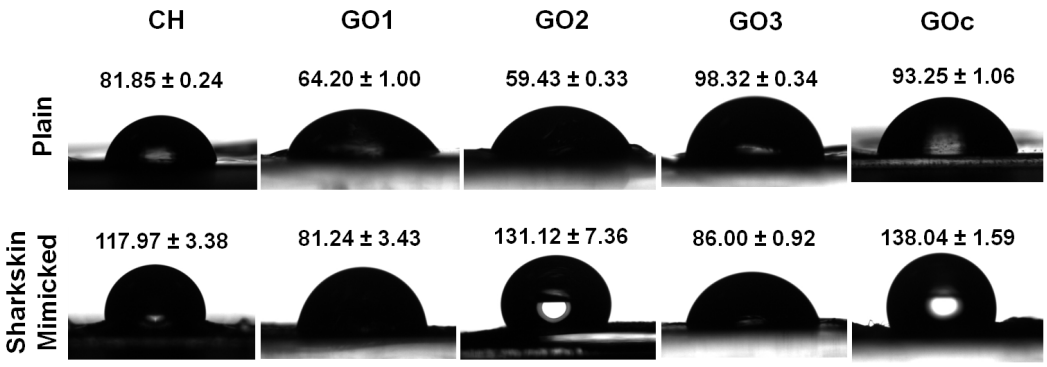


Figure 3.3 Water contact angle results for plain and sharkskin mimicked membranes (Mean ± SD, n=5) (CH: chitosan, GO: graphene oxide, GO1, GO2, GO3: 0.1, 0.2, 0.3 %wt graphene oxide/chitosan nanocomposites, GOc: graphene oxide coated)

cell viability and proliferation assessment with respect to TCP as the positive control and CH as the negative control (Figure 3.4 and 3.5). IF staining was also done as the morphological characterization of adhered cells and its results are represented in Figures 3.6. As shown in Figures 3.4A and 3.4B, on day 5 the highest cell viability of both cell types belongs to GOc group where the cell density of L929 has increased nearly 400% within 5 days. Similarly, viability of HaCaT cells increased as well to almost 200% that of the initial seeding density [150]. The cell viability sequences are as follows: for L929: GOc > GO2 > GO3 > GO1 > CH and for HaCaT: GOc > CH > GO2 > GO1 > GO3. There is no statistically significant difference between nanocomposite groups in L929 in term of cell viability even though the cell viability is highest for GO2 group compared to that of GO1 and GO3 on day 5. However, for HaCaT, cell viability on GO2 is significantly higher than GO1 and GO3. It is evident from the obtained results that GO coating has the highest potential to promote cell adhesion and proliferation which is in agreement with reported literature [150].

Similar results have been reported for cell viability on GOc and conjugated polymers. P. Sangsanoh *et al.* reported similar cell viability results on plain CH membranes [163]. Also Zuo *et al.* report promising results for adhesion and viability of mouse mesenchymal stem cells to GO/CH nanocomposites [40].

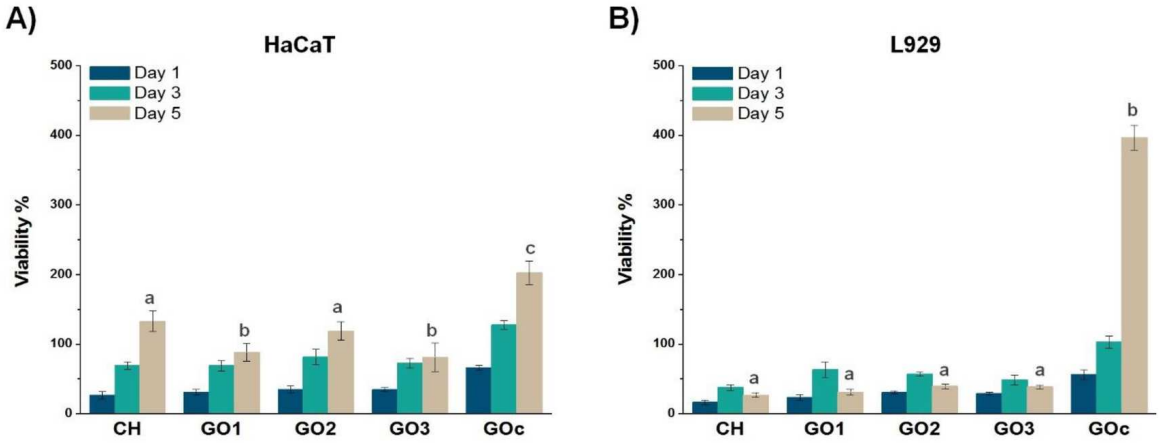


Figure 3.4 Cell culture results of HaCaT and L929 on plain membranes. **A)** Cell viability of HaCaT on plain membranes (MTT assay), **B)** Cell viability of L929 on plain membranes (MTT assay), (Mean ± SD, n=4; CH: chitosan, GO1, GO2, GO3: 0.1, 0.2 and 0.3%wt graphene oxide/chitosan nanocomposite, GOc: graphene oxide coated chitosan)

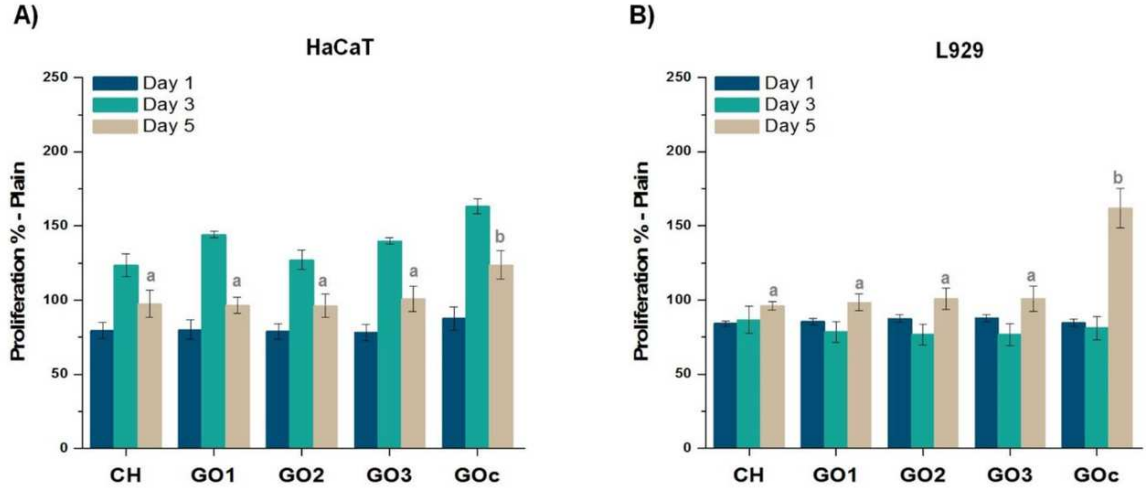


Figure 3.5 Cell culture results of HaCaT and L929 on plain membranes. **A)** Cell proliferation of HaCaT on plain membranes (AlamarBlue assay), **B)** Cell proliferation of L929 on plain membranes (AlamarBlue assay), (Mean ± SD, n=4; CH: chitosan, GO1, GO2, GO3: 0.1, 0.2 and 0.3%wt graphene oxide/chitosan nanocomposite, GOc: graphene oxide coated chitosan)

AlamarBlue results confirm the highest values of cell proliferation rate for GOc for both cell lines as well (Figure 3.5). High cell viability for GO2 among nanocomposites is most probably due to its high and stable water uptake ratio, highly hydrophilic nature along with having the highest percentages of -NH_2 and –NH_3 functional groups which may make it more polar than other nanocomposites.

IF staining results represented in Figure 3.6 show that cell number and their spreading behavior on GOc membrane is very similar to that of positive control (TCP) for both cell types. It seems that GO coating not only increased the proliferation rate but also improved adhesion, spreading and cytoskeletal development.

After comparing mammalian cell viability and proliferation results with physicochemical characterizations, it became obvious that despite the changes caused by conjugation of GO with CH in form of nanocomposite, no noticeable impact was induced on viability of HaCaT or L929 cells cultured on plain membranes. It is also obvious that coating GO onto CH membranes promotes surface properties in favor of cell adhesion, viability and proliferation. The study regarding effects of chemistry for fabricated membranes can be concluded at this step by selection of GOc as the best group. However, GO2 was chosen as the best group among nanocomposites in order to study the behavior of bacterial adhesion and process of biofilm formation on GO/CH nanocomposites. This selection was done based on cell viability results on plain membranes in which GO2 had the highest cell viability. Thus, for the remaining experiments the following groups were used as experimental groups: chitosan (CH) as negative control, 0.2 %wt graphene oxide/chitosan nanocomposite (GO2), graphene oxide coated chitosan (GOc), and graphene oxide coated 0.2 %wt graphene oxide/chitosan nanocomposite (GO2c). TCP was used as the control group.

3.2.3 Bacterial Culture Tests

3.2.3.1 ISO 22196 Test. Using ISO 22196 protocol, which is a quantitative measurement test for bacteriostatic and/or bactericidal capacity of plastic surfaces against

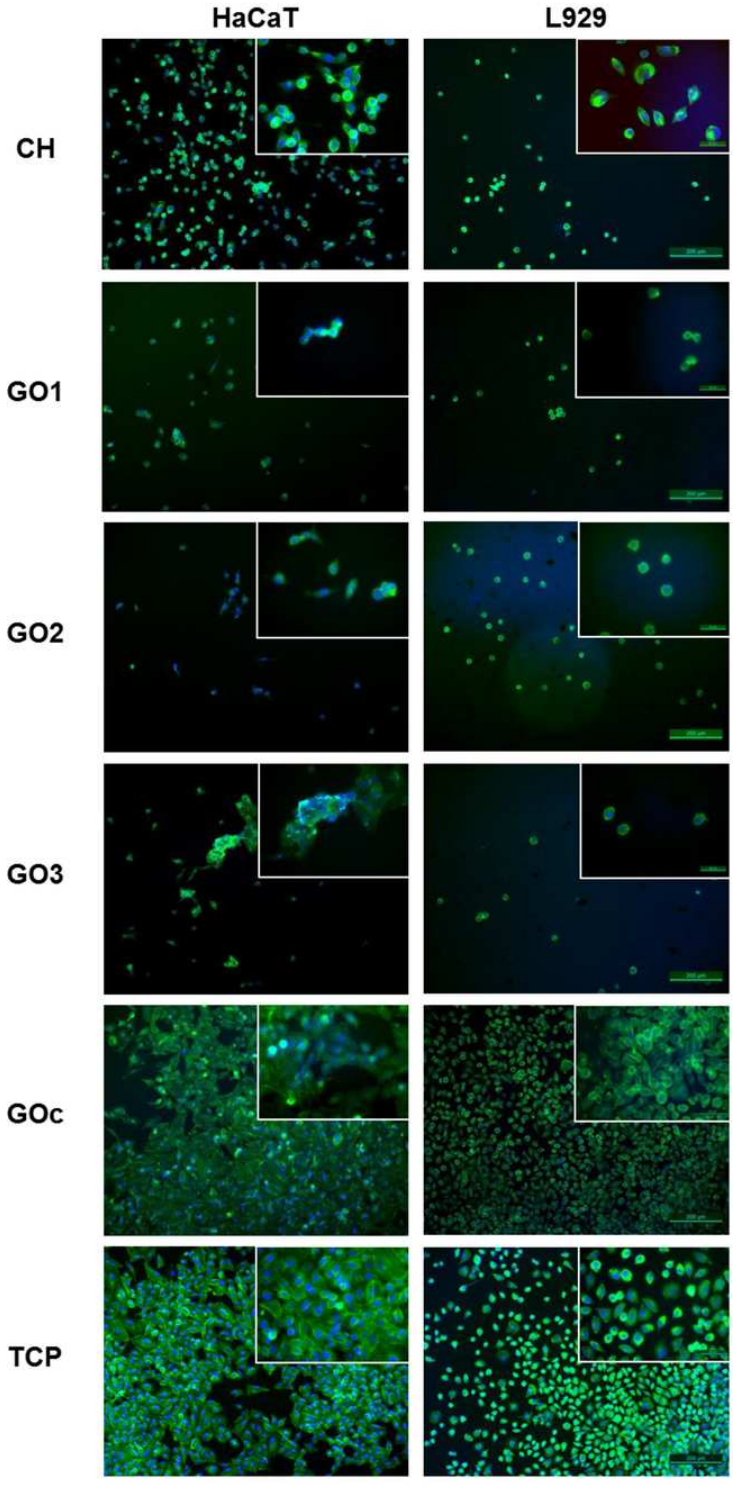


Figure 3.6 IF staining images of HaCaT and L929 cells stained with Alexa Fluor 488 phalloidin (green) and DAPI (blue) on day 3. Scale bars: 200μm and 50μm.

various microorganisms, antibacterial properties of prepared membranes towards planktonic bacteria during the early hours after initial contact were studied [159].As shown in Figures 3.7, there is a statistically significant difference between CFU counts of plain and sharkskin mimicked membranes with the same chemical composition for both *E. coli* and *S. aureus* proving the remarkable effect of sharkskin topography on bacterial adhesion. As for the effect of chemistry, plain membranes with different chemical compositions have similar percentage of live *E. coli* bacteria on the surface (Figure 3.7A). Similarly, sharkskin mimicked membranes with difference chemical compositions show no statistically significant difference in percentage of live *E. coli* bacteria on the surface. The reductions in CFU count of *E. coli* between plain and mimicked are as follows: CH: 80%, GOc: 76%, GO2: 77% and GO2c: 75%. As for *S. aureus*, there is a statistically significant difference between plain CH group and GO containing plain groups which is due to the high antibacterial activity of GO against gram positive bacteria. Sharkskin mimicked membranes have similar *S. aureus* CFU counts regardless of chemical compositions. The reductions in CFU count for *S. aureus* because of sharkskin topography are as the following: CH: 76%, GOc: 72%, GO2: 59% and GO2c: 79%. It is obvious that GO has considerably higher antibacterial activity against *S. aureus* than *E. coli* even during initial hours of attachment and adhesion onto smooth surfaces, hence the reduction of CFU count for mimicked membranes for *S. aureus* becomes less than that of *E. coli* similar to biofilm growth rate results [11],[168]. However, when the surface topography changes, the effect of surface chemistry on CFU count of *S. aureus* is incapacitated similar to that of *E. coli*. Overall, it can be concluded that during the initial phase of bacterial biofilm formation, which is attachment and adhesion of planktonic bacteria, the inhibitory effect of surface microtopography is far superior to chemical cues [169],[170].

3.2.3.2 Biofilm Growth (MTT assay). After measuring antibacterial activities during first hours of surface contact, MTT assay, which acts on metabolic activity of living cells, was used to measure growth rate of bacterial biofilm formed during a 24 h incubation period [161],[170]. By implementing this test, bacterial biofilm formation of *S. aureus* and *E. coli* strains were quantitatively measured and are represented in

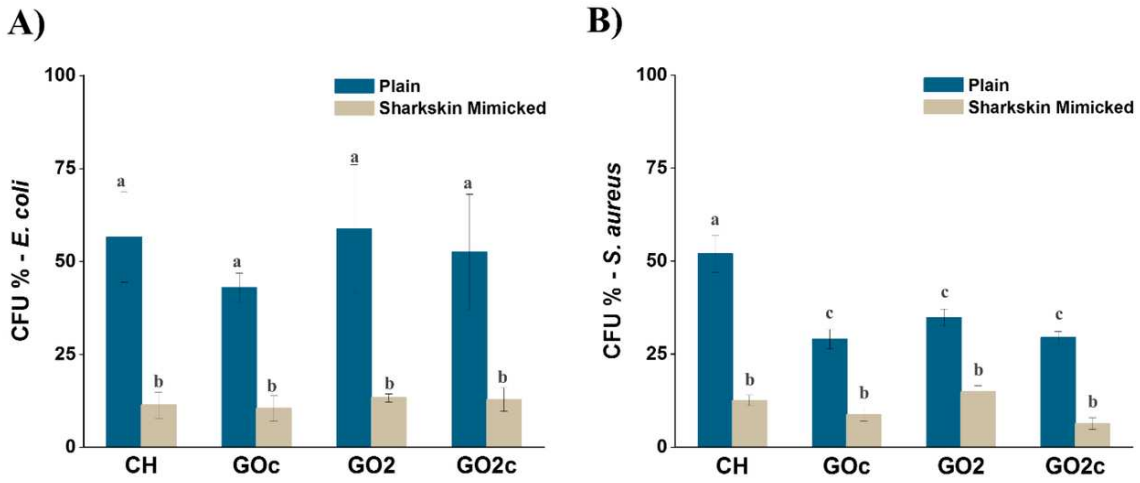


Figure 3.7 ISO 22196 test results, **A)** *E. coli*, **B)** *S. aureus*, (Mean ± SD, $p<0.05$, n=4; CH: chitosan, GO2: 0.2 %wt graphene oxide/chitosan nanocomposite, GOc: graphene oxide coated chitosan, GO2c: graphene oxide coated 0.2 %wt graphene oxide/chitosan nanocomposite)

Figures 3.8 (normalized with respect to TCP). As seen in Figure 3.8A, there is no statistically significant difference between bacterial biofilm growth rates among plain membranes with different chemical compositions for *E. coli*. The same trend was observed for sharkskin mimicked membranes with various chemical compositions as well. But, by comparing biofilm formation of plain and sharkskin mimicked membranes with same chemical composition, the effect of surface topography becomes very clear.

As shown in Figure 3.8A, there is a noticeable drop in biofilm growth between plain and sharkskin mimicked membranes of CH and GOc groups. Sharkskin micropattern reduced biofilm growth by nearly 45% in CH and 55% in GOc. Moreover, for GO2 and GO2c, it appears that the presence of GO in CH structure as nanocomposite, GO coated or not, reverses the effect of surface topography and results in higher amount of biofilm growth rate in *E. coli* cultured on mimicked membranes despite the statistical insignificance of it. Thus, presence of GO as surface coating on sharkskin mimicked CH is likely to be more effective in reducing bacterial biofilm formation than GO inside CH against *E. coli*.

For *S. aureus*, similar results to that of *E. coli* were obtained between plain

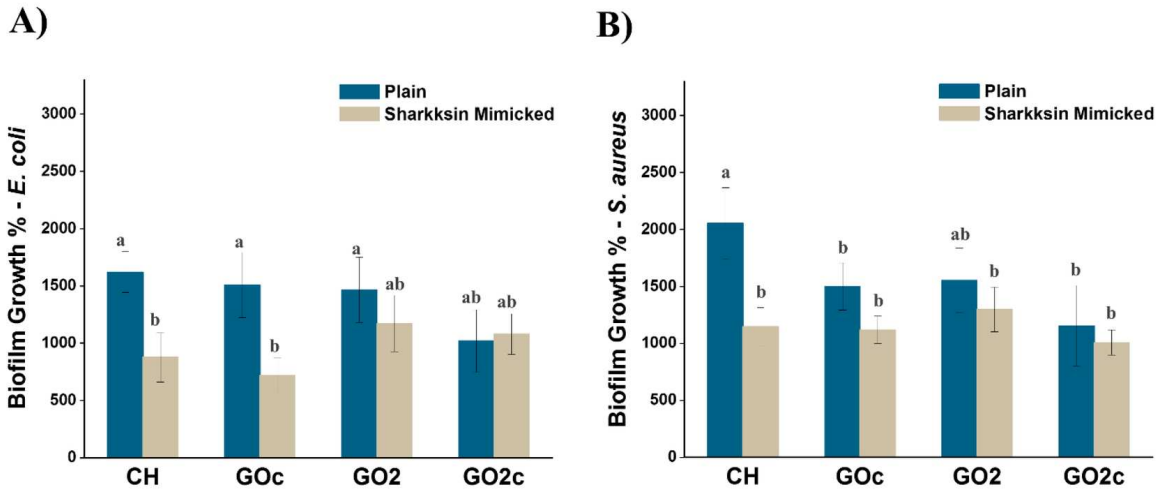


Figure 3.8 Bacterial biofilm growth on plain and sharkskin mimicked membranes (MTT assay) **A)** *E. coli*, **B)** *S. aureus*, (Mean ± SD, $p<0.05$, n=4; CH: chitosan, GO2: 0.2 %wt graphene oxide/chitosan nanocomposite, GOc: graphene oxide coated chitosan, GO2c: graphene oxide coated 0.2 %wt graphene oxide/chitosan nanocomposite)

membranes with varying chemical compositions and sharkskin mimicked membranes with varying chemical compositions with the single exception of CH vs. GOc in plain membranes (Figure 3.8B). There is no statistically significant difference between biofilm formation of mimicked membranes with various chemical compositions. As for plain membranes, biofilm growth of plain GO2 and GO2c groups show no difference however, there is a statistically significant difference between biofilm growth rates of plain CH and plain GOc which is attributed to antibacterial properties of GO.

Reduction of biofilm growth rate between plain and sharkskin mimicked GOc, GO2 and GO2c groups are significantly less than that of CH. The differences between the effect of GO on formation of biofilm of *S.aureus* and *E. coli* on mimicked surfaces show that, evidently GO is more effective in reducing bacterial biofilm growth rate in *S. aureus* than *E. coli*. In a similar study conducted by Krishnamoorthy *et al.* it has been reported that GO has higher antibacterial activity against gram positive bacterial than gram negative, which is in agreement with presented results [11],[171].

3.2.3.3 Biofilm Morphology. Since the antibacterial assessment tests performed so far cannot provide sufficient information regarding mechanism of reduction in bacterial viability, SEM imaging was used to observe bacterial morphology attached onto plain and sharkskin mimicked membranes. Obtained data are presented in Figures 3.9 and 3.10. As shown in the images, there is considerable difference between the numbers of adhered bacteria on plain and sharkskin mimicked membranes.

It is seen that there are significantly fewer bacteria on mimicked membranes than on plain membranes for both strains. SEM results agree with reported results of biofilm and planktonic bacteria viabilities as well as published studies on effects of topography and chemistry on antibacterial activity as mentioned previously [19],[125].

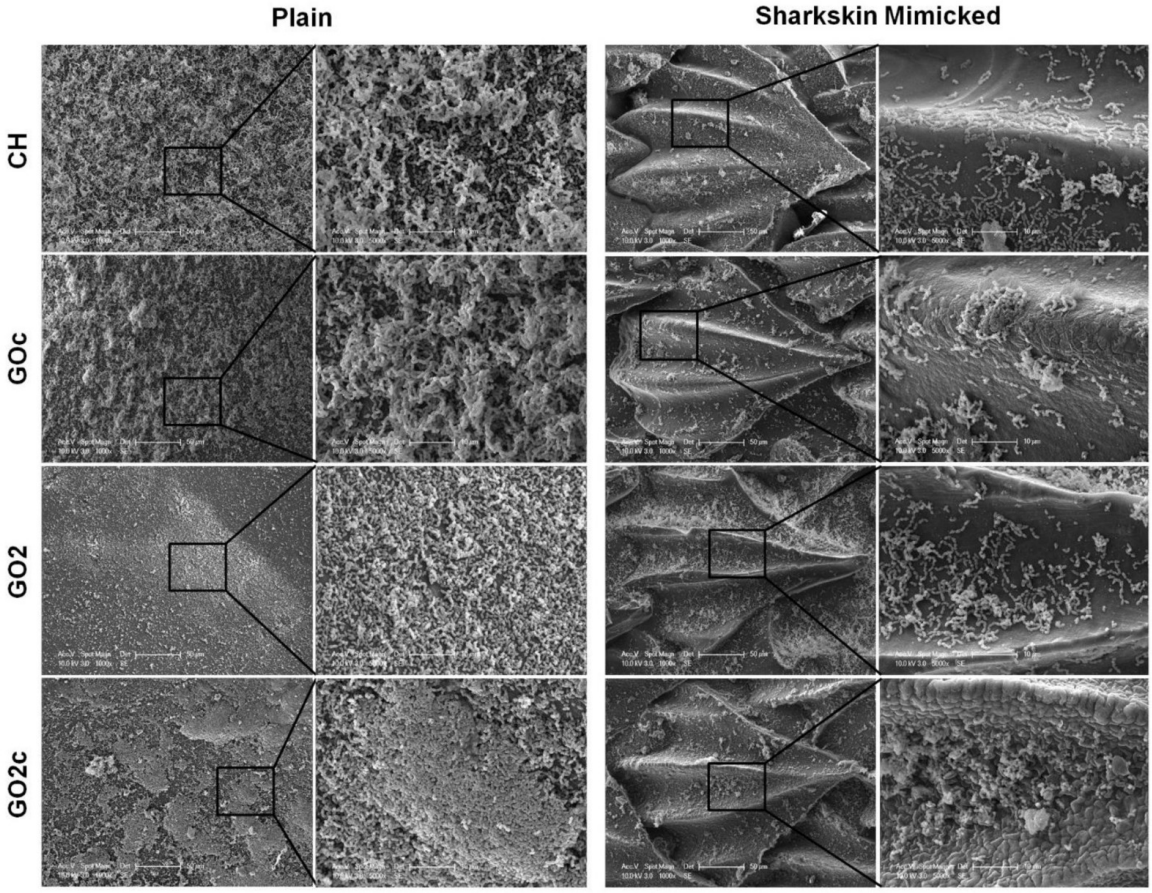


Figure 3.9 SEM images of *E. coli* on membranes. Scale bars: 50μm and 10μm (CH: chitosan, GO2: 0.2 %wt graphene oxide/chitosan nanocomposite, GOc: graphene oxide coated chitosan, GO2c: graphene oxide coated 0.2 %wt graphene oxide/chitosan nanocomposite).

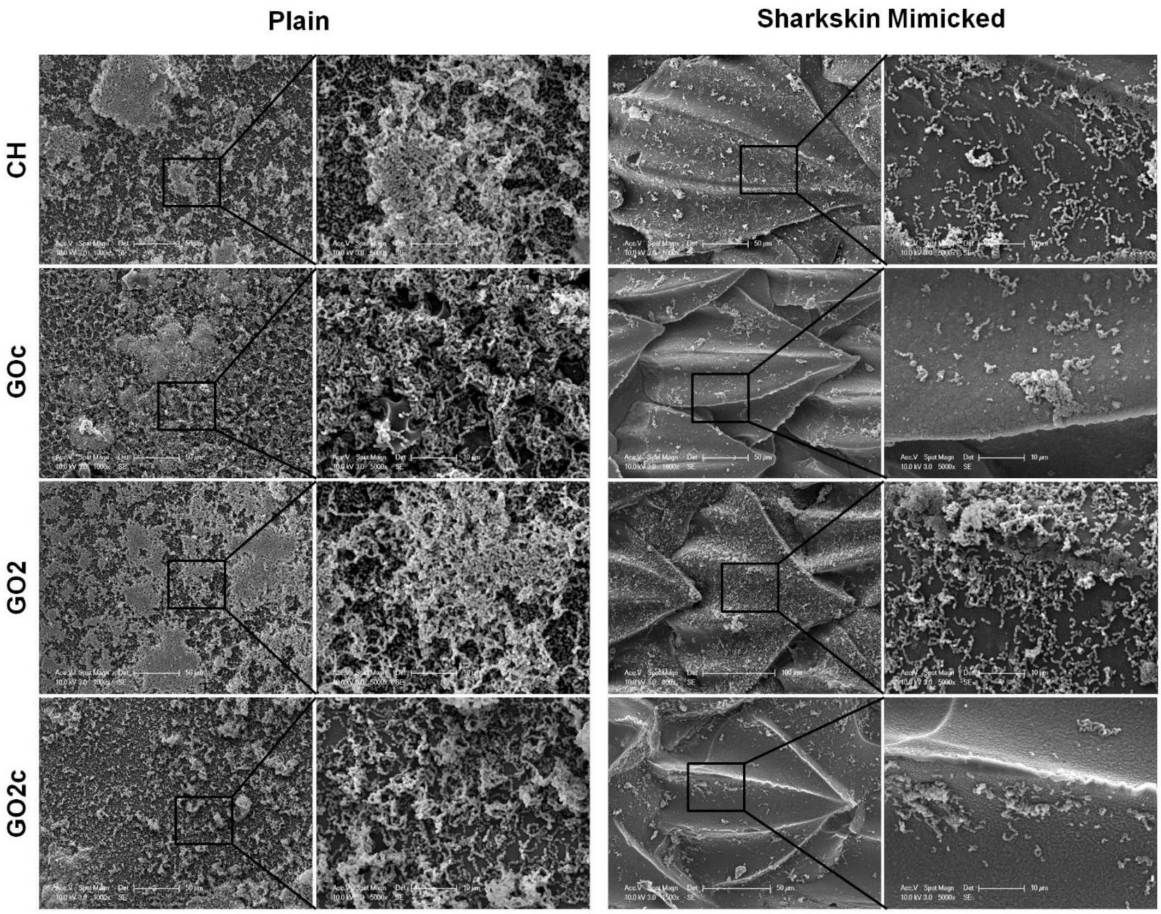


Figure 3.10 SEM images of *S. aureus* on membranes. Scale bars: 50μm and 10μm (CH: chitosan, GO2: 0.2 %wt graphene oxide/chitosan nanocomposite, GOc: graphene oxide coated chitosan, GO2c: graphene oxide coated 0.2 %wt graphene oxide/chitosan nanocomposite).

3.2.4 Mammalian Cell Culture on Sharkskin Mimicked Membranes

After ensuring the superiority of antibacterial activity of sharkskin mimicked to plain membranes, L929 and HaCaT cell lines were cultured on sharkskin mimicked CH, GOc, GO2 and GO2c groups. Seeding density was 1.5x10^4 and on days 1, 3, and 5 MTT and AlamarBlue assays were performed. As shown in Figure 3.11, on day 5 highest values of cellular viability for both L929 and HaCaT belong to GOc membranes. It seems that coating sharkskin mimicked CH membranes with GO increased cell viability of L929 and HaCaT by 1.75 and 2.17-fold, respectively. Similar results for GO/CH composites with higher GO concentrations have been reported by M. Mazaheri *et al.* for viability of human mesenchymal stem cells (hMSCs) [172]. Based on their results,

cell viability is higher in low GO concentrations (1.5% wt).

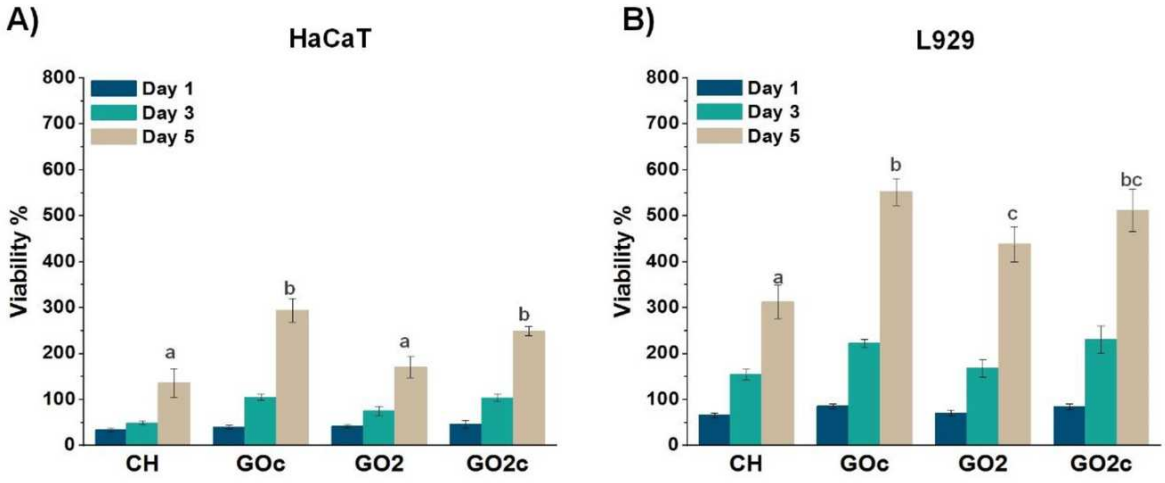


Figure 3.11 HaCaT and L929 cell culture tests results on sharkskin mimicked membranes. **A)** Cell viability of HaCaT on Sharkskin mimicked membranes (MTT assay), **B)** Cell viability of L929 on Sharkskin mimicked membranes (MTT assay) (Mean ± SD, $p<0.05$, n=4; CH: chitosan, GO2: 0.2 %wt graphene oxide/chitosan nanocomposite, GOc: graphene oxide coated chitosan, GO2c: graphene oxide coated 0.2 %wt graphene oxide/chitosan nanocomposite).

AlamarBlue proliferation results (Figure 3.12) confirms the viability results and shows the higher values of cell proliferation in sharkskin mimicked GOc and GO2c groups compared to CH and GO2 groups. Several other studies confirm the prohibitory effect of GO in cell viability as well as proliferation [11],[173]. The promoting effect of GO on cellular viability and proliferation may be attributed to two main factors, i: the large surface area of GO sheets with numerous oxygen containing functional groups provide a highly favorable platform for cell attachment through formation of focal adhesions and ii: the adsorption of serum proteins onto GO sheets due to its numerous surface functional groups, which can be attributed to $\pi - \pi$ stacking, and electrostatic and hydrogen bonding on the surface of GO [150]. Adsorption of serum protein cocktail onto membrane surface provides a familiar and favorable substrate for cells to adhere and spread. The most abundant of these functional groups are epoxy and hydroxyl groups that belong to carboxyl groups located at the edges of GO sheets.

These functional groups make GO a polar material with an overall negative charge which is beneficial in enhancing cellular responses since it has been reported

that polarity plays an important role in cellular functions and promote cell-biomaterial interactions [174],[175].

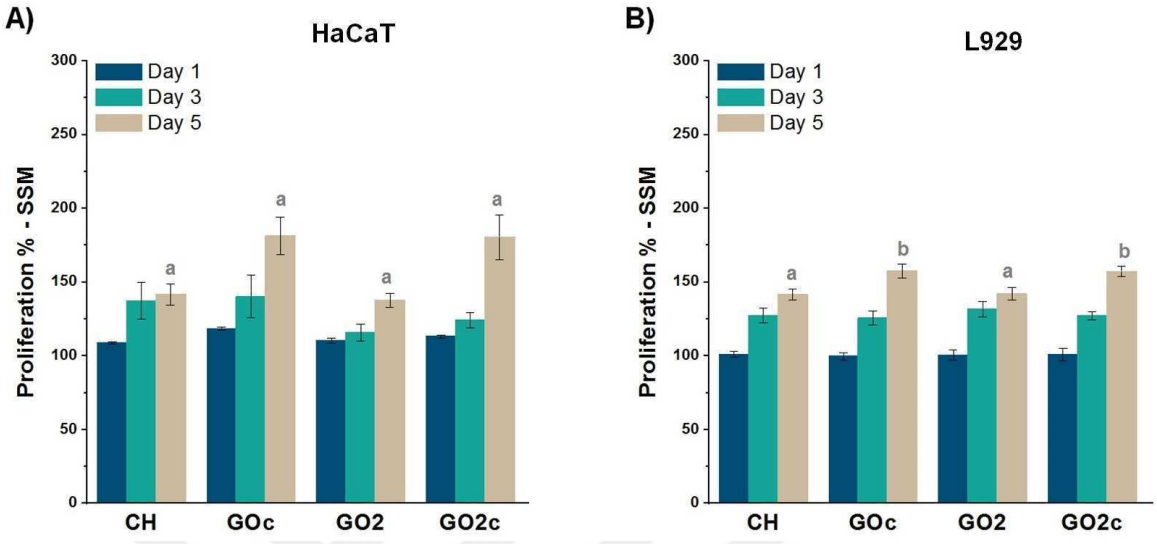


Figure 3.12 Cell culture results of HaCaT and L929 on SSM membranes. **A)** Cell proliferation rate of HaCaT on SSM membranes (AlamarBlue assay), **B)** Cell proliferation rate of L929 on SSM membranes (AlamarBlue assay), (Mean ± SD, $p<0.05$, $n=4$; CH: chitosan, GO2: 0.2 %wt graphene oxide/chitosan nanocomposite, GOc: graphene oxide coated chitosan, GO2c: graphene oxide coated 0.2 %wt graphene oxide/chitosan nanocomposite)

3.2.5 Morphology of Adhered Cells

Cellular morphology is an excellent indicator of healthy cell spreading behavior and metabolic activity status. SEM images of L929 and HaCaT cultured on sharkskin mimicked CH, GOc, GO2, GO2c, and glass (positive control) were obtained on days 1, 3, and 5 (Figures 3.13, 3.14, and 3.15). As shown in Figure 3.15 coated surfaces have remarkably promoted cell adhesion and spreading of both cell lines. On day 5, cell morphology of both cell types on CH group is closer to round shape indicating that cells are experiencing high levels of stress and are less likely to proliferate which is in agreement with MTT and AlamarBlue results. Cells of both types on sharkskin mimicked GOc and GO2c membranes resemble morphology of viable and proliferating cells [like glass (positive control)] since they are well spread and highly populated. It appears that GO incorporated inside CH polymer network also increases cell adhesion and number of viable cells but not as effectively as GO coating. A favorable substrate for cell adhesion

results in well-spread cells. The process of spreading changes the organization of cell cytoskeleton which in turn regulates cellular signals and pathways towards maturation and proliferation. Presented results provide additional proof regarding the boosting effect of GO on cell adhesion, spreading, proliferation and viability and highlight the contact-based nature of GO's effects on model mammalian cells [174],[176],[177].

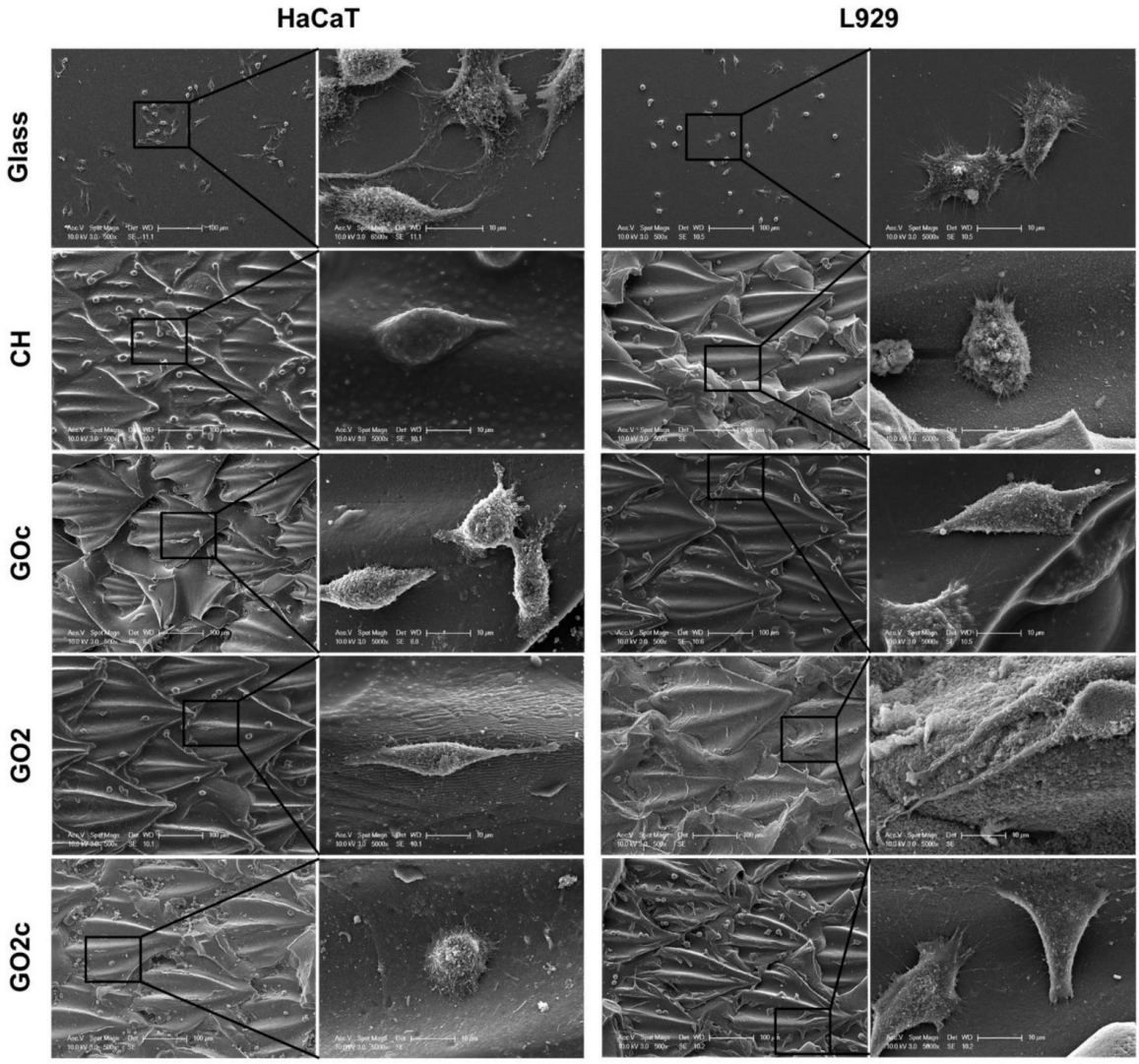


Figure 3.13 SEM images of HaCaT and L929 cultured on sharkskin mimicked membranes 1 day post culture. Scale bars: 100μm and 10μm.

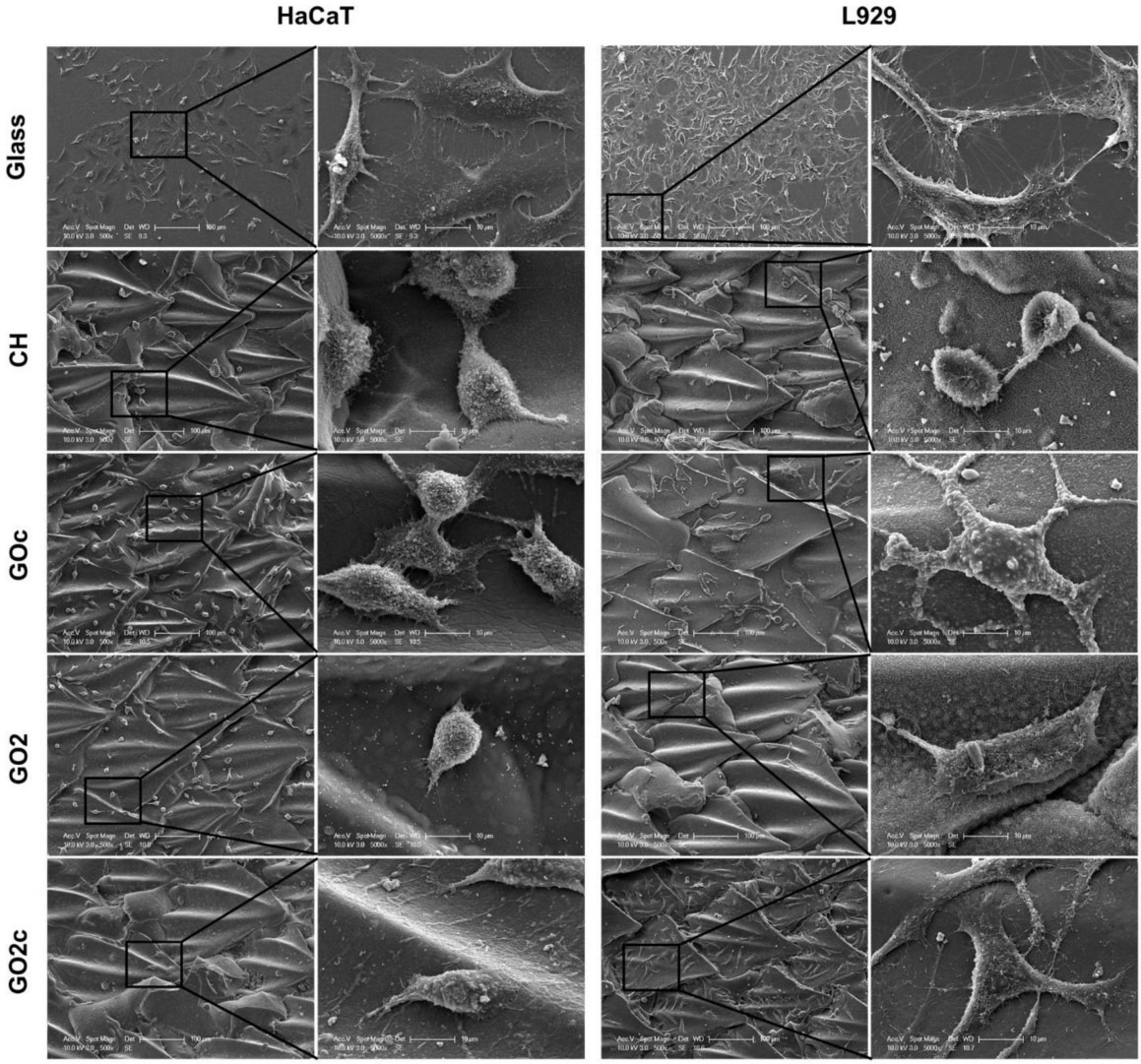


Figure 3.14 SEM images of HaCaT and L929 cultured on sharkskin mimicked membranes 3 days post culture. Scale bars: 100μm and 10μm.

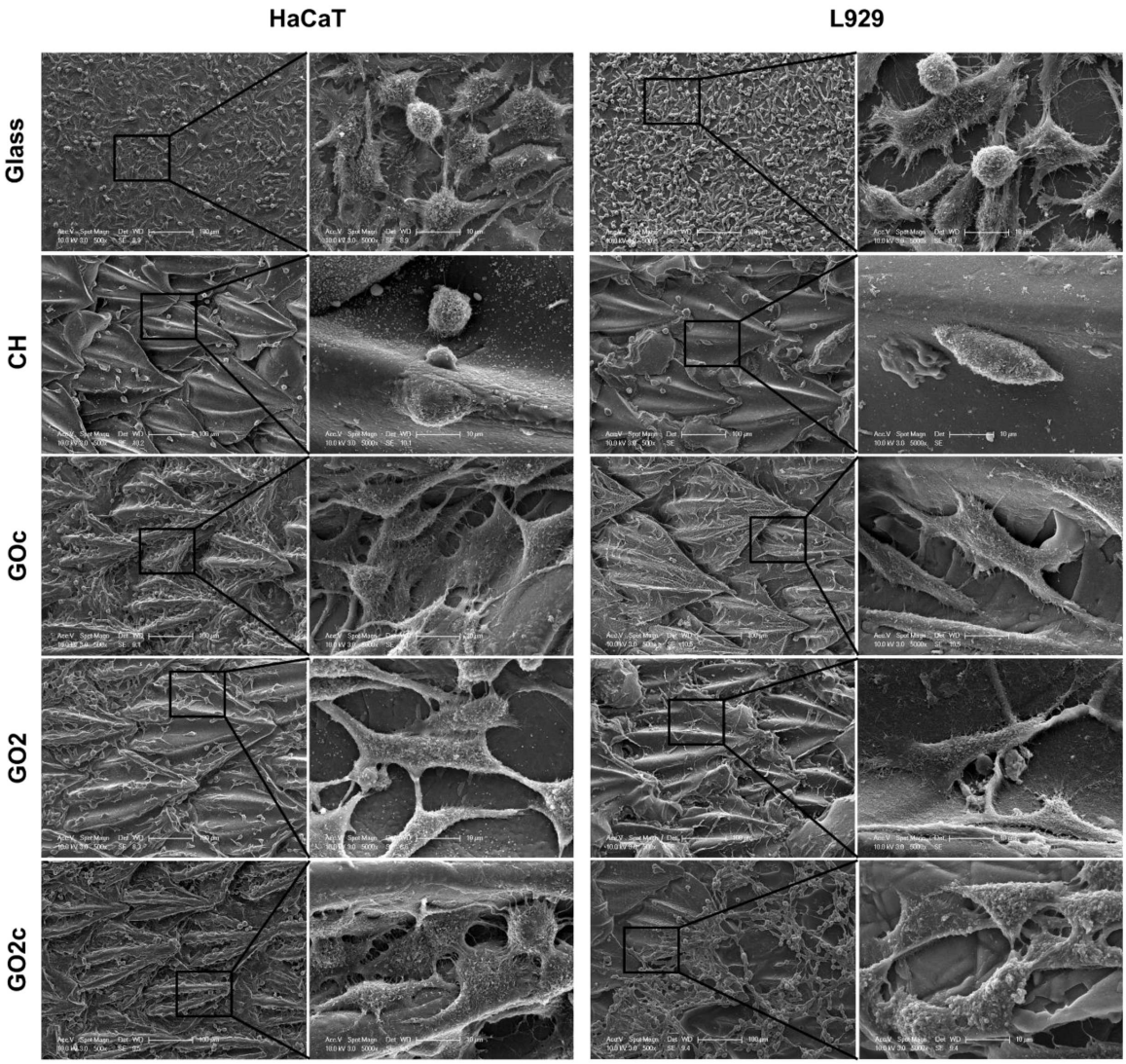


Figure 3.15 SEM images of HaCaT and L929 cultured on sharkskin mimicked membranes 5 days post culture. Scale bars: 100μm and 10μm.

3.3 Discussion

Inspired from nature, the dual antibacterial and cytocompatibility properties of sharkskin microtopography and GO in form of surface coating and nanocomposite were studied with the following objectives: maximum cell adhesion and proliferation, maximum antibacterial properties, and ease of fabrication. To do so, CH-based membranes were fabricated with GO in forms of nanocomposite and surface coating.

Based on the FTIR results, presented in Figure 3.2 it can be said that since the bonding of GO to CH mostly occurs via interactions between ionized -COOH group of GO and protonated -NH_2 group of CH, the abundant of charged groups may increase interactions with water molecules [153]. The effect of surface topography on surface wettability is unprecedentedly unique. In all sharkskin mimicked experimental groups the water contact angle values were significantly greater than that of their corresponding plain membranes. Similar results have been reported by Tae Wan Kim, Zhao *et al.* and Bharat Bhushan for sharkskin bioinspired surfaces [178–180].

Surface properties were further characterized with water contact angle measurements of both plain and sharkskin mimicked membranes which are shown in Figure 3.3. It is evident that GO in form of coating had the highest impact on increasing the surface hydrophobicity. These changes in surface hydrophilichydrophobic properties of the membranes have been in the literature [153]. Maraschin *et al.* reported similar fluctuation in WCA values for GO/CH composites [167]. Presence of GO on CH membranes in the form of surface coating increases the contact angle of water as well, similar to that of GO3. Also, most likely the curvatures of sharkskin topography create a very small gap of air between the liquid and the polymer surface at every single groove. This tiny pocket of air along with the fact that available contact points for a water droplet is less in sharkskin mimicked surface compared to that of plain membrane, keep the shape of the droplet closer to a full circle, hence increasing the water contact angle [178]. Moreover it appears that combined effect of chemistry and surface topography resulted in CH, GO2 and GOc to have WCA values above 90°(hydrophobic) and very close to each other. It can be deduced that the number of

functional groups which can interact with water molecules, such as oxygen-containing groups, increases with addition of GO up to a threshold point (0.3% wt) where surface properties change rather sharply.

As shown in Figure 3.4 the presence of GO on the surface of the membrane increases the cell viability to a great extent. This may be due to π-π bond on GO which has the ability of absorbing adhesion proteins from the serum, leading to formation of a substrate that facilitates cell adhesion and spreading [150],[174]. Moreover, the oxygen containing functional groups of GO are believed to have complementary effects on the cell adhesion and proliferation at low concentration of GO [147],[176]. Overall IF images provide additional confirmation of the MTT assay.

In term of antibacterial properties of GO, it has been reported that the oxidative stress induced on bacterial cell wall via reactive oxygen species (ROS) generation is primarily responsible for GO's antibacterial effect on both strains and the difference between its effect on gram positive vs gram negative strain is probably due to the differences between cell wall structure on the two strains [171]. Despite the considerable reduction in formation of bacterial biofilm on sharkskin mimicked membranes coated with GO, the underlying cause can be either bactericidal effect of GO or topography induced reduction of bacterial biofilm formation or a combination of these. In term of effect of surface topography on biofilm, obtained results are in agreement with reported literature regarding antibacterial effects of sharkskin mimicked and inspired surfaces [125],[181]. Xia Pu *et al.* showed that PDMS based sharkskin mimicked surfaces have remarkable antifouling properties in form of anti-algae adhesion due to substrate's combined hydrophobicity and surface topography characteristics [27],[182]. Furthermore, H. W. Chien *et al.* and Choi *et al.* sharkskin inspired micropatterned surfaces reported that significantly reduce bacterial biofilm formation for both *E. coli* and *S. aureus* strains in dynamic culture conditions [30]. Considering that the drag force reduces considerably on a surface with sharkskin micropattern, reduction of bacterial biofilm growth is probably greatly affected by the constant movement of the bacterial suspension on it. Thus, the true underlying mechanism of antibacterial effect of sharkskin mimicked surface in static (stationary) culture condition was still

unexplained. Our findings show that even in stationary conditions, sharkskin mimicked surfaces can significantly reduce bacterial biofilm formation. So far it seems that sharkskin topography in CH membranes significantly decreases the bacterial biofilm formation of *S. aureus* and *E. coli* formed over 24 h by approximately 50% with or without GO modification. However, the chemical effect of GO, both on the surface and within the polymer network, changes the significance of this effect. It appears that despite the numerous studies conducted on antibacterial potentials of GO, at low concentrations of GO in combination with CH, sharkskin topography can reduce biofilm formation just as effectively, thus debilitating the antibacterial properties of GO both on surface and within the polymer network.

According to the literature, sharkskin mimicked, and inspired surfaces show remarkable antibacterial properties. Bacterial adhesion and biofilm formation is influenced by many factors namely, surface charge, chemistry, topography, and wettability [183]. As the majority of these studies used hydrophobic nondegradable polymers such as PDMS and PMMA for fabrication of the substrates, the combined effect of hydrophobicity and topography are responsible for the obtained results. In addition, it has been reported that surface topography of sharkskin creates a certain amount of surface roughness which disrupts the process of biofilm formation [13]. Moreover, it has also been suggested that the grooved shape of sharkskin creates a very thin pocket of air at the interface of bacterial suspension and the substrate which in turn reduces the available adhesion point for microorganism, hence reducing the number of attached bacteria. While all these might be acceptable, the true mechanism behind the antibacterial properties of sharkskin mimicked surfaces still remains unknown [125]. The present study indirectly evaluates the validity of air pocket speculation being the only effector by using a biodegradable polymer that has a high water uptake capacity, which eliminates the possibility of formation of the air pocket. Thus, it is shown that even by using hydrophilic substrates, the sharkskin microtopography does indeed decreases bacterial biofilm growth rate by significantly reducing the number of adhered bacteria to the surface. Using CH as the base polymer opens up the way for application of sharkskin mimicked biomaterials for implantation purposes.

Apart from topography, the effect of GO on sharkskin effect is evaluated as well. It is widely accepted that antibacterial properties of GO is to be due to the oxidative stress of GO sheets on the bacterial cell wall via ROS production [168],[171]. The highly reactive oxygen containing functional groups on the surface and at the edges of GO sheets can bind to the outer membrane of the bacterium [168],[171]. It has been reported that when GO sheets are introduced to bacterial suspensions in the form of liquid mixture, bacteria usually get wrapped by free floating GO sheets thus losing their mobility [140],[184]. In case of GO sheets are fixated on the surface of the substrate, small sized GO sheets induce an effective oxidative stress to outer cell wall and damage it resulting in leakage of cytoplasm out of the cell, therefore killing it. Both these mechanisms require GO sheets to be in direct contact with the microorganism [38]. When GO is dispersed within the CH polymer network at low concentration, most probably majority of functional groups of GO sheet on both sides interact with active sites of CH, resulting in considerably fewer amount of GO sheets on the outer surface of the membrane. But, when GO is coated on the surface of the polymer, antibacterial activity of GO is most likely to enhance. Our findings align with the proposed mechanism for antibacterial properties of GO regarding induced oxidative stress following contact and reported differences of its activity towards gram negative and gram positive bacteria [171],[185]. Therefore, considering that the amount of necessary GO for fabrication of nanocomposites membranes is far greater than that of coated membranes and the fact that there is no statistically significant difference between antibacterial properties of GOc, GO2 and GO2c groups, GO coating appears to be superior to nanocomposites in term of cost and ease of fabrication process. As for the effect of surface topography, SEM images confirm the ISO 22196 and MTT assay results. It has become obvious that sharkskin mimicked surface indeed has antibacterial properties via reducing bacterial attachment and adhesion.

Examining the cell viability and proliferation rate of HaCaT and L929 on sharkskin mimicked surfaces showed that most probably due to the larger surface area of sharkskin mimicked membranes in micro scale compared to that of plain membranes per unit area (cm_2) there are more adhesion points available for cells to attach and spread. Additionally, as reported in the literature, sharkskin topography creates a cer-

tain level of surface roughness which in this case appears to promote cell adhesion and increase metabolic activity [186],[187]. Thus, combination of sharkskin micropattern and GO has proven to have remarkable effect of model L929 and HaCaT cell viability and proliferation.

In summary, it is concluded that sharkskin topography has indeed remarkable antibacterial properties against both gram-negative *E. coli* and gram-positive *S. aureus* in static conditions even though sharkskin in known to demonstrate this behavior mainly under dynamic flow conditions (swimming). Furthermore, sharkskin microtopography not only does not have cytotoxic effects on L929 and HaCaT mammalian cell lines but also it enhances cell viability and provides more available surface for cell adhesion and spreading. In term of using GO, like reported literature regarding its antibacterial activities against both gram-positive *S. aureus* and gram-negative *E. coli*, the presented study reports no statistically significant reduction in neither bacterial biofilm growth rate nor loss of planktonic viability between GO coated and GO nanocomposites in sharkskin mimicked membranes. However, the mammalian cell results clarify the necessity of GO coating for cell adhesion and proliferation. Finally, considering the ease of GO coating onto CH membranes compared to that of GO/CH nanocomposite along with simplicity of sharkskin micropattern mimicking procedures and abundance and low cost of CH polymer, it is concluded that GOc sharkskin mimicked CH based membrane has remarkable potentials as a convenient biomaterial candidate for numerous biomedical applications such as urinary and respiratory catheters as well as biodegradable, highly biocompatible and antibacterial coating layer for implantable medical devices.

4. BIOMIMETIC SHARKSKIN SURFACES WITH ANTIBACTERIAL, CYTOCOMPATIBILE, AND DRUG DELIVERY PROPERTIES

Fighting with the infection is one of the most challenging and costly burdens of the healthcare system. Several types of antibiotics and antibacterial agents have been designed and used in combating this dilemma. Nevertheless, the overuse of drugs and the difficulties of proper delivery have led to the development of drug-resistance in many species of bacteria which has reduced the efficacy of antibiotics. Furthermore, localized delivery of these drugs can be more effective in eliminating biomaterial surfaceassociated infection compared to systemic administration. This type of infection occurs mostly by the formation of a bacterial biofilm layer on the surface of the implantable biomaterial which is the interface between the biomaterial and the tissue. Sharkskin topography is known for its antibacterial properties due to its unique pattern. Herein, antibacterial properties and drug release potentials of sharkskin mimicked chitosan membranes are investigated with the aim of studying the impact of this topography in reducing bacterial biofilm formation on drug-loaded polymeric membranes. Amp and CAPE loaded CH membranes were fabricated. Gram-positive *S. aureus* bacteria strain is used in antibacterial experiments, and Human primary dermal fibroblast (HDFa) and HaCaT cells were used as model cell lines in cytocompatibility tests.

4.1 Experimental

4.1.1 Materials

Low molecular weight CH (50,000-190,000 Da), L-(+)-Lactic acid (80%), Ampicillin sodium salt, Caffeic Acid Phenethyl Ester, Absolute ethanol, NaOH (anhydrous, pellets), DMSO, Glutaraldehyde (25% in H_2O), and HMDS were purchased from Sigma Aldrich. PDMS (Sylgard 184) was purchased from Dow Chemical.

4.1.2 Preparation of Sharkskin Biomimicked Membranes

The skin of a Basking Shark (*Cetorhinus maximus*), supplied from a local fisherman [17]. The skin was cleaned and chemically fixated prior to use. Then by using molding technique and PDMS at the ratio of 15:1 (silicone elastomer to curing agent), the negative mold of sharkskin was prepared as described in the literature [188],[189] (Figure 4.1).

2.5 %w/v CH solution was prepared in 2.5 %v/v aqueous L-(+)-Lactic acid. The stock solutions of 200 mg/mL Amp in dH_2O and 0.1 M CAPE in absolute ethanol were prepared as well. Amp and CAPE were added to CH solution to obtain final concentrations of 1 mg/mL and 2.5 mg/mL for Amp-containing groups designated as A1 and A2.5, and 200 μM, 500 μM, and 1000 μM for CAPE-containing groups, designated C200, C500, and C1000, respectively [190]. The rest of the experimental groups contained both Amp and CAPE at the aforementioned concentrations in CH solution (Figure 4.1 and Table 4.1). Following the overnight mixing of polymer solutions on a magnetic stirrer, sharkskin mimicked (SSM) and plain samples were prepared via solution casting method [191]. Samples were degassed and dried at 65°C for 36 h, then collected and stored at +4°C for further use [17] (Figure 4.1). Due to the nature of CH and fabrication methods used here, the prepared membranes were in fact hydrogels [192],[193].

Table 4.1
Chemical compositions of experimental groups.

Experimental Groups	A1	A2.5	C200	C500	C1000	A1-C200	A1-C500	A1-C1000	A2.5-C200	A2.5-C500	A2.5-C1000
CH (%w/v)	2.5	2.5	2.5	2.5	2.5	2.5	2.5	2.5	2.5	2.5	2.5
Amp (mg/mL)	1	2.5	-	-	-	1	1	1	2.5	2.5	2.5
CAPE (μM)	-	-	200	500	1000	200	500	1000	200	500	1000

4.1.3 Physicochemical Characterization

Chemical and mechanical characterization were performed on A2.5, C500, and A2.5-C500, all selected at random along with CH as the control group to investigate the

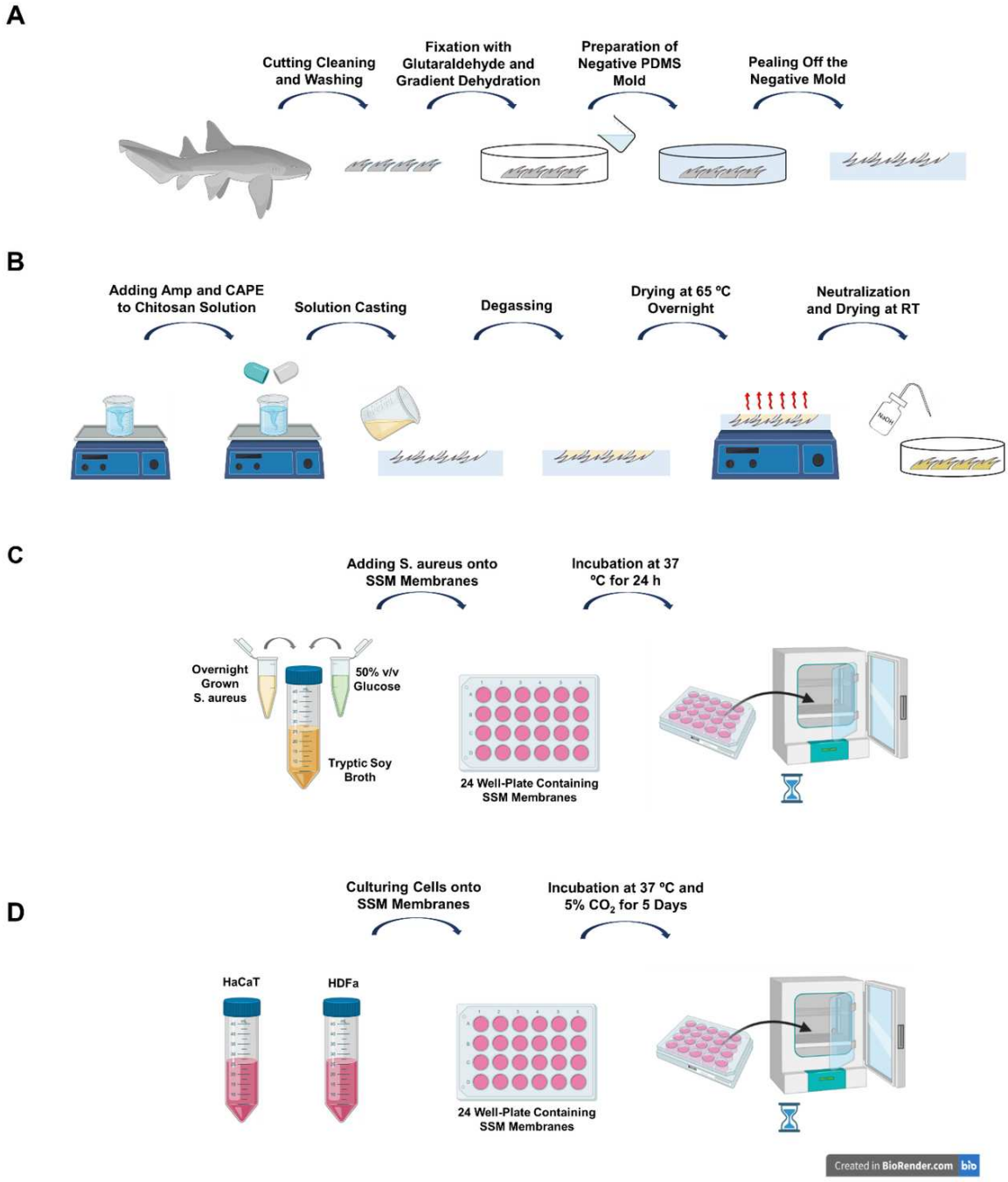


Figure 4.1 Schematic representation of experimental procedures for SSM CH/Amp/CAPE membrane preparation. **A)** Sharkskin mimicked negative mold preparation, **B)** Amp-CAPE loaded CH membrane fabrication, **C)** Bacterial biofilm growth test, and **D)** HaCaT and HDFa cell culture experiments.

effect of Amp and CAPE on surface roughness, chemistry, and mechanical properties. X-Ray Photoelectron Spectroscopy (XPS), FTIR, Tensile Strength, and Atomic Force Microscopy (AFM) were chosen as characterization techniques to provide information regarding chemical interactions between CH and additives, Amp and CAPE.

4.1.3.1 Swelling Ratio. Swelling ratio, which is the capacity of enlargement via water absorption, was measured by immersing dried membranes in PBS at RT for a certain time. Measurements were done at time points between 0, 1, 5, 10, 30, 60 minutes and, 2, 4, 6, and 12 hours. At each time point, excess PBS on each membrane was absorbed by gently pressing both sides of the membrane onto a filter paper followed by immediate weighing [194]. The equation below (Eq. 4.1) was used to calculate the ratio of swelling (Q) [195].

$$\text{Swelling Ratio} = [(W_t - W_0)/W_0] \times 100 \tag{4.1}$$

W_t = sample weight at time point t

W_0 = sample dry weight

4.1.3.2 X-Ray Photoelectron Spectroscopy (XPS). XPS spectra of all groups were obtained using a Thermo Scientific K-Alpha X-Ray Photoelectron Spectrometer (base pressure of 1x10^{-10} Torr). Measurements were taken at an angle of 65° to the analyzer, 165 eV pass energy, and between 1200 and 0 eV [196].

4.1.3.3 FTIR. FTIR spectra of A2.5, C500, A2.5-C500 along with CH membranes were examined using Thermo Scientific Nicolet iS50 FT-IR Spectrometer in the range of 4000 – 400 cm^{-1} to obtain information regarding the intermolecular interactions in composite membrane [151].

4.1.3.4 Tensile Strength. Tensile Strength measurements were done as an indicator of effect of Amp and CAPE on mechanical properties of CH samples. To do this, samples with 5cm x 1cm dimensions were prepared and mechanical tests were done at 0.5mm/s speed with 5kN load using LLOYD Instruments Universal Material Testing Machine (LR Plus Series).

4.1.3.5 Atomic Force Microscopy (AFM). Surface roughness values were measured using Nanosurf Flex Axiom Atomic Form Microscopy (AFM) Device at contact mode via a V-shaped tip 2,000 mm long cantilever with a spring constant of 0.06 Nm^{-1} [197].

4.1.4 Drug Release Rate

Dried samples were weighed prior to immersion in 500 μL of dH_2O for 48 h at 37°C. Samples were then removed and the amount of released Amp and CAPE into dH_2O was measured at 220 nm and 340 nm, respectively using UV-VIS spectrophotometer (NanoDrop^{TM} 2000/2000c Spectrophotometers, Thermo Scientifip^{TM}) [50],[161].

4.1.5 Zone of Inhibition

To understand the mechanism of drug release from the fabricated membranes, the zone of inhibition test was performed. Briefly, circular samples with 5 mm diameter were prepared. Using tryptic soy agar (TSA) plates were prepared. 10^7 CFU of the model bacteria, *S. aureus* (ATCC 25923), in 100 mL of Tryptic Soy Broth (TSB) was spread on the agar plate with a L-spreader. Then both plain and SSM samples were placed on the agar plate. Plates were incubated at 37°C for 24 h and then imaged.

4.1.6 Bacterial Studies

4.1.6.1 Biofilm Growth (MTT Assay). Formation of bacterial biofilm was measured using *S. aureus*. 100 μL of overnight grown suspension (CFU = 10^9) was added into 10 mL TSB medium. The mixture was supplemented with 100 μL of 50% w/v glucose solution to support biofilm formation. 750 μL of prepared bacterial suspension was added onto plain and SSM membranes already placed in wells of 24-well plates followed by incubation in the stationary incubator at 37°C for 24 h. Thereafter, samples were gently immersed in PBS to remove the unattached bacteria. In order to evaluate the viability by measuring the metabolic activity of the bacteria within the biofilm layer, MTT assay was performed with respect to TCP as the positive control group [25].

4.1.6.2 Morphology of Bacterial Adhesion. SEM was used to obtain images of bacteria cultured on plain and SSM membranes in order to morphologically evaluate the effect of surface topography on bacterial adhesion and biofilm layer formation. Samples were incubated for 24h in stationary incubator at 37°C while submerged in 2.5 mL TSB containing 100 μL of the overnight *S. aureus* bacterial suspension in a 15 mL conical tube. Prior to imaging samples were fixated with 2.5% v/v Glutaraldehyde in PBS at RT for 30 min followed by rinsing with PBS twice. Then samples were dehydrated using gradient solution of absolute ethanol in dH_2O ranging from 30% to 95% v/v and finally with 100% ethanol incubated at RT for 15 min on each step. Finally, few drops of HMDS were added onto each membrane and samples were dried overnight at RT. All samples were coated with an approximately 5 nm-thick layers of gold before imaging and images were obtained at 5.00 kV voltage and 15 mm working distance settings using a Philips XL30 ESEMFEG/EDAX instrument [198].

4.1.7 HDFa and HaCaT Cell Culture

Primary Human Dermal Fibroblast and keratinocyte cells were used as model mammalian cell lines. HDFa cell line (ATCC®PCS-201-012™) purchased from American Type Culture Collection organization alongwith its culture medium kit, Fibroblast Growth Kit–Low Serum (ATCC®PCS-201-041) [199]. Cells were grown in this culture medium until passage 6 (P6) was reached and all cell culture experiments of HDFa were performed using P6 cells. Briefly, 0.5 mL rh FGF b, 18.75 mL L-glutamine, 0.5 mL Ascorbic acid, 0.5 mL Hydrocortisone Hemisuccinate, 0.5 mL rh Insulin, and 10.0 mL FBS was added to 480 ml of Fibroblast Basal Medium. As for HaCaT cell line, cells were grown in RPMI-1640 medium supplemented with 10% v/v FBS, 1% v/v L-glutamine (Invitrogen, USA), together with 1% v/v penicillin-streptomycin (Invitrogen, USA) [200]. Passage number 35 (P35) of HaCaT cells was used for all cell culture experiments.

4.1.7.1 Cell Viability (MTT Assay). For the cell viability test, MTT assay was used as a measure of cell metabolic activity [201]. HDFa and HaCaT cells were seeded at 4×10^4 cell densities onto samples placed into the wells of 24-well cell culture plates and incubated at 37°C and 5% CO_2. On days 1, 3, and 5, MTT assay was performed by removing culture media and adding the mixture of MTT stock solution [5 mg/mL of the reagent in sterile PBS (pH=7.2)] [202] and fresh medium at the ratio of 1:10. Plates were transferred to the incubator (37°C, 5% CO_2) and kept there for 2.5 h. Afterwards DMSO was added and gently shaken to dissolve formazan crystal. The optical absorbance of final solutions was measured at 570 nm and 750 nm as measurement and background filters, respectively using Bio-Rad iMark Microplate Reader. Readouts were collected and analyzed with respect to TCP as the positive control group.

4.1.7.2 Cell Proliferation (AlamarBlue Assay). AlamarBlue assay was carried out to investigate the proliferation rate of cells cultures on SSM membranes. To

perform the test, a mixture of 1:10 AlamarBlue reagent to the culture medium was prepared. On days 1, 3, and 5, culture medium was discarded and replaced with the prepared mixture. After 3 h incubation at 37°C and 5% CO_2, supernatants were transferred to 96-well plates for optical absorbance measurement at 570 nm and 595 nm wavelengths as measurement (reduction) and reference (oxidation) filters, respectively. Results were obtained with blank medium as the negative control group [203].

4.1.7.3 HDFa and HaCaT Cell Morphology. To investigate the adhesion and spreading behavior of HDFa and HaCaT cells on SSM samples, SEM images of cells cultured on membranes were captured on days 1, 3, and 5. Prior to imaging samples were fixated and dehydrated according to the protocol mentioned in section 4.1.6.2.

4.1.8 *In vitro* Enzymatic Degradation

Lysozyme-induced enzymatic degradation test was performed for samples used in mammalian cell culture tests. Briefly, samples were dried at 65°C for 48 h prior to the addition of enzyme solution. After measuring the dry-weight of each membrane, 750 μL of freshly prepared 0.8 mg/mL lysozyme enzyme in dH_2O was added to wells of 24-well plates containing dried membranes [129]. Afterwards plates were incubated for 21 days at 37°C. The solution was refreshed every 3 days. Dry weights of all membranes were measured on days 7, 14, and 21, and the degradation rate was calculated based on the equation below (Eq. 4.2):

$$\text{Weight Loss Ratio} = [(W_0 - W_t)/W_0] \tag{4.2}$$

W_t: sample weight on day t

W_0: the initial sample dry weight

4.1.9 Statistical Analysis

All experiments were performed in triplicates with a sample size of n=3 and analyzed data are presented as mean ± SD. Statistical calculations were done using one-way ANOVA followed by Tukey test with a $p < 0.05$ as an indication of statistical significance.

4.2 Results

4.2.1 Chemical and Mechanical Characterization

Chemical characterizations included swelling ratio, XPS, AFM, FTIR, and tensile strength. The swelling ratio test was performed for all experimental groups for 24 h duration. As shown in Figure 4.2, sharkskin microtopography decreased the swelling ratio of all experimental groups regardless of the chemical compositions. In membranes, containing both Amp and CAPE, the highest amount of the swelling belonged to plain A1-C500 and A2.5-C500. This agrees with the swelling ratio of plain CAPE-only samples in which C500 had a higher water uptake ratio than both C200 and C1000. However, this difference was not observed in SSM samples. In addition to the swelling ratio, tensile strength measurements of plain membranes of all chemical compositions were performed [204].

Mechanical properties of the plain membranes were measured. As indicated in Figure 4.3, the presence of Amp and CAPE within the CH polymer matrix changed the tensile strength of plain membranes. Addition of Amp reduced the tensile strength of CH membranes but interestingly increasing Amp concentration from 1 mg/mL to 2.5 mg/mL, increased tensile strength to nearly the same value as CH. On the other hand, the presence of CAPE increased the tensile strength of plain CH membranes in all concentrations (200 μM, 500 μM, and 1000 μM). Combination of 1 mg/mL Amp with all concentrations of CAPE once again decreased tensile strength but there was

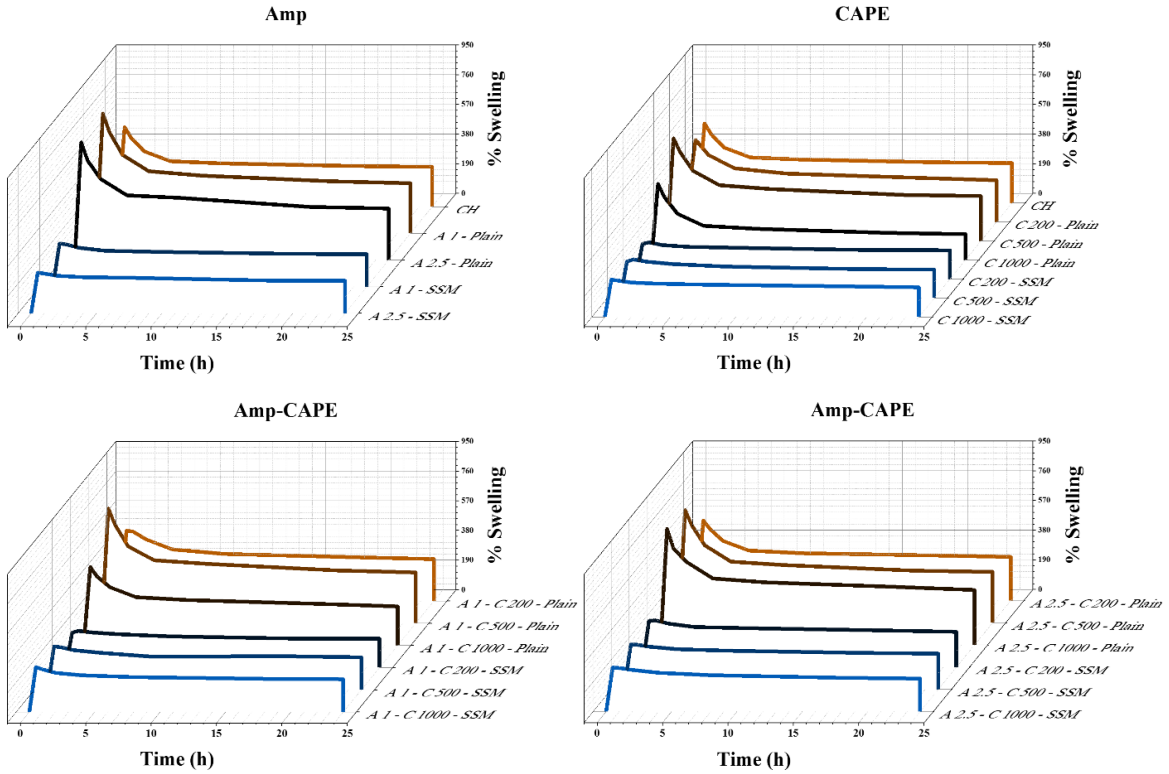


Figure 4.2 Swelling ratio results (SSM: sharkskin mimicked, CH: chitosan, Amp: Ampicillin sodium salt, CAPE: Caffeic acid phenethyl ester, A1: 1 mg/mL Amp, A2.5: 2.5 mg/mL Amp, C200: 200 μM CAPE, C500: 500 μM CAPE, C1000: 1000 μM CAPE, A1-C200: 1 mg/mL Amp + 200 μM CAPE, A1-C500: 1 mg/mL Amp + 500 μM CAPE, A1-C1000: 1 mg/mL Amp + 1000 μM CAPE, A2.5-C200: 2.5 mg/mL Amp + 200 μM CAPE, A2.5-C500: 2.5 mg/mL Amp + 500 μM CAPE, A2.5-C1000: 2.5 mg/mL Amp + 1000 μM CAPE).

no statistically significant difference between them. Similar to Amp-only samples, 2.5 mg/mL Amp content together with CAPE boosted tensile strength values nearly to that of CAPE-only membranes.

Following swelling and mechanical test, incorporation of Amp and CAPE into CH network was confirmed with XPS and FTIR tests. Figures 4.4, 4.5, and 4.6 along with Tables 4.2 and 4.3 represent the obtained results. As seen in XPS survey spectra in Figure 4.4, Sodium (Na) was detected in A2.5 and A2.5-C500 samples which indicated the presence of Amp within the samples since the molecular structure of Amp, $C_{16}H_{18}N_3NaO_4S$, contains Na atoms [205]. Atomic ratio of C/Na also confirmed this as shown in Table 4.2. Addition of CAPE, with the molecular structure of $C_{17}H_{16}O_4$ [130], increased the number of oxygen (O) atoms which was detected by the decrease

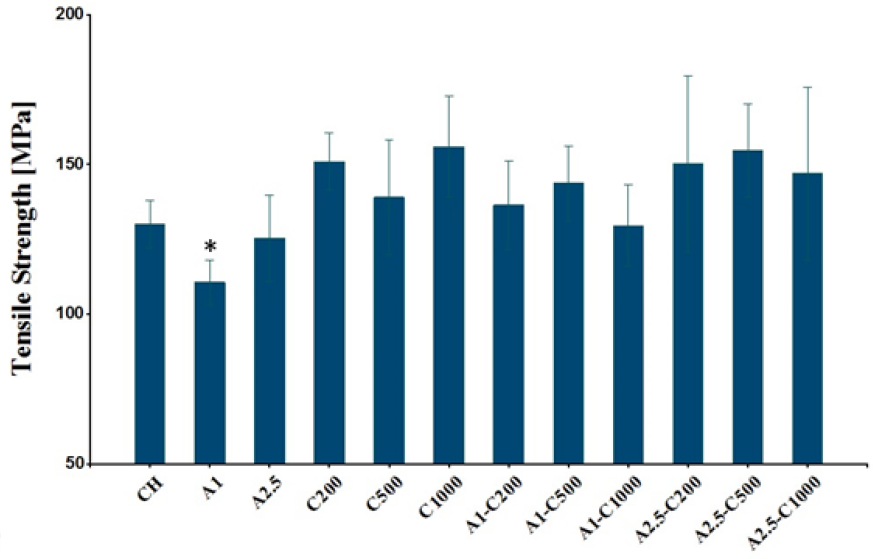


Figure 4.3 Tensile strength results of plain membranes of all chemical compositions (Mean ± SD, *p < 0.05, CH: chitosan, Amp: Ampicillin sodium salt, CAPE: Caffeic acid phenethyl ester, A1: 1 mg/mL Amp, A2.5: 2.5 mg/mL Amp, C200: 200 μM CAPE, C500: 500 μM CAPE, C1000: 1000 μM CAPE, A1-C200: 1 mg/mL Amp + 200 μM CAPE, A1-C500: 1 mg/mL Amp + 500 μM CAPE, A1-C1000: 1 mg/mL Amp + 1000 μM CAPE, A2.5-C200: 2.5 mg/mL Amp + 200 μM CAPE, A2.5-C500: 2.5 mg/mL Amp + 500 μM CAPE, A2.5-C1000: 2.5 mg/mL Amp + 1000 μM CAPE).

in the C/O ratio of CH sample from 5.40 to 2.04 in the C500 sample and confirmed by the higher intensity of O1s peak in the survey spectrum compared to that of CH [$(C_6H_{11}NO_4)$n] [206],[207]. When CAPE and Amp were added to the CH solution together, in theory, the number of both C and O atoms should have increased as well as a slight increase in nitrogen (N) atom content.

Apart from XPS analysis, FTIR spectra of the same samples were obtained and shown in Figure 4.5. The location of the N-H peak in CH was recorded at 3291 cm^{-1} and it shifted to 3391 cm^{-1} in A2.5 and again to 3465 cm^{-1} in A2.5-C500 [208]. Similarly, C=O peak's location of CH was recorded at 1795 cm^{-1} which shifted to 1761 cm^{-1} in A2.5, to 1681 cm^{-1} in C500, and to 1785 cm^{-1} in A2.5-C500. Lastly, peak location of C-O was recorded at 1066 cm^{-1} for CH which shifted to 1172 cm^{-1} in C500 and then again to 1066 cm^{-1} in A2.5-C500 [208],[209]. FTIR data along with XPS results confirm the incorporation of Amp and CAPE into the CH polymer network. The observed slight shifts of the characteristic peaks of CH occurred most probably

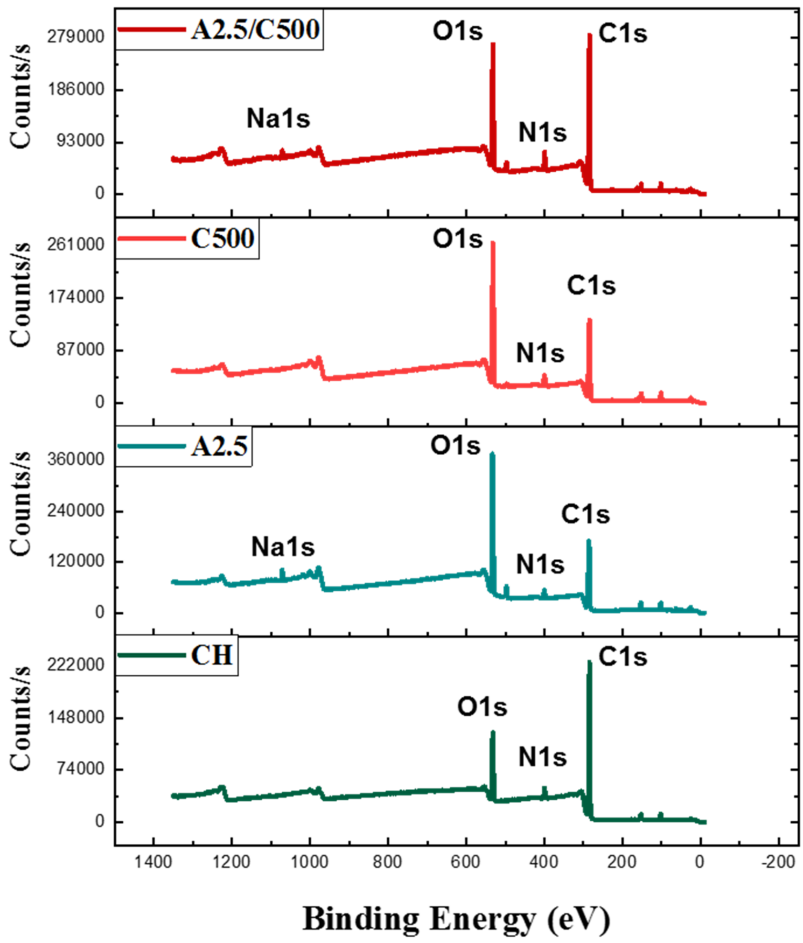


Figure 4.4 XPS survey spectra (SSM: sharkskin mimicked, CH: chitosan, Amp: Ampicillin sodium salt, CAPE: Caffeic acid phenethyl ester, A2.5: 2.5 mg/mL Amp, C500: 500 μM CAPE, A2.5-C500: 2.5 mg/mL Amp + 500 μM CAPE).

due to the presence of Amp and CAPE within the CH polymer chains. These minor changes in position of the peaks and their intensities are most likely an indicator of non-covalent bonds between the additives and the polymer molecules.

Additionally, some peaks have appeared which do not belong to CH namely peaks at 695 cm^{-1} in A2.5 and 689 cm^{-1} in A2.5-C500 groups which belong to Benzene group of Amp. Also, the C=O group which exists in Amp and CAPE results in different peak positions as a result of differences in overall numbers of the groups present in the sample.

Table 4.2
Atomic ratios of CH, A2.5, C500 and A2.5-C500 membrane obtained from XPS analysis.

Atomic Ratios	C/N	C/O	C/Na
A2.5-C500	15.19	3.49	107.50
C500	13.21	2.04	-
A2.5	16.08	1.73	55.11
CH	20.44	5.40	-

Table 4.3
Characteristic FTIR peaks and their corresponding wavenumbers (cm^{-1}).

Peaks	CH	A2.5	C500	A2.5/C500
-OH	-	-	3471	3490
N-H	3291	3391	-	3465
C-H	2921	-	-	2926
C-H	2877	-	-	2868
C=O	17.95	1761	1681	1785
C-C	-	1648	-	1650
C-N	1262	-	-	1268
C-O-C	1153	-	-	1148
C-O	1066	-	1172	1066
Benzene	-	695	-	689

To investigate how Amp and CAPE affected the surface roughness of plain CH, A2.5, C500, and A2.5-C500 membranes AFM measurements were performed. As seen in Figure 4.6, the addition of Amp created small clump-like features on the surface of the membrane. These features increased the surface roughness (Rq) of CH from 31.52 ± 3.415 nm to 47.2 ± 5.925 nm in A2.5. Contrary to the effect of Amp, the presence of CAPE reduced the surface roughness of CH from 31.52 ± 3.415 nm to 9.352 ± 1.578 nm. Combining Amp and CAPE resulted in the surface absolute roughness value very close to that of A2.5 at 47.63 ± 5.912 nm, showing the predominant effect of Amp within the composite. This phenomenon is most probably due to the higher molecular

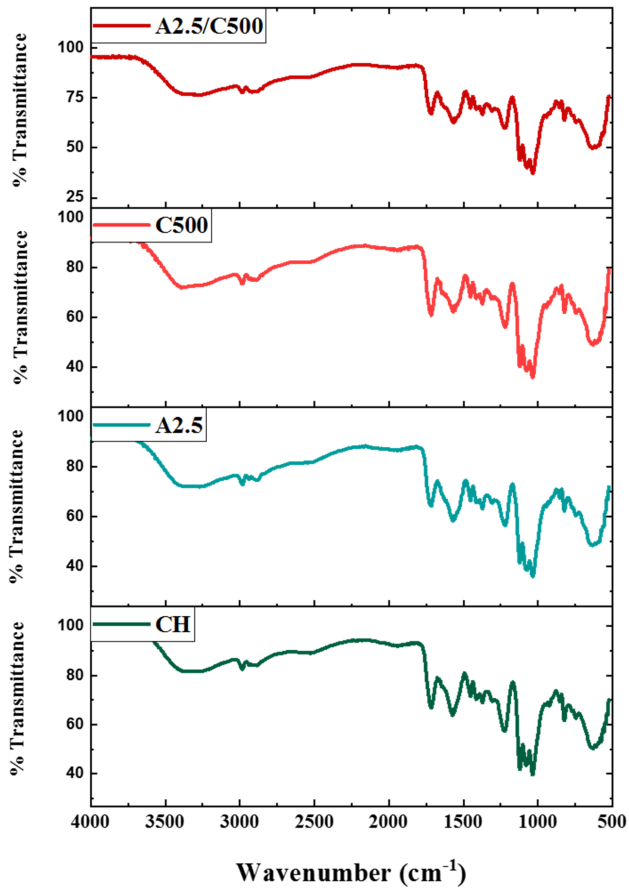


Figure 4.5 FTIR spectra of CH, A 2.5, C500, and A2.5-C500 membranes (CH: chitosan, Amp: Ampicillin sodium salt, CAPE: Caffeic acid phenethyl ester, A2.5: 2.5 mg/mL Amp, C500: 500 μM CAPE, A2.5-C500: 2.5 mg/mL Amp + 500 μM CAPE)

weight and water solubility of Amp ($C_{16}H_{18}N_3NaO_4S$, 371.4 g/mol) compared to CAPE ($C_{17}H_{16}O_4$, 284.31 g/mol) which might have resulted in more homogeneous dispersion of Amp across the membrane surface, inhibiting the effect of CAPE on surface roughness. The Ra values for CH, A2.5, C500, and A2.5-C500 were measured 26.91 ± 3.311 nm, 39.69 ± 6.18 nm, 7.367 ± 1.303 nm, and 40.09 ± 6.202 nm, respectively. The same trend for Rq was reported by K. Divya *et al.* showing increase in surface roughness of CH membranes in composite membranes as a result of additive and varying depending on its concentration [210].

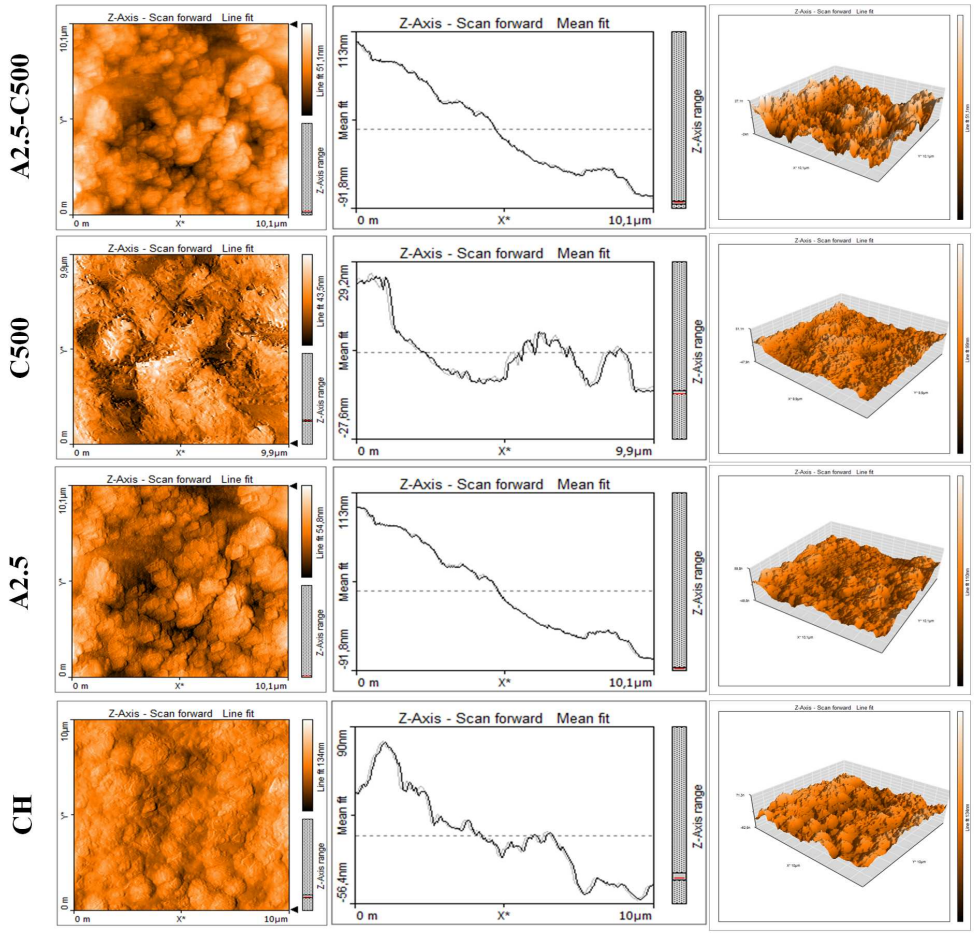


Figure 4.6 AFM results (10 μm x 10 μm scan area) of plain membranes (CH: chitosan, Amp: Ampicillin sodium salt, CAPE: Caffeic acid phenethyl ester, A2.5: 2.5 mg/mL Amp, C500: 500 μM CAPE, A2.5-C500: 2.5 mg/mL Amp + 500 μM CAPE).

4.2.2 Drug Release and Zone of Inhibition

Drug release test was performed to investigate the influence of surface topography on the release of Amp and CAPE from CH polymer network for a period of 24h at 37°C in dH_2O (Figure 4.7 and 4.8). Figure 4.7A, B, and C represent μg Amp released in dH_2O per mg of the sample dry weight. An overall evaluation of this data showed a higher drug release for plain membranes compared to SSM membranes. Even though the surface area of SSM sample is more than that of plain samples due to the riblets and grooves of sharkskin microtopography [211], the amount of released drug is noticeably less in SSM membranes compared to plain membranes in most groups. It

is most likely that due to the noticeably low swelling ratio of SSM samples compared to that of their plain counterparts, release rates have decreased as well.

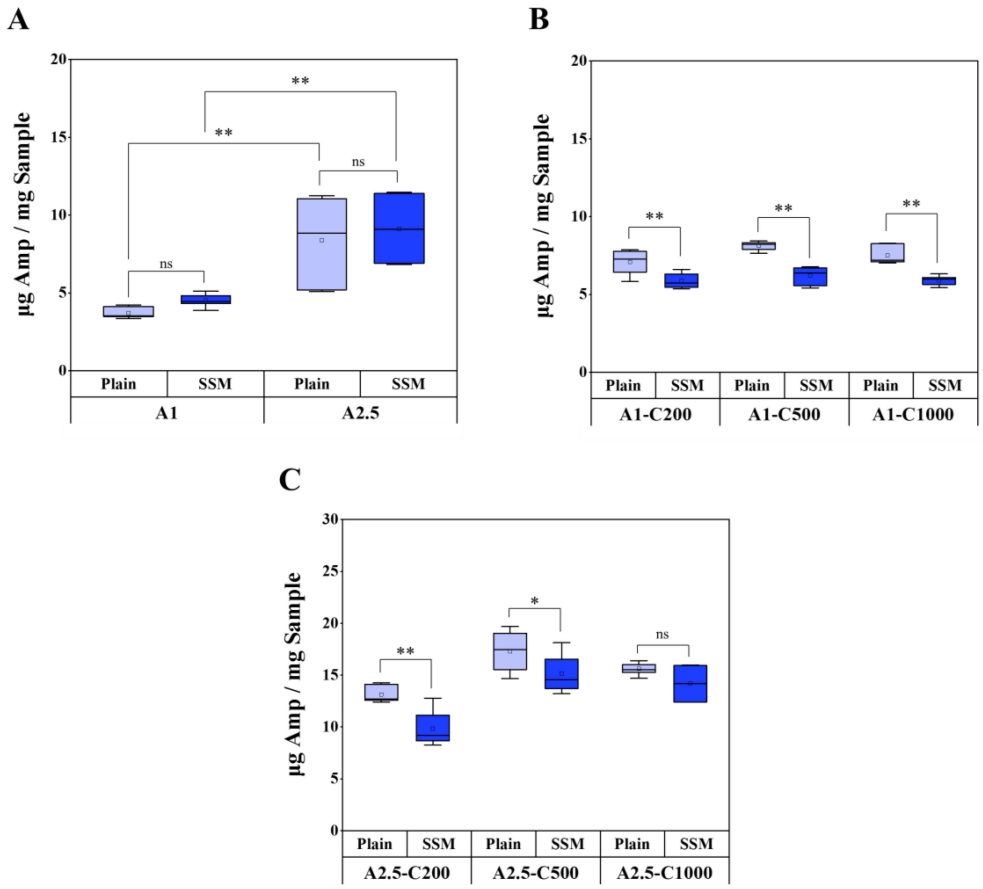


Figure 4.7 Drug release results of Amp (μg Amp per mg sample) after 24 h incubation in dH_2O at 37°C); **A)** Amp-only groups, **B)** A1-CAPE groups, **C)** A2.5-CAPE groups (Mean ± SD, *p< 0.05, **p< 0.001, SSM: sharkskin mimicked, Amp: Ampicillin sodium salt, CAPE: Caffeic acid phenethyl ester, A1: 1 mg/mL Amp, A2.5: 2.5 mg/mL Amp, A1-C200: 1 mg/mL Amp + 200 μM CAPE, A1-C500: 1 mg/mL Amp + 500 μM CAPE, A1-C1000: 1 mg/mL Amp + 1000 μM CAPE, A2.5-C200: 2.5 mg/mL Amp + 200 μM CAPE, A2.5-C500: 2.5 mg/mL Amp + 500 μM CAPE, A2.5-C1000: 2.5 mg/mL Amp + 1000 μM CAPE).

Detailed examination of the A1 release rate revealed that there was very little and statistically insignificant difference between the amounts of Amp released from the plain and SSM samples (Figure 4.7A). This indicated that the larger surface area of SSM samples [211] and the higher swelling of plain A1 most probably have cancelled out each other's effect and overall did not affect the transfer of Amp molecule to dH_2O over the 24 h incubation. As for A2.5, it seems that the effect of swelling ratio overcame the difference of surface area and resulted in higher Amp release in plain membranes

even though this difference was not statistically significant either (Figure 4.7A). As for the significant release of Amp from SSM A2.5 compared to SSM A1, most likely the concentration gradient between Amp and dH_2O overcame the inhibitory effect of low swelling ratio SSM A2.5 and resulted in a high rate of Amp release.

After the addition of CAPE to A1 groups, the release rate of Amp increased for both plain and SSM groups although it was more subtle for SSM (Figure 4.7B). Despite this noticeable boost, there was still no statistically significant difference between released Amp amounts from plain A1-C200, A1-C500, and A1-C1000 groups. Similar insignificance was also observed for SSM A1-C200, A1-C500, and A1-C1000 groups. A close look into A2.5 and its combination groups with CAPE in Figure 4.7C revealed that SSM A2.5-C200 has a release value of 9.8 μg Amp per mg sample which is very close to that of A2.5 at 9.1 μg Amp per mg sample, indicating that C200 did not have a noticeable effect on Amp release.

CAPE release in dH_2O over the period of 24 h at 37°C is presented in Figures 4.8. As seen in the Figure 4.8A, the amount of CAPE released from plain C200 membrane was very close to SSM C200 sample. By increasing CAPE content by 2.5 and 5 times, the release from SSM increased as well but not relative to the CAPE content. Interestingly sharkskin microtopography increased CAPE release compared to that of plain membranes.

It appeared that the larger surface area of SSM samples might have affected CAPE release. Addition of 1 mg/mL Amp to CAPE affected CAPE release behavior of all groups containing both Amp and CAPE in the manner of reversing the effect of topography on CAPE release (Figure 4.8B). It appears that the addition of 1mg/mL Amp change the release rate of CAPE from plain CH membranes compared to SSM CH. Increasing the Amp content to 2.5 mg/mL induced a statistically significant impact on raising CAPE release from plain A2.5-C200 compared to that of plain A2.5-C500, and plain A2.5-C1000 (Figure 4.8C). Similarly, SSM A2.5-C1000 release was measured at very similar level SSM C1000 groups and statistically significantly different than SSM A2.5-C200 and SSM A2.5-C500. Presence of 2.5 mg/mL Amp within the polymer

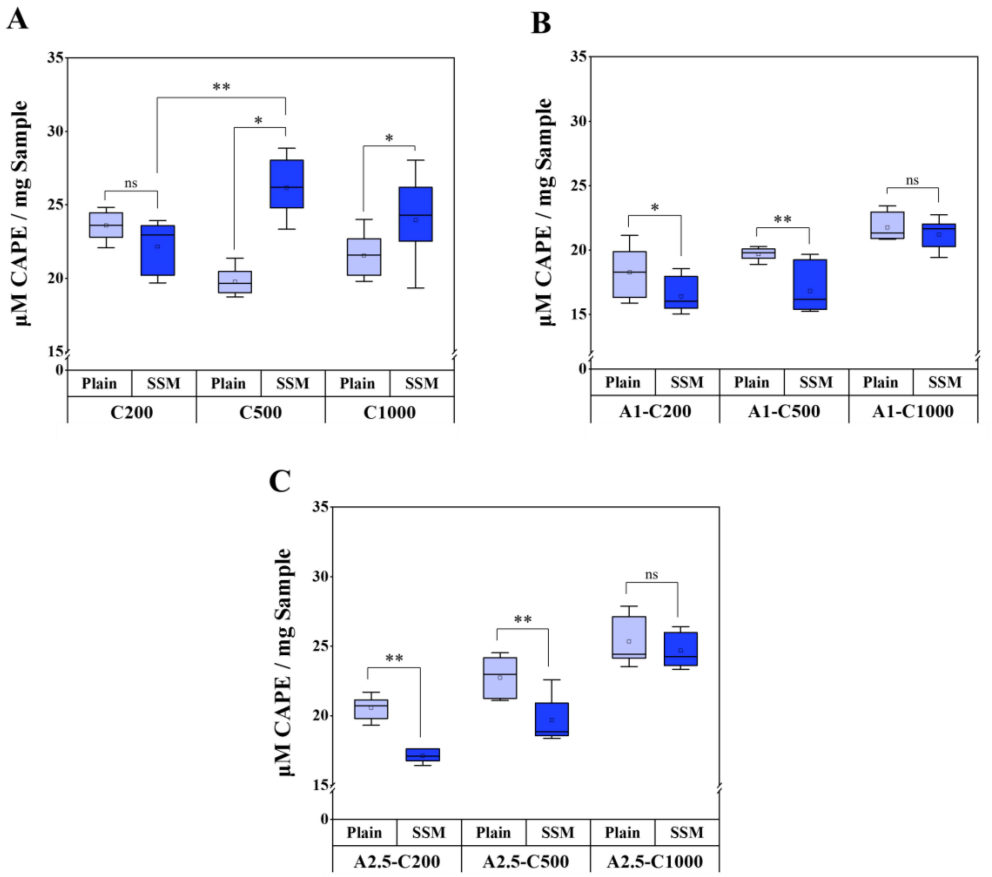


Figure 4.8 Drug release of CAPE (μM CAPE per mg sample) after 24 h incubation in dH_2O at 37°C); **A)** CAPE-only groups, **B)** A1-CAPE groups, **C)** A2.5-CAPE groups (Mean ± SD, *p < 0.05, **p < 0.001, SSM: sharkskin mimicked, Amp: Ampicillin sodium salt, CAPE: Caffeic acid phenethyl ester, C200: 200 μM CAPE, C500: 500 μM CAPE, C1000: 1000 μM CAPE, A1-C200: 1 mg/mL Amp + 200 μM CAPE, A1-C500: 1 mg/mL Amp + 500 μM CAPE, A1-C1000: 1 mg/mL Amp + 1000 μM CAPE, A2.5-C200: 2.5 mg/mL Amp + 200 μM CAPE, A2.5-C500: 2.5 mg/mL Amp + 500 μM CAPE, A2.5-C1000: 2.5 mg/mL Amp + 1000 μM CAPE).

seems to have boosted the CAPE release to its certain maximum level for all A2.5-C200, A2.5-C500, and A2.5-C1000 groups.

Based on the data given in Figure 4.2 regarding the swelling ratio of the membranes and their correlation with the data obtained for drug release (Figure 4.7 and 4.8), it has been concluded that the mechanism of drug release is mainly regulated by the transfer of drug molecules from the membrane to the medium during swelling of the membranes (swelling-associated diffusion). Moreover, the concentration gradient of the drug plays a vital role in drug release as well.

To further confirm this conclusion, a zone of inhibition test was performed, and results are shown below. Based on the lack of a measurable zone of inhibition around the plain and SSM samples, as seen in Figure 4.9, it was found that the release of either drugs did not occur via diffusion. As a result, it is concluded that the swelling ratio is the key property controlling the rate of drug release from the fabricated hydrogel membranes.

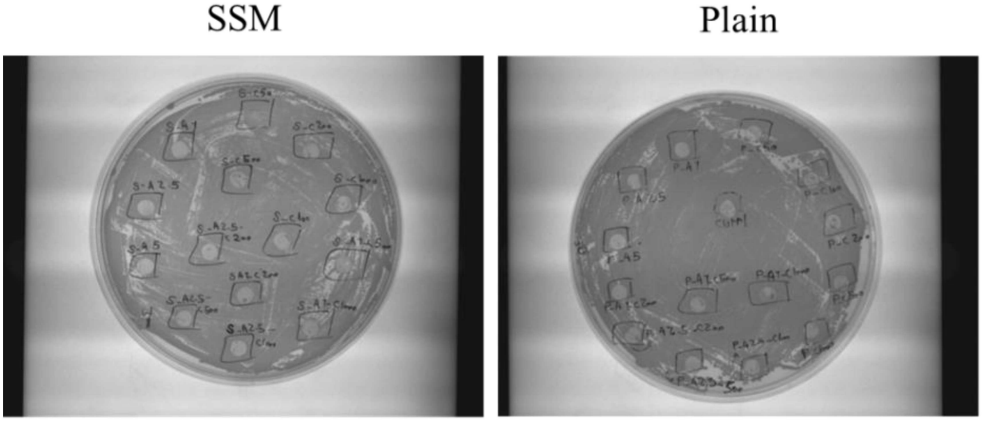


Figure 4.9 Zone of inhibition of plain and SSM samples against *S. aureus* bacteria on TSA plate after 24 h incubation at 37°C.

It can be summarized from release data presented in Figure 4.7 and 4.8 that CAPE had in fact been released into dH_2O during a 24 h period up to a certain level regardless of total content, which is probably due to the very low solubility of CAPE in dH_2O. Furthermore, simultaneous loading of Amp and CAPE within the CH polymer changed Amp release rate and increased it transfer rate from the membrane into the dH_2O.

4.2.3 Bacterial Biofilm Growth (MTT assay) and Morphology

Coagulase negative staphylococci, typically *Staphylococcus aureus* is the most common organism isolated from infected medical devices. Staphylococcus aureus is slightly less common yet more virulent [212]. Thus, elimination and/or prevention of bacterial biofilm formation on the surface is one of the major issues of biomate-

rials, hence testing the formation rate of biofilm and its viability is of great importance [2],[16]. Figure 4.5 represents MTT assay results of *S. aureus* biofilm layer formed over 24 h on plain and SSM membranes. As expected, bacterial biofilm formation was reduced as a result of the presence of the antibacterial agent, Amp, and the cytotoxic compound, CAPE, within the polymeric membranes. This reduction was additional to the significant influence of sharkskin microtopography in disrupting the uniformity of the biofilm layer, hence decreasing the biofilm growth rate. At the first glance it was obvious that SSM membranes had noticeably less biofilm formation values than their chemically similar plain membranes regardless of the amount of additives within the polymer, emphasizing the remarkable effect of sharkskin topography on reducing bacterial biofilm formation in static (stationary) culture conditions [17],[28]. The difference between biofilm layer formation of *S. aureus* on plain and SSM with the same chemical composition are statistically significant in CH, A1, A2.5, C500, C1000, A2.5-C500, and A2.5-C1000. Considering IC50 value [213] as the measure of effective reduction of bacterial biofilm formation in plain and SSM membranes, with respect to plain CH as the control, it becomes clear that sharkskin micropatterned A2.5, C1000, A1-C500, A1-C1000, A2.5-C500, and A2.5-C1000 membranes are the only groups that have the acceptable bacterial biofilm formation rates of 32.5%, 39.0%, 47.9%, 50.8%, 34.6% and 41.7%, normalized with respect to the positive control (TCP), that satisfy the IC50 threshold. This indicated two main points: first, the extraordinary effect of sharkskin microtopography in reducing bacterial biofilm formation on CH based membranes, second, the optimum concentration of Amp and CAPE necessary for inducing a 50% reduction in bacterial biofilm in addition to the sharkskin micropattern effect. Figure 4.10 also shows the influences of different concentrations of Amp and CAPE in the biofilm formation inhibition process. It was evident that biofilm formation on A2.5 is less than that of A1, which was expected since the amount of antibiotic in A2.5 is 1.5 times more than the antibiotic amount in A1 (Figure 4.10A). The bacterial biofilm in plain A1 membrane had a value of 82.2% whereas plain A2.5 membrane had a value of 71.1%. Similarly, SSM A1 membrane scored 51.5% in bacterial biofilm formation whereas SSM A2.5 membrane scored 32.5%. The difference between plain A1 and A2.5 was calculated at the average value of 11.1% while the same difference for SSM A1 and A2.5 was 19%.

As for CAPE, despite C200, C500, and C1000 having CAPE concentrations of 200 μM, 500 μM, and 1000 μM, there is no statistically significant difference between biofilm formations of *S. aureus* on plain membranes with different CAPE concentrations (Figure 4.10B). The same trend was observed between SSM C200, C500, and C1000 groups. This meant that regardless of surface topography, the release of CAPE did not significantly change relative to CAPE concentration within the membrane. This is most probably due to the low solubility of CAPE in aqueous solutions.

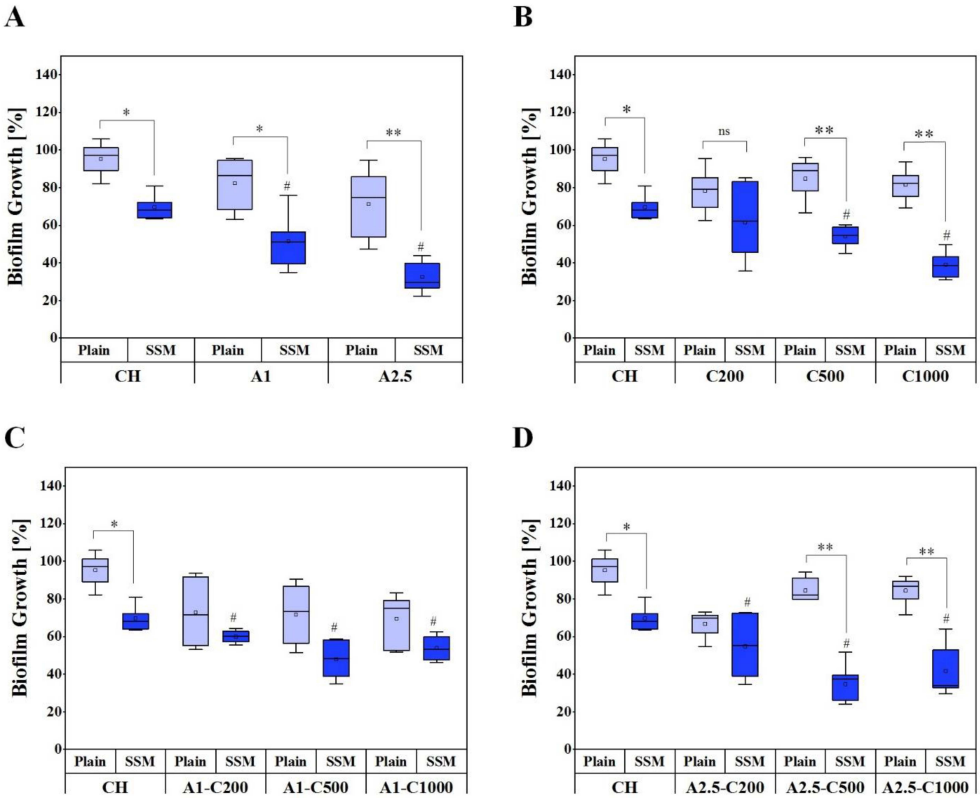


Figure 4.10 Bacterial biofilm growth of *S. aureus* in TSB over 24 h (MTT assay). **A)**Amp-only SSM and plain membrane, **B)** CAPE-only SSM and plain membrane, **C)** A1-CAPE SSM and plain membrane, **D)** A2.5-CAPE SSM and plain membrane (Mean ± SD, *p $<$ 0.05, **p $<$ 0.001, $^{\#}$p $<$ 0.001 compared to the control group, plain CH, SSM: sharkskin mimicked, Amp: Ampicillin sodium salt, CAPE: Caffeic acid phenethyl ester, CH: chitosan, A1: 1 mg/mL Amp, A2.5: 2.5 mg/mL Amp, C200: 200 μM CAPE, C500: 500 μM CAPE, C1000: 1000 μM CAPE, A1-C200: 1 mg/mL Amp + 200 μM CAPE, A1-C500: 1 mg/mL Amp + 500 μM CAPE, A1-C1000: 1 mg/mL Amp + 1000 μM CAPE, A2.5-C200: 2.5 mg/mL Amp + 200 μM CAPE, A2.5-C500: 2.5 mg/mL Amp + 500 μM CAPE, A2.5-C1000: 2.5 mg/mL Amp + 1000 μM CAPE).

Nevertheless, the combination of CAPE at 1000 μM concentration with sharkskin microtopography resulted in more than 50% reduction of bacterial biofilm formation, hence satisfying the IC50 threshold.Apparently, the antibacterial effect of

CAPE was affected and enhanced by the sharkskin topography. In the present thesis, high number of initial bacterial load was used for biofilm test where the constructed SSM membranes were in contact with higher number of pathogens during initial adhesion of bacteria. However,in clinical scenario the initial bacterial number that could lead to biofilm formation and subsequent infection is less than that of the *in vitro* test [30],[214],[215]. Thus, more efficient effect on prevention of biofilm formation by constructed SSM membrane could be expected in a clinical application.

The efficacy of simultaneous release of Amp and CAPE from CH membranes and its impact on bacterial biofilm formation was tested via MTT assay as well. Dual addition of Amp and CAPE within CH solution was done at the following concentrations: A1-C200, A1-C500, A1-C1000, A2.5-C200, A2.5-C500, and A2.5-C1000 in which A1 designated CH solutions containing 1 mg/mL Amp, and A2.5 groups contained 2.5 mg/mL Amp.

Since Amp is an antibiotic and CAPE has high cytotoxic effects, it was expected that the reduction of bacterial biofilm formation to be more than that of CAPE-only and Amp-only membranes for both plain and SSM. Contrary to expectations, A1 combination groups (A1-C200, A1-C500, and A1-C1000) of SSM showed MTT biofilm values close to that of SSM A1, and SSM A2.5 combinations (A2.5-C200, A2.5-C500, and A2.5-C1000) had similar values to that of SSM A2.5 as well (Figures 4.10C and D). It seems that even by combining two cytotoxic agents; bacterial biofilm formation could not be reduced any further. So far, it could be concluded that A1-C500, A2.5-C500 along with A2.5-C1000 had the lowest bacterial biofilm formation rates in addition to C1000-only and A2.5-only groups.

After analyzing MTT assay results for *S. aureus* biofilm along with Amp and CAPE release, SEM images of *S. aureus* on plain and SSM samples of all chemical compositions were acquired to evaluate the morphology of bacterial biofilm layer formed on prepared membranes.

As seen in Figure 4.11, there is a clear difference between plain CH and SSM CH

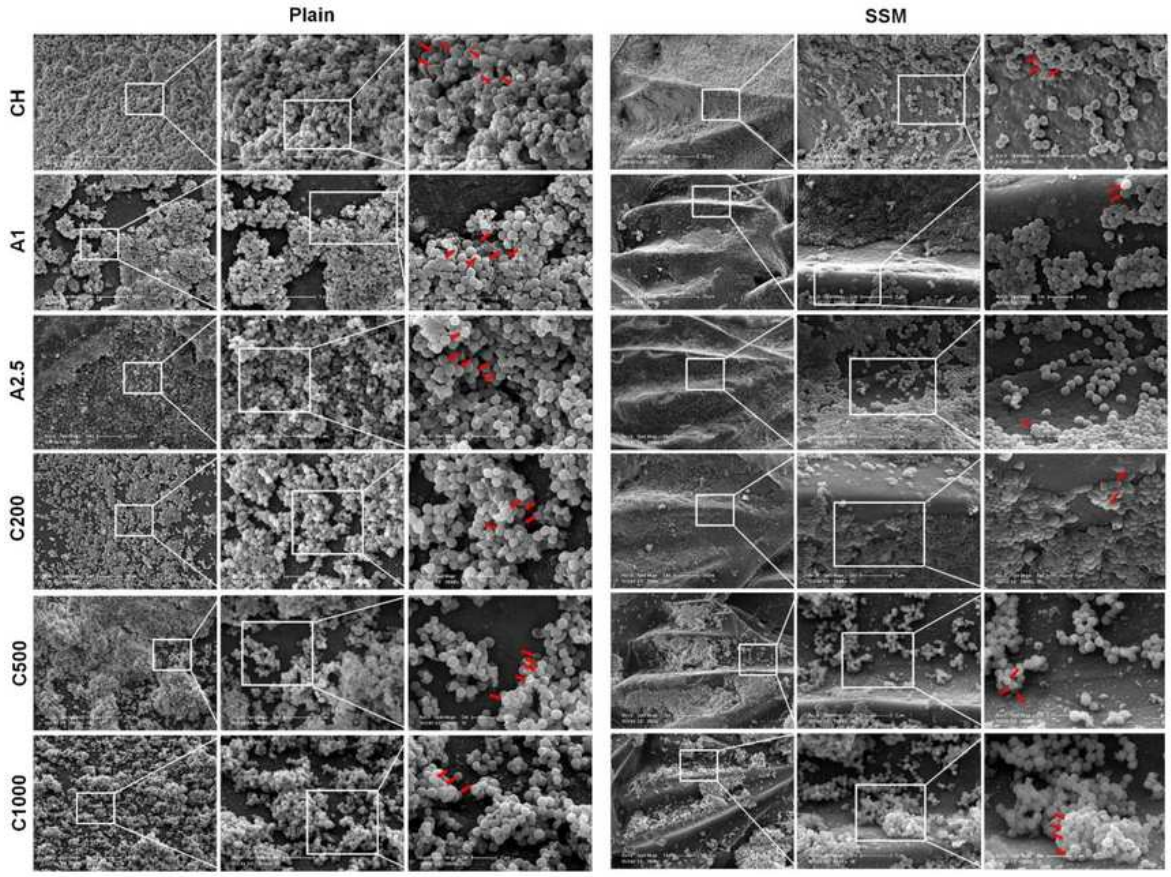


Figure 4.11 SEM images of *S. aureus* growth on plain and SSM CH membranes after 24 h incubation at 37°C. Red arrows indicate layers of bacteria on the surface of the membranes. Scale bars: 20 μm, 5 μm, and 2 μm (SSM: sharkskin mimicked, Amp: Ampicillin sodium salt, CAPE: Caffeic acid phenethyl ester, CH: Chitosan, A1: 1 mg/mL Amp, A2.5: 2.5 mg/mL Amp, C200: 200 μM CAPE, C500: 500 μM CAPE, C1000: 1000 μM CAPE).

membrane in terms of biofilm uniformity. Evidently, grooves and riblets of sharkskin microtopography disrupt this uniformity resulting in lower bacterial biofilm formation in MTT assay. Furthermore, the layered structure of the biofilm on plain membranes appeared to be a multilayered bulk of planktonic bacterium held together in the shape of a wide and thick sheet whereas in SSM the biofilm seemed like colonies of bacteria with approximately 1-5 layers, scattered all over the membrane surface. In the A1 plain membrane, a disruption in the uniformity of the thick biofilm layer was observed which most likely occurred due to Amp release. Bacterial biofilm formed on SSM A1 seemed more scattered compared to the SSM CH due to the antibacterial activity of the Amp. The layer of biofilm on SSM A1 had approximately 1-3 layers of bacteria in form of a relatively homogenous sheet with larger bacteria-free zones compared to SSM CH membrane. For A2.5 plain and SSM samples, a bacterial accumulation pattern and biofilm formation behavior similar to A1 membranes was observed. Although, the biofilm layer on SSM A2.5 had much less sheet uniformity compared to SSM A1 consisting of approximately 1-2 layers of the planktonic bacterium with a higher number of gaps. In the case of CAPE, there was no noticeable difference between plain C200, C500, and C1000 groups regarding bacterial biofilm layer uniformity. All three had scattered clumps of multilayered bacterial colonies. Regarding uniformity of biofilm layer on SSM C200, C500, and C1000, by increasing CAPE concentration, the morphology of the biofilm layer went from being very similar to SSM CH in C200, a relatively multilayered sheet with few gaps, to scattered clumps in C500 with some bacteria-free zones and fewer bacterial clump-like colonies and more free zones in C1000.

As for bacterial biofilm morphology on membranes containing Amp and CAPE together, as shown in Figure 4.12 in all plain membrane groups, the bacterial biofilm layer resembled a very thick and tightly packed multilayer bacterial sheet. By increasing CAPE concentration, some gaps appeared on this layer though not large enough to be considered significantly different. In SSM samples, A1-C200 and A2.5-C200 samples had very similar biofilm layer morphology to their Amp-only counterparts. Evidently, 200 μM CAPE concentration was not enough to induce additional change to the adhesion and formation behavior of the biofilm layer. On plain A1-C500 a few small gaps appeared because of increased CAPE concentration but the biofilm morphology of *S.*

aureus on SSM membranes still looked a lot like SSM A1 membrane. Increasing CAPE content to 1000 μM had a significant impact on plain and SSM membranes of both A1-C1000 and A2.5-C1000 groups by creating more bacteria-free zones on plain membranes and reducing the size and number of biofilm's bacterial layers on SSM membranes along with notably larger gaps on SSM membranes compared to their plain counterparts.

To the best of our knowledge, the phenomenon regarding reduction in layers of bacteria forming the biofilm sheet as a result of sharkskin microtopography and antibacterial activities of the additives has not been reported in the literature to this date.

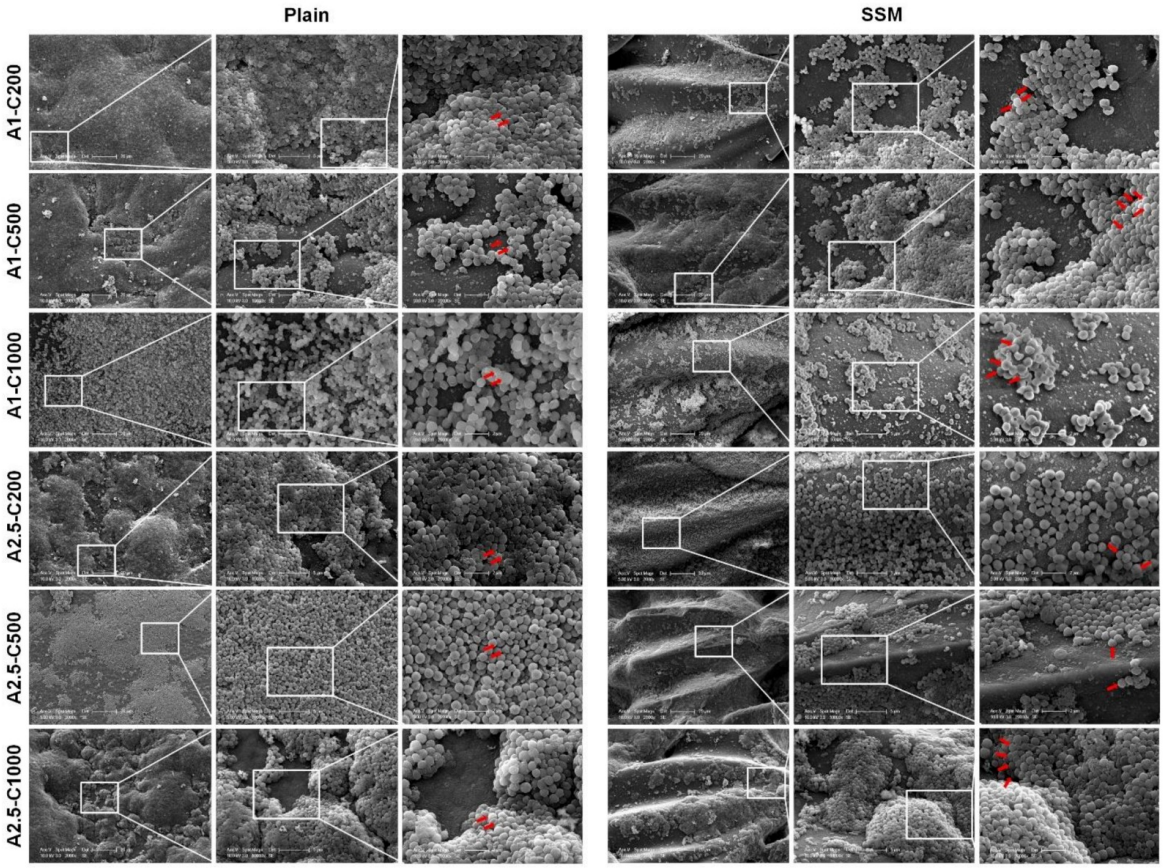


Figure 4.12 SEM images of *S. aureus* growth on plain and SSM CH membranes after 24 h incubation at 37°C. Red arrows indicate layers of bacteria on the surface of the membranes. Scale bars: 20 μm, 5 μm, and 2 μm (SSM: sharkskin mimicked, Amp: Ampicillin sodium salt, CAPE: Caffeic acid phenethyl ester, CH: Chitosan, A1-C200: 1 mg/mL Amp + 200 μM CAPE, A1-C500: 1 mg/mL Amp + 500 μM CAPE, A1-C1000: 1 mg/mL Amp + 1000 μM CAPE, A2.5-C200: 2.5 mg/mL Amp + 200 μM CAPE, A2.5-C500: 2.5 mg/mL Amp + 500 μM CAPE, A2.5-C1000: 2.5 mg/mL Amp + 1000 μM CAPE).

So far based on bacterial MTT assay, SEM images, and release test results, it can be concluded that only SSM A2.5, C1000, A1-C500, A1-C1000, A2.5-C500, and A2.5-C1000 fall under the IC50 threshold both in terms of morphology and MTT assay values. Henceforth, only these groups were selected for further mammalian cell culture experiments.

4.2.4 HDFa and HaCaT Cell Culture Tests

HDFa and HaCaT cells were cultured on SSM A2.5, C1000, A1-C500, A1-C1000, A2.5-C500, and A2.5-C1000 membranes with the seeding density of 4×10^4 cells per well of 24-well plates for both cell types (Figure 4.13). MTT and AlamarBlue assays experiments were conducted on days 1, 3, and 5, post culture with respect to TCP as the positive control. Data are presented in Figure 4.13A to 4.13D. As shown in Figure 4.13A, HDFa cells of SSM C1000, A1-C500, A1-C1000, and A2.5-C1000 had the lowest cell viability values with similar values at 37.1%, 33.1%, 36.5%, and 35.8% respectively on day 1. On the contrary, A2.5, and A2.5-C500 had viability values of 42.7% and 47.1% with the 41.7% value for CH, the negative control. Considering the two most important properties of CAPE being anti-inflammatory and high cytotoxicity, it appears that C1000, A1-C500, A1-C1000, and A2.5-C1000 induce a high levels of cell toxicity compared to that of CH which was expected due to Amp and CAPE release rate results. CAPE's anti-inflammatory effect along with Amp, seemingly influenced HDFa cells in the A2.5-C500 group making it not only the least cytotoxic concentration of Amp-CAPE mix for cell viability of HDFa type but also boosting the number of viable cells compared to CH membranes although not statistically significant. Cell proliferation rates of HDFa agree with MTT assay data in which the highest HDFa proliferation on day 5 belonged to A2.5-C500 (Figure 4.13C). The rest of the experimental groups have relatively similar proliferation rates after 3 and 5 days of incubation.

As for HaCaT viability, represented in Figure 4.13B, CH, A2.5, and A1-C500 groups had the highest cell viability values on day 5 at 380.2%, 339.3%, and 323.2%, respectively. Evidently, the cytotoxicity of Amp and CAPE on HaCaT cells was not

significant enough to induce a statistically significant difference. C1000, on the other hand, had the least HaCaT cell viability at 156.4%, which emphasizes the cytotoxic effects of CAPE at 1000μM concentration. Consequently, A1-C1000 with 185.1% viability and A2.5-C1000 with 212.5% viability had similar MTT values to C1000.

In addition to CAPE, a higher concentration of Amp induced a reduction in the number of viable HaCaT cells as well since the measured MTT assay value for A2.5-C500 was 227.9%. Obtained results were expected based on drug release data. Evaluating AlamarBlue assay data of HaCaT confirmed MTT assay results in which A2.5 and A1-C500 had the highest cell proliferation values like that of CH. As shown in Figure 4.13D, A2.5 increased the cell proliferation rate of HaCaT compared to CH, meaning the higher concentration of Amp-only was, in fact, helpful in boosting HaCaT cell proliferation rate resulting in the increased number of viable cells.

SEM images of HDFa and HaCaT cell types cultured on SSM A2.5, C1000, A1-C500, A1-C1000, A2.5-C500, and A2.5-C1000 along with SSM CH were obtained for days 1, 3, and 5. SSM CH was used as the negative control and glass as the positive control. Figure 4.14, 4.15, and 4.16 shows cells on days 1, 3, and 5.

Similar to MTT and AlamarBlue results for HDFa, cells on A2.5, C1000, A1-C1000, and A2.5-C500 samples appeared to be very well spread and spindle-shaped whereas cells on other membranes were round in shape and fewer in number. The highest population of well-spread cells of HDFa belonged to A2.5 and A2.5-C500 compared to CH negative control.

4.2.5 *In vitro* Enzymatic Degradation

Enzymatic degradation test of SSM CH, A2.5, C1000, A1-C500, A1-C1000, A2.5-C500, and A2.5-C1000 was also performed using lysozyme enzyme. As presented in Figure 4.17 the addition of Amp and CAPE, whether individually or together, remarkably slowed the degradation of SSM CH membranes. It appeared that addition

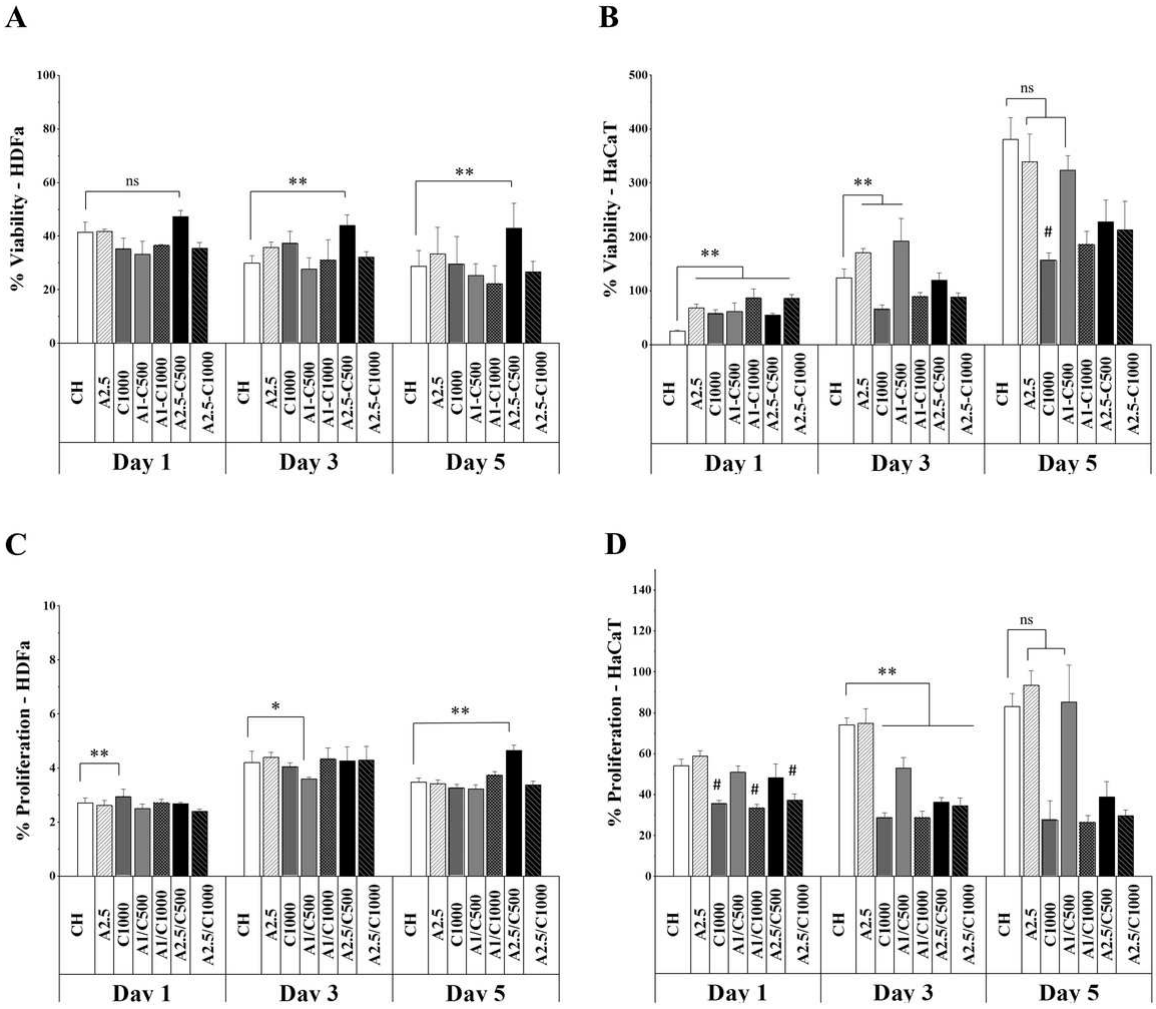


Figure 4.13 **A)** HDFa cell viability (MTT assay) results, **B)** HaCaT cell viability (MTT assay) results, **C)** HDFa cell proliferation (AlamarBlue assay) results, **D)** HaCaT cell proliferation (AlamarBlue assay) results (Mean ± SD, *p < 0.05, **p < 0.001, #p < 0.001 compared to the CH control, n=3, Amp: Ampicillin sodium salt, CAPE: Caffeic acid phenethyl ester, CH: Chitosan, A2.5: 2.5 mg/mL Amp, C1000: 1000 μM CAPE, A1-C500: 1 mg/mL Amp + 500 μM CAPE, A1-C1000: 1 mg/mL Amp + 1000 μM CAPE, A2.5-C500: 2.5 mg/mL Amp + 500 μM CAPE, A2.5-C1000: 2.5 mg/mL Amp + 1000 μM CAPE).

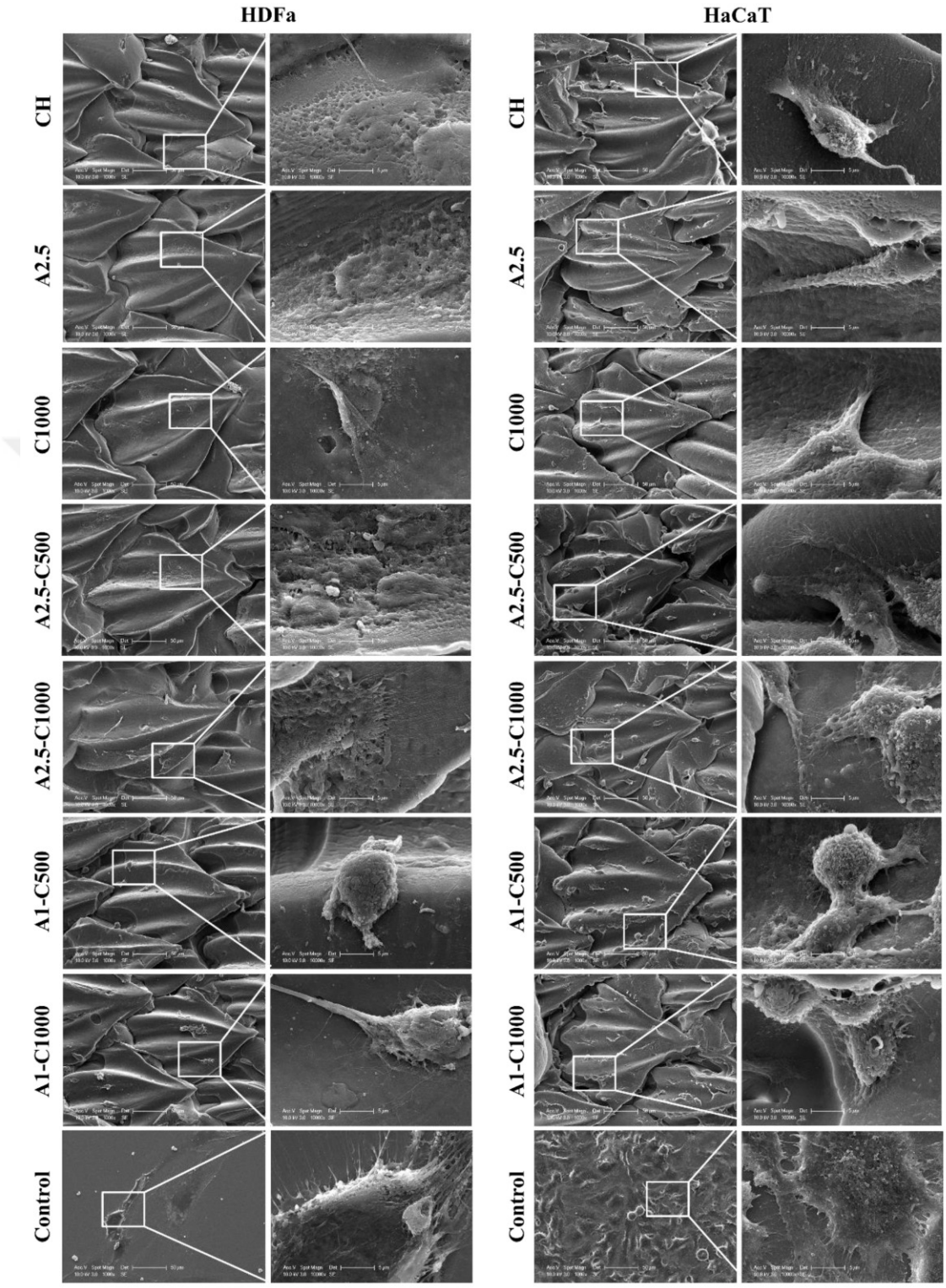


Figure 4.14 SEM images of HDFa and HaCaT on SSM CH membranes on day 1. Scale bars: 200 μm and 50 μm (CH: Chitosan, A2.5: 2.5 mg/mL Amp, C1000: 1000 μM CAPE, A1-C500: 1 mg/mL Amp + 500 μM CAPE, A1-C1000: 1 mg/mL Amp + 1000 μM CAPE, A2.5-C500: 2.5 mg/mL Amp + 500 μM CAPE, A2.5-C1000: 2.5 mg/mL Amp + 1000 μM CAPE, Control: glass slide).

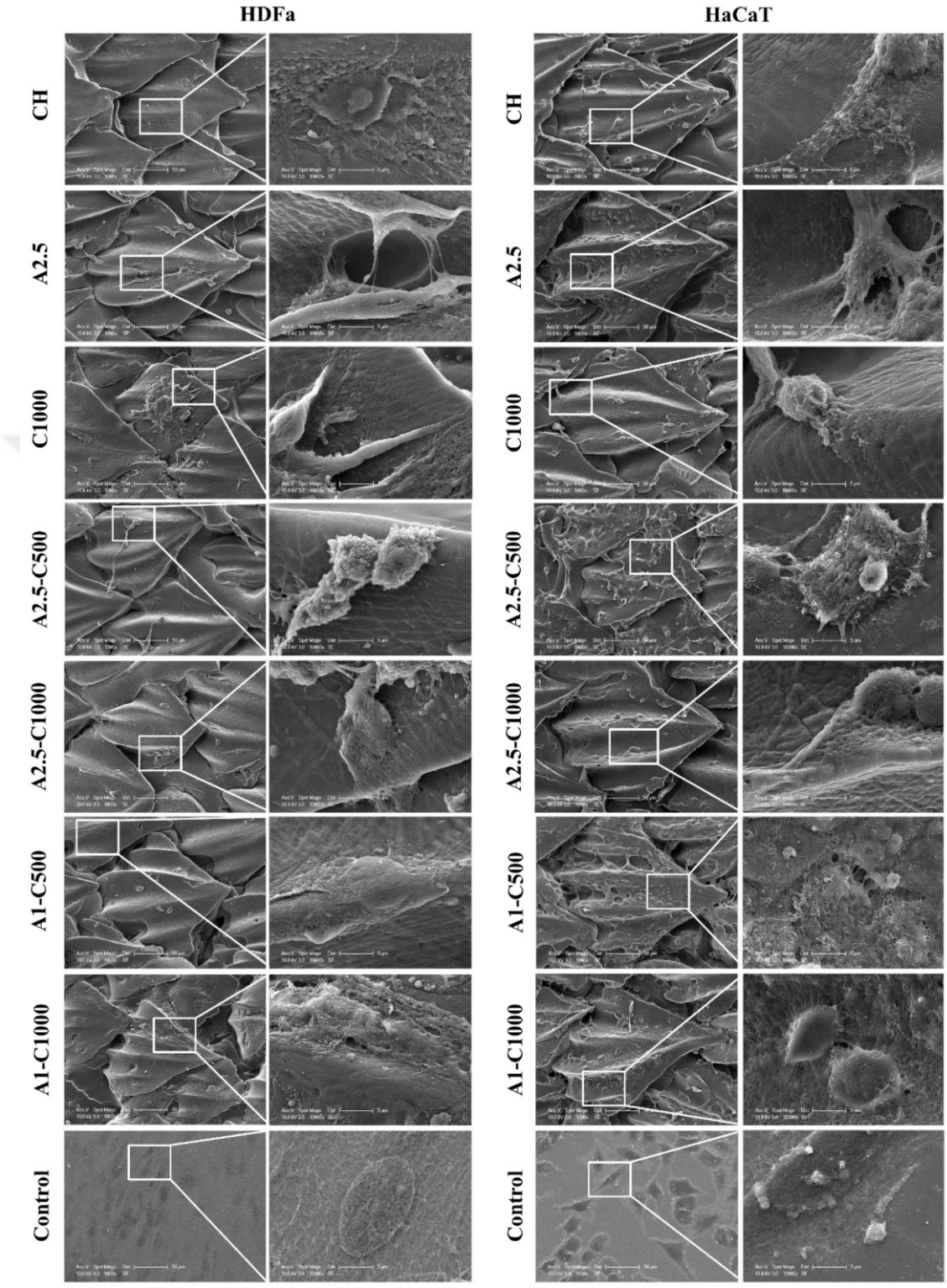


Figure 4.15 SEM images of HDFa and HaCaT on SSM CH membranes on day 3. Scale bars: 200 μm and 50 μm (CH: Chitosan, A2.5: 2.5 mg/mL Amp, C1000: 1000 μM CAPE, A1-C500: 1 mg/mL Amp + 500 μM CAPE, A1-C1000: 1 mg/mL Amp + 1000 μM CAPE, A2.5-C500: 2.5 mg/mL Amp + 500 μM CAPE, A2.5-C1000: 2.5 mg/mL Amp + 1000 μM CAPE, Control: glass slide).

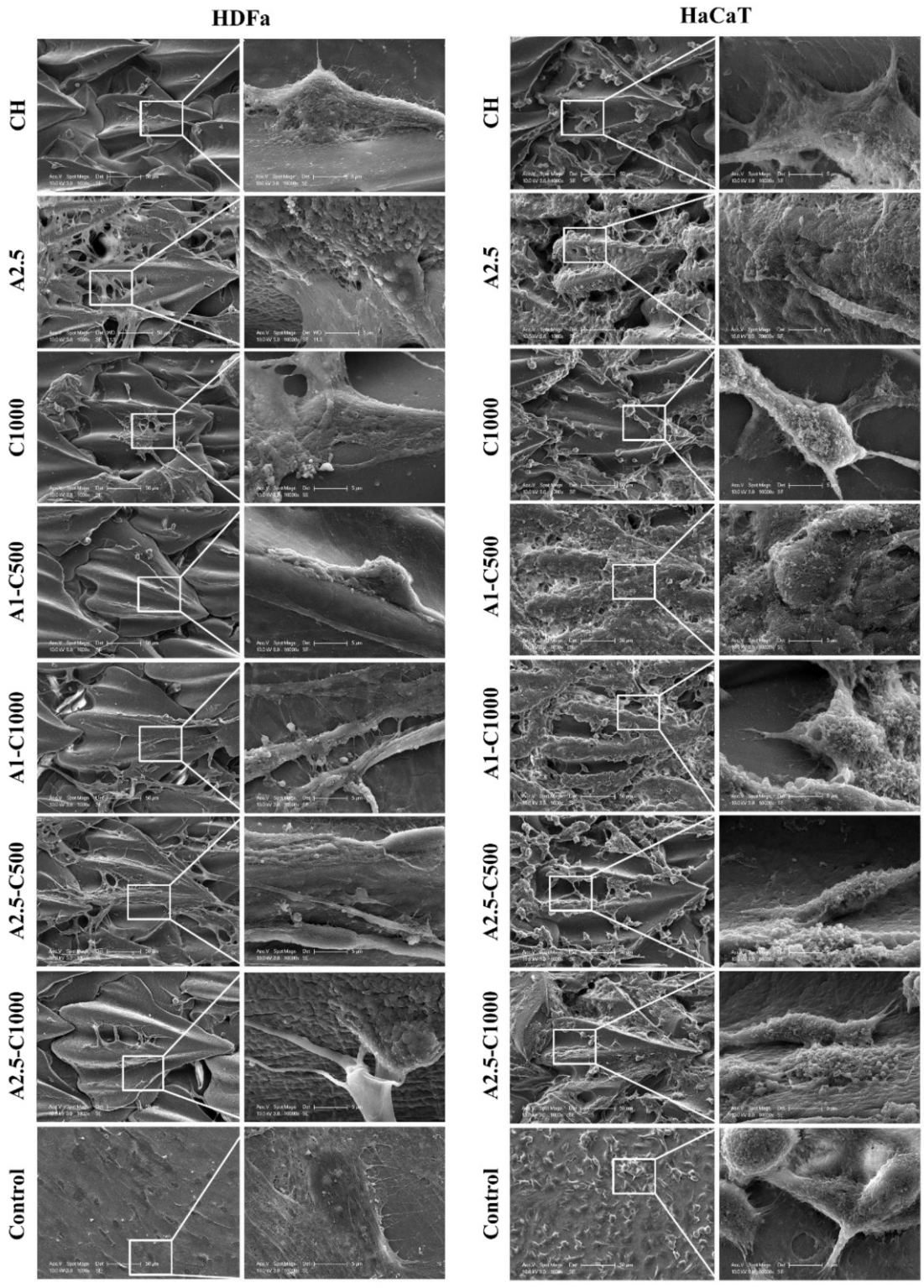


Figure 4.16 SEM images of HDFa and HaCaT on SSM CH membranes on day 5. Scale bars: 200 μm and 50 μm (CH: Chitosan, A2.5: 2.5 mg/mL Amp, C1000: 1000 μM CAPE, A1-C500: 1 mg/mL Amp + 500 μM CAPE, A1-C1000: 1 mg/mL Amp + 1000 μM CAPE, A2.5-C500: 2.5 mg/mL Amp + 500 μM CAPE, A2.5-C1000: 2.5 mg/mL Amp + 1000 μM CAPE, Control: glass slide).

of CAPE at 1000μM concentration to SSM samples dramatically decreased the degradation percentage of SSM CH samples. A1-C500 and A1-C1000 had almost identical degradation percentage and close to that of C1000. A2.5, on the other hand, increased the rate of SSM CH membrane's degradation compared to C1000 but still much slower than SSM CH samples. Addition of CAPE did not change the degradation of A2.5-C500 and A2.5-C1000 in favor of the C1000 sample and their degradation percentage remained like A2.5. A. Lončarević *et al.* conducted a study on the degradation rate of CH porous scaffolds induced in water with and without lysozyme [129]. They concluded that CH scaffolds had a nearly 16% weight loss in PBS medium at the end of 3 weeks.

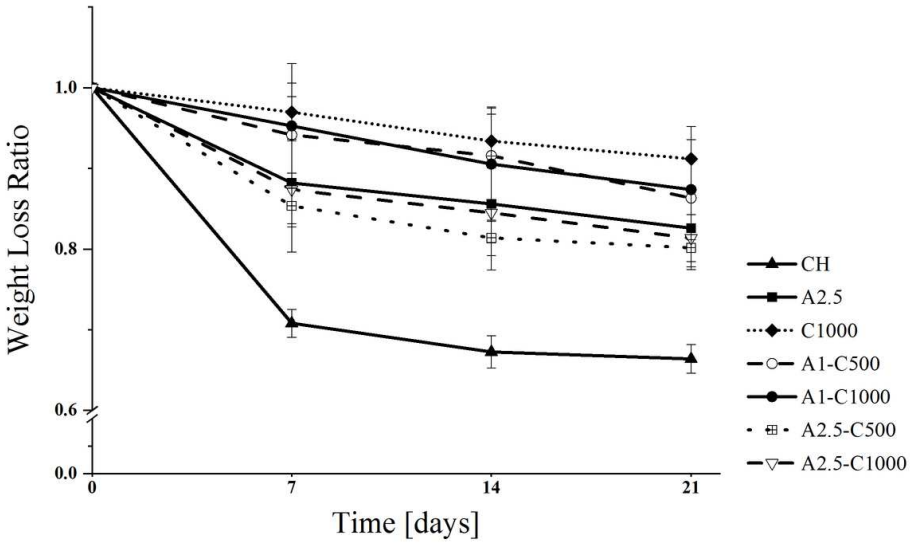


Figure 4.17 Lysozyme-induced enzymatic degradation (CH: Chitosan, A2.5: 2.5 mg/mL Amp, C1000: 1000 μM CAPE, A1-C500: 1 mg/mL Amp + 500 μM CAPE, A1-C1000: 1 mg/mL Amp + 1000 μM CAPE, A2.5-C500: 2.5 mg/mL Amp + 500 μM CAPE, A2.5-C1000: 2.5 mg/mL Amp + 1000 μM CAPE).

According to the obtained results, SSM CH membranes had an average degradation of nearly 30% at the end of 3rd week (21 days). Based on the measurements, the highest degradation rate belongs to CH membrane followed by, A2.5-C500, A2.5-C1000, A2.5, A1-C500, A-C1000, and C1000. The measured swelling ratio of the corresponding groups were: 355.5%, 328.9%, 311.8%, 308.7%, 308.1%, 309.4%, and 291.2%, respectively which followed the same trend as the weight loss of the membranes. Degradation percentages of SSM A2.5, A2.5-C500, and A2.5-C1000 were calculated at 23.1%, 25.8%,

and 24.7% whereas 24h-swelling ratios of these membranes were measured at 308.7%, 328.9%, and 311.8%, respectively. A similar trend was observed for SSM C1000, A1-C500, and A1-C1000, which have percentage weight losses of 8.9%, 13.1%, and 14.8% along with 24 h-swelling ratios of 291.2%, 308.1%, and 309.4%. SSM CH had the highest swelling ratio at 355.5%, which explained the highest degradation compared to the rest of the experimental groups.

4.3 Discussion

Preventing bacterial biofilm formation and growth is the first step in hindering biomaterial surface and implant-associate infections. In a quest to design surfaces with enhanced antibacterial and cytocompatible properties, the study of the duo of sharkskin topography and drug (Amp/CAPE) loaded polymeric membranes was undertaken and reported here. Sharkskin biomimicked membranes were investigated for their potentials as implantable biodegradable drug delivery platform that could reduce the bacterial biofilm growth and promote cell viability and proliferation.

In this chapter the antibacterial, cytotoxicity, drug release, and physicochemical properties of Amp and CAPE loaded CH-based sharkskin mimicked membranes were studied. As the first test, swelling ratio of both plain and sharkskin mimicked membranes were measured. As shown in Figure 4.2, in all experimental groups, the sharkskin micropattern reduced the swelling ratio significantly. Following this, the mechanical properties were studied by measuring the tensile strength of plain membranes. Despite the fact that presence of additives changed the tensile strength of all groups, only A1 was found to have the only statistically significantly different tensile strength value among all experimental groups. Similar results were observed by F.-L. Mi *et al.* in the ultimate tensile strength values of genipin cross-linked CH membrane vs CH membrane. They reported that cross-linking material increased the tensile strength of CH membranes up to a point, but with increasing the concentration of the cross-linker, the value of ultimate tensile strength decreased [216].

For chemical characterization of fabricated membranes, XPS analysis was done. Obtained results, which are shown in Figure 4.4, validated our expectation in which atomic ratios of C/O and C/N increased along with the increase in peak intensity of O1s and C1s in the survey spectrum. Presence of Na atoms was detected in A2.5-C500 as expected. The increase in C/Na ratio from 55.11 in A2.5 to 107.5 in A2.5-C500 meant that the percentage of Na in A2.5 was higher than A2.5-C500 which was reasonable since the increase in C, O, and N atoms content was so high that the overall percentage of Na atoms within the membrane decreased [217],[218]. Apart from XPS, FTIR analysis was also performed. As shown in Figure 4.5, the obtained results all together confirm the presence of Amp and CAPE within the CH membranes. Similar shifts in peak position were observed by Vijayalakshmi *et al.*, Dogan, J Xu *et al.*, and Venkatesan *et al.* in the FTIR spectra of CH upon addition of PEG, tripolyphosphate (TPP), gelatin blends of various concentrations, and carbon nanotubes (CNTs), respectively [219–222]. Since both drugs were present within the polymeric network, their possible effects on surface roughness were studied via AFM. As seen in Figure 4.6, CAPE decreased the surface roughness significantly. In contrast, Amp increased the surface roughness in both A2.5 and A2.5-C500 membranes.

The drug release was one of the most important properties of the hydrogel membranes fabricated here. Therefore, the results of drug release rate, which are shown in Figures 4.7 and 4.8, are in agreement with the literature. Numerous studies have been conducted to this date regarding the combination of Amp with the majority of polymers many of which aimed at designing efficient drug carriers for controlled release. In a study conducted by X. Zhang *et al.* antibacterial activity of Amp-loaded alginate-chitosan fiber was investigated by performing the agar diffusion plate test. Results revealed that not only CH induced an increase in antibacterial activity of fabricated fibers, most probably due to its crosslinking capabilities which allowed for a higher uptake of Amp during the fabrication process, but also Amp could indeed be released from the CH matrix into the surrounding environment and exhibit its antibacterial activity [223]. Incorporation of Amp into CH beads at various Amp concentrations without the use of crosslinkers was investigated by T. Chandy and C.P. Sharma and the antibacterial test results of these beads revealed that Amp can be effectively released

from CH beads and eliminate bacteria [45]. Furthermore, the antibacterial properties of Ampicillin–Chitosan–Polyanion nanoparticles were characterized by Y. Ciro *et al.* in which by utilizing broth micro-dilution method on sensitive and resistant *S. aureus* strains, a nearly 2-fold increase in antibacterial effect of fabricated nanoparticles was reported compared to free Amp. This indicated the effectiveness of Amp encapsulation within polymeric nanostructures in enhancing drug release as opposed to its direct administration [224].

By increasing CAPE concentration, the amount of released Amp increased significantly for both plain and SSM membranes. It is most likely that the presence of CAPE molecules led to a faster transfer of Amp molecules from the membrane into the dH_2O. Higher solubility of Amp in water compared to CAPE, most probably resulted in a higher release rate of Amp instead of CAPE despite the higher molecular weight of Amp ($C_{16}H_{18}N_3NaO_4S$, 371.4 g/mol) in comparison to CAPE ($C_{17}H_{16}O_4$, 284.31 g/mol).

Like Amp, CAPE has been investigated in the literature for its antibacterial potentials while either incorporated into or coated onto polymeric constructs mostly nanoparticles. The need for such studies arose due to the remarkable characteristics of CAPE like antibacterial, anti-inflammatory, antioxidant, antitumor, and antiviral effects. For instance, in a study conducted by T. Arasoglu *et al.* it was shown that CAPE encapsulated Poly-D,lactide-co-glycolide (PLGA) nanoparticles have antibacterial activity against *P. aeruginosa*, *E. coli*, most of all on *S. aureus* and methicillin-resistant *S. aureus* (MRSA). Interestingly, they reported that free CAPE did not induce any antibacterial effect while CAPE encapsulated PLGA nanoparticles had moderate and long-term antibacterial effect towards methicillin-resistant *S. aureus* (MRSA) and *S. aureus*, respectively. They attributed this phenomenon to the low solubility of CAPE in aqueous media as opposed to slow and controlled delivery of CAPE while loaded into PLGA nanoparticles [225]. In another research by M. Ignatova *et al.* CAPE was incorporated into nanofiber mats made of Polyvinylpyrrolidone (PVP), poly(3-hydroxybutyrate) (PHB), and combinations of them. Based on their results, CAPE induced bactericidal effects on *S. aureus* whether it was used as a coating or loaded

into the core of the fiber. Despite the complete eradication of *S. aureus* bacteria by CAPE/PVP/PHB, the growth of *E. coli* could only be inhibited [224]. Several studies have attributed the antibacterial activity of CAPE to the generation of reactive oxygen species (ROS) on the cell wall of bacteria, which induced microorganism's death [226],[227]. On the other hand it has been suggested by Takaisi-Kikuni and Schilcher that CAPE most probably inhibits the polymerase reaction of bacterial RNA [144]. Since the published CAPE release results are in correlation with our findings for CAPE release rate into dH_2O, it can be concluded that CAPE incorporated into the polymer network of CH membranes released into the LB medium, leading to bacterial biofilm reduction most probably via inducing bactericidal effects. As for the release profile of CAPE and Amp together, to the best of our knowledge, there is only one study conducted by Meyuhas *et al.* in which minimum inhibitory concentration (MIC) of CAPE+Amp against *S. aureus* was studied where the optimum concentrations were found to be 16 μM for CAPE and 24 mg/mL for Amp where they were administered directly to the bacterial suspension [228]. They have concluded that while CAPE had significant antibacterial effects on most of the tested Gram-positive bacteria strains, it could not prevent bacterial growth of Gram-negative strains.

After detailed examination of zone of inhibition data and comparing it with drug release and swelling ratio results, it was concluded that most likely the drug release rate is correlated mainly with the swelling ratio of the membranes. This conclusion was drawn since the concentration gradient between the membrane and the medium was the same for both plain and SSM samples however, the amount of released drug was different between plain and SSM membranes with same additive content for both Amp and CAPE. Consequently, the conclusion was made that the key regulator of the drug release in this case is mostly the swelling ratio-associated diffusion, resulting in the release of the loaded drugs.

Comparing obtained results for swelling ration in Figure 4.2 with drug release data in Figures 4.7 and 4.8 showed a perfect correlation between the swelling ratio after 24 h of the membranes and the amount of drug released after 24 h. According to this relation, it can be concluded that the swelling ratio is the key regulator of the

drug release CH membranes. This deduction was in agreement with existing literature regarding drug release mechanisms from CH based structures [229],[230]. For instance, Gull *et al.* investigated the potentials of CH based multi-responsive hydrogels in delivering drugs. The stated that sustained drug delivery by their non-toxic biomaterial was achieved and that the mechanism of the drug release was in fact dependent on the swelling ratio [230]. Furthermore, Damiri *et al.* conducted a study on the controlled release of drugs (caffeine, 5-fluorouracil (5-FU), and ascorbic acid) from CH based hydrogels. Their reported results showed a similar trend between swelling ratio and the *in vitro* drug release which is in agreement with the correlation observed in SSM membranes [229].

In chapter 3, it was established that CH-based sharkskin mimicked membrane has remarkable antibacterial properties by reducing bacterial biofilm formation by nearly 50% for *S. aureus* (ATCC 6538P) cultured in LB broth for 24 h, confirming the results presented here [17]. Moreover H.W. Chien *et al.* showed that the roughness of sharkskin micropatterned PDMS substrates caused a dramatic reduction in bacterial biofilm growth [28]. Similarly, Choi *et al.* reported that under dynamic culture conditions, a significant reduction of bacterial biofilm formation occurred for both *E. coli* and *S. aureus* strains, which were attributed to acute drag force reduction [231]. Furthermore, according to the studies conducted by Xia Pu *et al.*, SSM PDMS surfaces reduced the adhesion of algae as a result of sharkskin's surface microtopography along with PDMS's hydrophobicity [27]. The data presented in Figure 4.10 is in agreement with the literature, proving the undeniable impact of sharkskin topography on reducing the formation of a viable bacterial biofilm layer regardless of the additive type and/or its concentration.

It is well-known that CAPE is a relatively toxic compound extracted from propolis [48].Studies conducted on the mechanism of action and level of cytotoxicity of CAPE have shown that CAPE acts in a selective manner [232] towards some cell types in term of causing cell death [54],[233] while protecting others from it [234]. Due to its cytotoxicity, CAPE has been used as an anticancer drug candidate for the past few decades. Y.J. Lee *et al.* showed that after treating buccal mucosal fibroblast (BF), tongue squa-

mous cell carcinoma (TSCCa), neck metastasis of Gingiva carcinoma (GNM), and oral submucous fibroblast (OSF) cell lines with 25-200 μM concentration range of CAPE, severe cell death occurred for all of them except for BF [235]. In terms of the effect of CAPE on HaCaT cell line, D. Zhou and X. Weng reported that a novel butylated derivative of Caffeic Acid (CA), a bioactive polyphenol component found abundantly in plants with a structure very similar to CAPE [236], not only did not induce toxicity but also protected them from squalene peroxidationinduced stress which is generally caused by UVA irradiation [234]. In short, CAPE seems to have different effects on different cell lines at different doses. Hence it was of utmost importance to study the cytotoxic effects of CAPE on HDFa and HaCaT cell lines. Similar to CAPE, the effect of Amp content on cell viability and proliferation of HDFa and HaCaT were also investigated despite reported cases of its very low cytotoxicity [237]. A. Balupillai *et al.* conducted a study regarding the mechanism of action of CA in photocarcinogenesis of HDFa cells as a result of UVB irradiation. Their reported cell viability (MTT assay) data of cells treated with 0 μM, 6.25 μM, 12.5 μM, 25 μM, 50 μM, 100 μM, and 200 μM concluded that the highest non-toxic CA concentration at 100 μM even though the first notable drop in cell viability was observed 25 μM CA concentration. Also, the optimum CA concentration for preventing UVA-induced photocarcinogenesis was found to be 40 μM, for direct administration of CA to the cultured cells [238]. Apart from CAPE, 2.5 mg/mL Amp concentration of SSM A2.5 did not induce any significant cytotoxicity against HDFa cells compared to SSM CH was in agreement with abovementioned literature [237].

As mentioned above regarding CAPE and CA derivatives, there are reports of their non-toxic effects on HaCaT cell line. D. Zhou and X. Weng synthesized and characterized butylated caffeic acid (BCA) to be used instead of CA as an effective antioxidant for skin protection against UVA-induced environmental stresses. According to their results, CA was administered up to 200 μM concentration to cells exposed to peroxidized squalene and cell viability values showed no cytotoxic effect [234]. In another study conducted by K. M. Lim *et al.* *in vitro* and *in vivo* performance of CAPE in reducing skin inflammation using the HaCaT line as the model cell in *in vitro* experiments was studied. Their findings suggested that direct administration of CAPE

with up to 10 μM concentration significantly reduced secretion of pro-inflammatory cytokines in 20 ng mL TNF-α-stimulated HaCaT cells including IL-1β, IL-6, and TNF-α [236]. Although the concentration of CAPE in our study are far more than the maximum non-toxic amounts reported in the literature, 100 μM for HDFa and 200 μM for HaCaT, the fact that CAPE was entrapped within the SSM CH polymer network prevented its burst release and allowed for the investigation of both antibacterial and cytotoxic effects of high doses of CAPE. So far it can be summarized that SSM CH can be used as a carrier for high amounts of CAPE and Amp with the aim of reducing both bacterial biofilm formation and mammalian cell toxicity.

Looking over SEM images of HaCaT on day 5 revealed similar results compared to HDFa in the sense of being in agreement with MTT and AlamarBlue assay data. As expected from the viability and proliferation results, numbers of well-spread HaCaT cells on A2.5, A1-C500, and A1-C1000 membranes were considerably more than other groups. The sheet of HaCaT cells on A1-C500 looked like a thick, homogenous layer of interconnected cells, entirely covering the sharkskin grooves and riblets. SEM images of HaCaT on SSM A2.5 sample did show higher number of cells compared to C1000, A2.5-C500, and A2.5-C1000 but it was like cell adhesion behavior and cell number of A1-C1000 membrane. Overall, the only group with both high levels of HDFa and HaCaT viability and proliferation along with well-spread cell morphology is A2.5.

The *in vitro* degradation rate of the membranes induced by lysozyme enzyme was studied (Figure 4.17). Since the degradation rate is directly dependent on the water uptake capacity of membranes, obtained data of percentage degradation and swelling were in perfect correlation indicating that the higher the swelling rate, the more weight is lost from the membrane. Additionally, it was observed that by addition of either of the drugs, the degradation rate reduced, suggesting that presence of the additives increased the structural stability of CH membranes. Similar phenomenon was observed by Yasayan while degradation of chitosan and pectin polyelectrolyte (PEC) complex was studied [239]. She reported that the presence of PEC in CH films slowed down the rate of degradation of CH films. El-Sherbiny *et al.* also observed a reduction in degradation rate of CH based nanoparticles at high concentrations of Pluronic (more

than 40%) at 37°C during enzymatic degradation [240].

Overall, our results suggested that not only the sharkskin topography has a huge impact on reducing bacterial biofilm formation, but it also affects drug release and degradation rate of the Amp-CAPE loaded CH-based membranes as well.

5. CONCLUSION

The present thesis demonstrated the impact of sharkskin micropattern on antibacterial and cytocompatibility of chitosan-based hydrogel membranes. In this regard, two studies were conducted: first one focused on understanding the adhesion bacterial and cell on sharkskin mimicked membranes with and without Graphene Oxide (GO). The second study, investigated the potential of sharkskin mimicked membranes in carrying and releases drugs for which Ampicillin sodium salt (Amp) and Caffeic acid phenethyl ester (CAPE) were used as model drugs. CH membranes with actual sharkskin microtopography were fabricated by utilizing soft lithography (PDMS molding) and solution casting methods.

In chapter 3 which presents the first study, GO was used in two forms: as surface coating, and nanocomposite in fabricating membranes. Gram-negative *E. coli*, Gram-positive *S. aureus*, Human dermal Keratinocyte, and mouse fibroblast cells were used in a series of *in vitro* experiments. Early-stage bacterial settlement (ISO 22196 test) and long-term biofilm formation tests revealed that sharkskin micropattern significantly reduces bacterial adhesion during the first 3 h of culture, between 70% and 80%, in both *E. coli* and *S. aureus*, respectively. Moreover, bacterial biofilm formation was reduced because of sharkskin micropattern by nearly 50%. GO showed antibacterial properties on smooth surfaces however this effect was diminished for patterned membranes. The effectiveness of GO on mammalian cell viability and proliferation was remarkable both on smooth membranes and on sharkskin mimicked ones.

Then, in the second study, drug release behavior of sharkskin mimicked chitosan-based membranes was studied. As described in chapter 4, Amp, which is a widely used antibiotic, and CAPE, which is a water insoluble anti-inflammatory drug extracted from propolis were added into the chitosan solution prior to casting. Obtained results indicate that sharkskin topography regulated the swelling ratio of the fabricated membranes, thus, controlling the amount of drug released from them via diffusion. It was

also found that high doses of CAPE can be delivered by loading into chitosan polymer solution. Additionally, the antibacterial activity of sharkskin mimicked chitosan membrane is increased by addition of Amp and CAPE, both individually and together.

The membranes with sharkskin microtopography proved to be effective in simultaneously promoting cell proliferation and inhibiting bacterial biofilm formation. Employing topographies with inherent antibacterial properties, such as sharkskin, may be useful in reducing surface-associated bacterial contaminations and infections such as medical devices and inpatient-care equipment. Additionally, the biodegradable nature of the base polymer could bring about many applications in the biomedical field as an implantable membrane with dual functionality, cytocompatibility, and antibacterial activity.

REFERENCES

1. Moriarty, T. F., S. A. J. Zaat, and H. J. Busscher, *Biomaterials Associated Infection: Immunological Aspects and Antimicrobial Strategies*, Springer, 2013.

2. Weishaupt, R., J. N. Zünd, L. Heuberger, F. Zuber, G. Faccio, F. Robotti, A. Ferrari, G. Fortunato, Q. Ren, K. Maniura-Weber, and A. G. Guex, "Antibacterial, cytocompatible, sustainably sourced: Cellulose membranes with bifunctional peptides for advanced wound dressings," *Advanced Healthcare Materials*, Vol. 9, no. 7, p. 1901850, 2020.

3. Clainche, T. L., D. Linklater, S. Wong, P. Le, S. Juodkazis, X. L. Guével, J.-L. Coll, E. P. Ivanova, and V. Martel-Frachet, "Mechano-bactericidal titanium surfaces for bone tissue engineering," *ACS Applied Materials & Interfaces*, Vol. 12, no. 43, pp. 48272–48283, 2020. PMID: 33054152.

4. Leaper, D., A. J. McBain, A. Kramer, O. Assadian, J. L. A. Sanchez, J. Lumio, and M. Kiernan, "Healthcare associated infection: novel strategies and antimicrobial implants to prevent surgical site infection," *Annals of the Royal College of Surgeons of England*, Vol. 92, no. 6, pp. 453–458, 2010.

5. Grill, M. F., and R. K. Maganti, "Neurotoxic effects associated with antibiotic use: management considerations," *Br J Clin Pharmacol*, Vol. 72, no. 3, pp. 381–93, 2011.

6. Darouiche, R. O., "Treatment of infections associated with surgical implants," *New England Journal of Medicine*, Vol. 350, no. 14, pp. 1422–1429, 2004.

7. Kuehn, C., K. Graf, W. Heuer, A. Hilfiker, I. F. Chaberny, M. Stiesch, and A. Haverich, "Economic implications of infections of implantable cardiac devices in a single institution," *European Journal of Cardio-Thoracic Surgery*, Vol. 37, no. 4, pp. 875–879, 2010.

8. Choo, E. J., and H. F. Chambers, "Treatment of methicillin-resistant staphylococcus aureus bacteremia," *Infection & chemotherapy*, Vol. 48, no. 4, pp. 267–273, 2016.

9. Cunha, B. A., "Antibiotic side effects," *Medical Clinics of North America*, Vol. 85, no. 1, pp. 149–185, 2001.

10. Westphal, J. F., D. Vetter, and J. M. Brogard, "Hepatic side-effects of antibiotics," *Journal of Antimicrobial Chemotherapy*, Vol. 33, no. 3, pp. 387–401, 1994.

11. Wierzbicki, M., S. Jaworski, E. Sawosz, A. Jung, G. Gielerak, H. Jaremek, W. Łojkowski, B. Woźniak, L. Stobiński, A. Małolepszy, and A. Chwalibog, "Graphene oxide in a composite with silver nanoparticles reduces the fibroblast and endothelial cell cytotoxicity of an antibacterial nanoplatform," *Nanoscale Research Letters*, Vol. 14, no. 2, p. 320, 2019.

12. Ghavamian, S., I. D. Hay, R. Habibi, T. L. T, and V. J. Cadarso, "Three-dimensional micropatterning deters early bacterial adherence and can eliminate colonization," *ACS Applied Materials & Interfaces*, 2021.

13. Ghimire, A., and J. Song, "Anti-periprosthetic infection strategies: From implant surface topographical engineering to smart drug-releasing coatings," *ACS Applied Materials & Interfaces*, Vol. 13, no. 8, pp. 20921–20937, 2021.

14. Ren, X., H. C. van der Mei, Y. Ren, H. J. Busscher, and B. W. Peterson, "Antimicrobial loading of nanotubular titanium surfaces favoring surface coverage by mammalian cells over bacterial colonization," *Materials Science and Engineering: C*, Vol. 123, p. 112021, 2021.

15. Jenkins, J., J. Mantell, C. Neal, A. Gholinia, P. Verkade, A. H. Nobbs, and B. Su, "Antibacterial effects of nanopillar surfaces are mediated by cell impedance, penetration and induction of oxidative stress," *Nature Communications*, Vol. 11, no. 1, p. 1626, 2020.

16. Jaggessar, A., H. Shahali, A. Mathew, and P. Yarlagadda, "Bio-mimicking nano and microstructured surface fabrication for antibacterial properties in medical implants," *J Nanobiotechnology*, Vol. 15, no. 1, p. 64, 2017.

17. Rostami, S., F. Puza, M. Ucak, E. Ozgur, O. Gul, U. K. Ercan, and B. Garipcan, "Bifunctional sharkskin mimicked chitosan/graphene oxide membranes: Reduced biofilm formation and improved cytocompatibility," *Applied Surface Science*, Vol. 544, p. 148828, 2021.

18. Khalid, S., A. Gao, G. Wang, P. K. Chu, and H. Wang, "Tuning surface topographies on biomaterials to control bacterial infection," *Biomaterials Science*, Vol. 8, no. 24, pp. 6840–6857, 2020.

19. Arisoy, F. D., K. W. Kolewe, B. Homyak, I. S. Kurtz, J. D. Schiffman, and J. J. Watkins, "Bioinspired photocatalytic shark-skin surfaces with antibacterial and antifouling activity via nanoimprint lithography," *ACS Applied Materials & Interfaces*, Vol. 10, no. 23, pp. 20055–20063, 2018.

20. Chen, H., X. Zhang, L. Ma, D. Che, D. Zhang, and T. S. Sudarshan, "Investigation on large-area fabrication of vivid shark skin with superior surface functions," *Applied Surface Science*, Vol. 316, pp. 124–131, 2014.

21. Chen, D., Y. Liu, H. Chen, and D. Zhang, "Bio-inspired drag reduction surface from sharkskin," *Biosurface and Biotribology*, Vol. 4, no. 2, pp. 39–45, 2018.

22. Luo, Y., and Z. D. Z, "Investigation on fabricating continuous vivid sharkskin surface by bio-replicated rolling method," *Applied Surface Science*, Vol. 282, pp. 370–375, 2013.

23. Peng, Y. L., C. G. Lin, and L. W. L, "The preliminary study on antifouling mechanism of shark skin," *Advanced Materials Research*, Vol. 79, no. 82, pp. 977–980, 2009.

24. Bechert, D., and W. Reif, "On the drag reduction of the shark skin," *American Institute of Aeronautics and Astronautics*, Vol. In 23rd Aerospace Sciences Meeting, 1985.

25. Han, X., D. Zhang, X. Li, and Y. Li, "Bio-replicated forming of the biomimetic drag-reducing surfaces in large area based on shark skin," *Chinese Science Bulletin*, Vol. 53, no. 10, p. 1587, 2008.

26. Lang AW, Motta P, H. P., and W. M, "Bristled shark skin: a microgeometry for boundary layer control?," *Bioinspir Biomim*, Vol. 3, no. 4, p. 046005, 2008.

27. Pu, X., G. Li, and H. Huang, "Preparation, anti-biofouling and drag-reduction properties of a biomimetic shark skin surface," *Biology Open*, Vol. 5, no. 4, pp. 389–396, 2016.

28. Chien, H. W., X. Y. Chen, W. P. Tsai, and M. Lee, "Inhibition of biofilm formation by rough shark skin-patterned surfaces," *Colloids Surf B Biointerfaces*, Vol. 186, p. 110738, 2020.

29. de Queiroz Antonino, R. S. C. M., B. R. P. L. Fook, V. A. de Oliveira Lima R I de Farias Rached, E. P. N. Lima, R. J. da Silva Lima, C. A. P. Covas, and M. V. L. Fook, "Preparation and characterization of chitosan obtained from shells of shrimp (litopenaeus vannamei boone)," *Marine Drugs*, Vol. 15, no. 5, p. 141, 2017.

30. Choi, W., C. Lee, D. Lee, Y. J. Won, G. W. Lee, M. G. Shin, B. Chun, T. S. Kim, H. D. Park, H. W. Jung, J. S. Lee, and J. H. Lee, "Sharkskin-mimetic desalination membranes with ultralow biofouling," *Journal of Materials Chemistry A*, Vol. 6, no. 45, pp. 23034–23045, 2018.

31. May, R. M., M. G. Hoffman, M. J. Sogo, A. E. Parker, G. A. O'Toole, A. B. Brennan, S. T, and Reddy, "Micro-patterned surfaces reduce bacterial colonization and biofilm formation in vitro: Potential for enhancing endotracheal tube designs," *Clinical and Translational Medicine*, Vol. 3, no. 1, p. 8, 2014.

32. Chung, K. K., J. F. Schumacher, E. M. Sampson, R. A. Burne, P. J. Antonelli, and A. B. Brennan, "Impact of engineered surface microtopography on biofilm formation of staphylococcus aureus," *Biointerphases*, Vol. 2, no. 2, pp. 89–94, 2007.

33. Goy, R. C., S. T. B. Morais, and O. B. G. Assis, "Evaluation of the antimicrobial activity of chitosan and its quaternized derivative on e. coli and s. aureus growth," *Revista Brasileira de Farmacognosia*, Vol. 26, no. 1, pp. 122–127, 2016.

34. Hu, X., Y. Wang, J. O. Yang, Y. Li, P. Wu, H. Zhang, D. Yuan, Y. Liu, Z. Wu, and Z. Liu, "Synthesis of graphene oxide nanoribbons/chitosan composite membranes for the removal of uranium from aqueous solutions," *Frontiers of Chemical Science and Engineering*, 2020.

35. Yang S, Z. X., and Z. D, "Electrospun chitosan/poly (vinyl alcohol)/graphene oxide nanofibrous membrane with ciprofloxacin antibiotic drug for potential wounddressing application," *Int J Mol Sci [Internet]*, Vol. 20, no. 18, 2019.

36. Dinescu, S., M. Ionita, S. R. Ignat, M. Costache, and A. Hermenean, "Graphene oxide enhances chitosan-based 3d scaffold properties for bone tissue engineering," *Int J Mol Sci*, Vol. 20, no. 20, 2019.

37. Hermenean, A., A. Codreanu, H. Herman, C. Balta, M. Rosu, C. V. Mihali, A. Ivan, S. Dinescu, M. Ionita, and M. Costache, "Chitosan-graphene oxide 3d scaffolds as promising tools for bone regeneration in critical-size mouse calvarial defects," *Scientific reports*, Vol. 7, no. 1, pp. 16641–16641, 2017.

38. Perreault, F., A. F. de Faria, S. Nejati, and M. Elimelech, "Antimicrobial properties of graphene oxide nanosheets: Why size matters," *ACS Nano*, Vol. 9, no. 7, pp. 7226–7236, 2015.

39. Wojtoniszak, M., X. Chen, R. J. Kalenczuk, A. Wajda, J. Łapczuk, M. Kurzewski, M. Drozdzik, P. K. Chu, and E. Borowiak-Palen, "Synthesis, dispersion, and cytocompatibility of graphene oxide and reduced graphene oxide," *Colloids and Surfaces B: Biointerfaces*, Vol. 89, pp. 79–85, 2012.

40. Zuo, P. P., H. F. Feng, Z. Z. Xu, L. F. Zhang, Y. L. Zhang, W. Xia, and W. Q. Zhang, "Fabrication of biocompatible and mechanically reinforced graphene oxide-chitosan nanocomposite films," *Chemistry Central Journal*, Vol. 7, no. 1, p. 39, 2013.

41. Depan, D., B. Girase, J. S. Shah, and R. D. K. Misra, "Structure–process–property relationship of the polar graphene oxide-mediated cellular response and stimulated growth of osteoblasts on hybrid chitosan network structure nanocomposite scaffolds," *Acta Biomaterialia*, Vol. 7, no. 9, pp. 3432–3445, 2011.

42. Martínez-Camacho, A. P., M. O. Cortez-Rocha, J. M. Ezquerra-Brauer, A. Z. Graciano-Verdugo, F. Rodriguez-Félix, M. M. Castillo-Ortega, M. S. Yépiz-Gómez, and M. Plascencia-Jatomea, "Chitosan composite films: Thermal, structural, mechanical and antifungal properties," *Carbohydrate Polymers*, Vol. 82, no. 2, pp. 305–315, 2010.

43. Mitra, A., and B. Dey, "Chitosan microspheres in novel drug delivery systems," *Indian J Pharm Sci*, Vol. 73, no. 4, pp. 355–66, 2011.

44. Chandy, T., and C. P. Sharma, "Chitosan matrix for oral sustained delivery of ampicillin," *Biomaterials*, Vol. 14, no. 12, pp. 939–944, 1993.

45. Fernández-Hidalgo, N., B. Almirante, J. Gavaldà, M. Gurgui, C. Peña, A. de Alarcón, J. Ruiz, I. Vilacosta, M. Montejo, N. Vallejo, F. López-Medrano, A. Plata, J. López, C. Hidalgo-Tenorio, J. Gálvez, C. Sáez, J. M. Lomas, M. Falcone, J. de la Torre, X. Martínez-Lacasa, and A. Pahissa, "Ampicillin plus ceftriaxone is as effective as ampicillin plus gentamicin for treating enterococcus faecalis infective endocarditis," *Clin Infect Dis*, Vol. 56, no. 9, pp. 1261–8, 2013.

46. Hussein-Al-Ali, S. H., M. E. E. Zowalaty, M. Z. Hussein, B. M. Geilich, and T. J. Webster, "Synthesis, characterization, and antimicrobial activity of an ampicillin-conjugated magnetic nanoantibiotic for medical applications," *Int J Nanomedicine*, Vol. 9, pp. 3801–3814, 2014.

47. Tolba, M. F., S. S. Azab, A. E. Khalifa, S. Z. Abdel-Rahman, and A. B. Abdel-Naim, "Caffeic acid phenethyl ester, a promising component of propolis with a plethora of biological activities: a review on its anti-inflammatory, neuroprotective, hepatoprotective, and cardioprotective effects," *IUBMB Life*, Vol. 65, no. 8, pp. 699–709, 2013.

48. Tolomelli, A., A. Ricci, A. Viola, M. Bassan, L. Ferrari, L. Ferrazzano, G. Martelli, A. Mattellone, and W. Cabri, "Ampicillin sodium: Isolation, identification and synthesis of the last unknown impurity after 60 years of clinical use," *Journal of Pharmaceutical and Biomedical Analysis*, Vol. 191, p. 113584, 2020.

49. Baranowska-Korczyc, A., A. Warowicka, M. Jasiurkowska-Delaporte, B. Grześkowiak, M. Jarek, B. M. Maciejewska, J. Jurga-Stopa, and S. Jurga, "Antimicrobial electrospun poly(ϵcaprolactone) scaffolds for gingival fibroblast growth," *RSC Advances*, Vol. 6, no. 24, pp. 19647–19656, 2016.

50. Anal, A. K., and W. F. Stevens, "Chitosan–alginate multilayer beads for controlled release of ampicillin," *International Journal of Pharmaceutics*, Vol. 290, no. 1, pp. 45–54, 2005.

51. Liu, H., K. K. Leonas, and Y. Zhao, "Antimicrobial properties and release profile of ampicillin from electrospun poly(ϵepsilon;-caprolactone) nanofiber yarns," *Journal of Engineered Fibers and Fabrics*, Vol. 5, no. 4, p. 155892501000500402, 2010.

52. Ozturk, G., Z. Ginis, S. Akyol, G. Erden, A. Gurel, and O. Akyol, "The anticancer mechanism of caffeic acid phenethyl ester (cape): review of melanomas, lung and prostate cancers," *Eur Rev Med Pharmacol Sci*, Vol. 16, no. 15, pp. 2064–8, 2012.

53. Chiao, C., A. M. Carothers, D. Grunberger, G. Solomon, G. A. Preston, and J. C. Barrett, "Apoptosis and altered redox state induced by caffeic acid phenethyl ester (cape) in transformed rat fibroblast cells," *Cancer Research*, Vol. 55, no. 16, p. 3576, 1995.

54. Ignatova, M. G., N. E. Manolova, I. B. Rashkov, N. D. Markova, R. A. Toshkova, A. K. Georgieva, and E. B. Nikolova, "Poly(3-hydroxybutyrate)/caffeic acid electrospun fibrous materials coated with polyelectrolyte complex and their antibacterial activity and in vitro antitumor effect against hela cells," *Materials Science and Engineering: C*, Vol. 65, pp. 379–392, 2016.

55. Yordanov, Y., "Caffeic acid phenethyl ester (cape): cornerstone pharmacological studies and drug delivery systems," *Pharmacia*, Vol. 66, no. 4, pp. 223–231, 2019.

56. Bankova, V., M. Popova, and B. Trusheva, "The phytochemistry of the honeybee," *Phytochemistry*, Vol. 155, pp. 1–11, 2018.

57. Ketkar, S., S. K. Pagire, N. R. Goud, K. Mahadik, A. Nangia, and A. Paradkar, "Tracing the architecture of caffeic acid phenethyl ester cocrystals: Studies on crystal structure, solubility, and bioavailability implications," *Crystal Growth & Design*, Vol. 16, no. 10, pp. 5710–5716, 2016.

58. Wang, X., J. Pang, J. A. Maffucci, D. S. Pade, R. A. Newman, S. M. Kerwin, P. D. Bowman, and S. Stavchansky, "Pharmacokinetics of caffeic acid phenethyl ester and its catechol-ring fluorinated derivative following intravenous administration to rats," *Biopharmaceutics & Drug Disposition*, Vol. 30, no. 5, pp. 221–228, 2009.

59. Kalepu, S., and V. Nekkanti, "Insoluble drug delivery strategies: review of recent advances and business prospects," *Acta Pharmaceutica Sinica B*, Vol. 5, no. 5, pp. 442–453, 2015.

60. Lee, S. J., M. S. Kang, J. S. Oh, H. S. Na, Y. Lim, Y. I. Jeong, and H. C. Lee, "Caffeic acid-conjugated chitosan derivatives and their anti-tumor activity," *Archives of Pharmacal Research*, Vol. 36, no. 12, pp. 1437–1446, 2013.

61. Proksch, E., J. M. Brandner, and J. M. Jensen, "The skin: an indispensable barrier," *Experimental Dermatology*, Vol. 17, no. 12, pp. 1063–1072, 2008.

62. Naresh, M. D., V. Arumugam, and R. Sanjeevi, "Mechanical behaviour of shark skin," *Journal of Biosciences*, Vol. 22, no. 4, pp. 431–437, 1997.

63. Yoshinaka, R., K. Sato, H. Anbe, M. Sato, and Y. Shimizu, "Distribution of collagen in body muscle of fishes with different swimming modes," *Comparative Biochemistry and Physiology Part B: Comparative Biochemistry*, Vol. 89, no. 1, pp. 147–151, 1988.

64. Coppola, D., M. Oliviero, G. A. Vitale, C. Lauritano, I. D'Ambra, S. Iannace, and D. de Pascale, "Marine collagen from alternative and sustainable sources: Extraction, processing and applications," *Marine Drugs*, Vol. 18, no. 4, p. 214, 2020.

65. Alexander, R. M., "Mechanical design in organisms. s. a. wainwright , w. d. biggs , j. d. currey , j. m. gosline," *The Quarterly Review of Biology*, Vol. 51, no. 4, pp. 567–568, 1976.

66. Lee, M., "Shark skin: Taking a bite out of bacteria. in remarkable natural material surfaces and their engineering potential," *Springer International Publishing*, pp. 15–27, 2014.

67. Lang, A., M. L. Habegger, and P. Motta, "Shark skin drag reduction," *In Encyclopedia of Nanotechnology*, pp. 2394–2400, 2012.

68. Gilbert, P. W., "Biology and behaviour of sharks," *Endeavour*, Vol. 8, no. 4, pp. 179–187, 1984.

69. Magin, C. M., S. P. Cooper, and A. B. Brennan, "Non-toxic antifouling strategies," *Materials Today*, Vol. 13, no. 4, pp. 36–44, 2010.

70. Martin, R. A., A. D. Maddalena, and R. C. f S Research, "Field guide to the great white shark," *ReefQuest Centre for Shark Research*, 2003.

71. Bhushan, B., "Shark-skin surface for fluid-drag reduction in turbulent flow," *In Biomimetics: Bioinspired Hierarchical-Structured Surfaces for Green Science and Technology*, pp. 327–382, 2016.

72. Dillon, E. M., R. D. Norris, and A. O'Dea, "Dermal denticles as a tool to reconstruct shark communities," *Marine Ecology Progress Series*, Vol. 566, pp. 117–134, 2017.

73. Lang, A. W., P. Motta, P. Hidalgo, and M. Westcott, "Bristled shark skin: a microgeometry for boundary layer control?," *Bioinspir Biomim*, Vol. 3, no. 4, p. 046005, (2008.

74. Bhushan, B., "Shark skin effect," *In Encyclopedia of Nanotechnology*, pp. 2400–2411, 2012.

75. Liu, Y., H. Gu, Y. Jia, J. Liu, H. Zhang, R. Wang, B. Zhang, H. Zhang, and Zhang, "Design and preparation of biomimetic polydimethylsiloxane (pdms) films with superhydrophobic, selfhealing and drag reduction properties via replication of shark skin and si-atrp," *Chemical Engineering Journal*, Vol. 356, pp. 318–328, 2019.

76. Dean, B., and B. Bhushan, "Shark-skin surfaces for fluid-drag reduction in turbulent flow: a review," *Philosophical Transactions of the Royal Society A: Mathematical, Physical and Engineering Sciences*, Vol. 368, no. 1929, pp. 4775–4806, 2010.

77. Crew, S., "Shark speed test fastest shark in the ocean? | guadalupe island sharks?," *See https://horizoncharters.com/shark-speed-test-fastest-shark-ocean/ (accessed)*, December 27, 2017.

78. Carman, M. L., T. G. Estes, A. W. Feinberg, J. F. Schumacher, W. Wilkerson, L. H. Wilson, M. E. Callow, J. A. Callow, and A. B. Brennan, "Engineered antifouling microtopographies – correlating wettability with cell attachment," *Biofouling*, Vol. 22, no. 1, pp. 11–21, 2006.

79. Miyazaki, M., H. Moriya, and A. Miyauchi, "Biomimetic design inspired sharkskin denticles for growth suppression of biofilm," *Journal of Photopolymer Science and Technology*, Vol. 32, no. 2, pp. 295–301, 2019.

80. Sullivan, T., and F. Regan, "The characterization, replication and testing of dermal denticles of scyliorhinus canicula for physical mechanisms of biofouling prevention," *Bioinspir Biomim*, Vol. 6, no. 4, p. 046001, 2011.

81. Magin, C. M., D. B. Neale, M. C. Drinker, B. J. Willenberg, S. T. Reddy, K. M. L. Perle, G. S. Schultz, and A. B. Brennan, "Evaluation of a bilayered, micropatterned hydrogel dressing for full-thickness wound healing," *Exp Biol Med (Maywood)*, Vol. 241, no. 9, pp. 986–95, 2016.

82. Reddy, S. T., K. K. Chung, C. J. McDaniel, R. O. Darouiche, J. Landman, and A. B. Brennan, "Micropatterned surfaces for reducing the risk of catheter-associated urinary tract infection: An in vitro study on the effect of sharklet micropatterned surfaces to inhibit bacterial colonization and migration of uropathogenic escherichia coli," *J Endourol*, Vol. 25, no. 9, pp. 1547–1552, 2011.

83. Mann, E. E., D. Manna, M. R. Mettetal, R. M. May, E. M. Dannemiller, K. K. Chung, A. B. Brennan, and S. T. Reddy, "Surface micropattern limits bacterial contamination," *Antimicrobial Resistance and Infection Control*, Vol. 3, no. 1, p. 28, 2014.

84. Luo, Y., and Z. Deyuan, "Recent progress in exploring drag reduction mechanism of real sharkskin surface: A review," *Journal of Mechanics in Medicine and Biology*, Vol. 15, no. 3, p. 1530002, 2014.

85. Liu, G., Z. Yuan, Z. Qiu, S. Feng, Y. Xie, D. Leng, and X. Tian, "A brief review of bio-inspired surface technology and application toward underwater drag reduction," *Ocean Engineering*, Vol. 199, p. 106962, 2020.

86. Pu, X., G. Li, and Y. Liu, "Progress and perspective of studies on biomimetic shark skin drag reduction," *ChemBioEng Reviews*, Vol. 3, no. 1, pp. 26–40, 2016.

87. May, R., C. M. Magin, E. E. Mann, M. C. Drinker, J. C. Fraser, C. A. Siedlecki, A. B. Brennan, and S. T. Reddy, "An engineered micropattern to reduce bacterial colonization, platelet adhesion and fibrin sheath formation for improved biocompatibility of central venous catheters," *Clinical and Translational Medicine*, Vol. 4, no. 1, p. 9, 2015.

88. Little, B. J., P. Wagner, J. S. Maki, M. Walch, and R. Mitchell, "Factors influencing the adhesion of microorganisms to surfaces," *The Journal of Adhesion*, Vol. 20, no. 3, pp. 187–210, 1986.

89. Flemming, H. C., "Microbial biofouling: Unsolved problems, insufficient approaches, and possible solutions," *In Biofilm Highlights*, pp. 81–109., 2011.

90. Ranganathan, V., "Biofilms: Microbial cities of scientific significance," *Journal of Microbiology & Experimentation*, Vol. 1, 2014.

91. Crouzet, M., C. L. Senechal, V. S. Brözel, P. Costaglioli, C. Barthe, M. Bonneu, B. Garbay, and S. Vilain, "Exploring early steps in biofilm formation: set-up of an experimental system for molecular studies," *BMC microbiology*, Vol. 14, pp. 253–253, 2014.

92. Subbiahdoss, G., R. Kuijer, D. W. Grijpma, H. C. van der Mei, and H. J. Busscher, "Microbial biofilm growth vs. tissue integration: "the race for the surface" experimentally studied," *Acta Biomaterialia*, Vol. 5, no. 5, pp. 1399–1404, 2009.

93. Alotaibi, G. F., and M. A. Bukhari, "Factors influencing bacterial biofilm formation and development," *Am J Biomed Sci & Res*, Vol. 12, no. 6, pp. 617–626, 2021.

94. Molobela, I. P., and F. M. Ilunga, "Impact of bacterial biofilms: the importance of quantitative biofilm studies," *Annals of Microbiology*, Vol. 62, no. 2, pp. 461–467, 2012.

95. Khatoon, Z., C. D. McTiernan, E. J. Suuronen, T. F. Mah, and E. I. Alarcon, "Bacterial biofilm formation on implantable devices and approaches to its treatment and prevention," *Heliyon*, Vol. 4, no. 12, p. e01067, 2018.

96. Nyström, T., "Aging in bacteria," *Current Opinion in Microbiology*, Vol. 5, no. 6, pp. 596–601, 2002.

97. Kumari, A., S. Mankotia, B. Chaubey, M. Luthra, and R. Singh, "Role of biofilm morphology, matrix content and surface hydrophobicity in the biofilm-forming capacity of various candida species," *J Med Microbiol*, Vol. 67, no. 6, pp. 889–892, 2018.

98. Oliveira, A., and M. d L Ribeiro de Souza da Cunha, "Bacterial biofilms with emphasis on coagulase-negative staphylococci," *Journal of Venomous Animals and Toxins Including Tropical Diseases - J VENOM ANIM TOXINS TROP DIS*, Vol. 14, 2008.

99. Leriche, V., P. Sibille, and B. Carpentier, "Use of an enzyme-linked lectinsorbent assay to monitor the shift in polysaccharide composition in bacterial biofilms," *Appl Environ Microbiol*, Vol. 66, no. 5, pp. 1851–6, 2000.

100. Donlan, R. M., and J. W. Costerton, "Biofilms: survival mechanisms of clinically relevant microorganisms," *Clin Microbiol Rev*, Vol. 15, no. 2, pp. 167–93, 2002.

101. Hussain, M., J. G. Hastings, and P. J. White, "Isolation and composition of the extracellular slime made by coagulase-negative staphylococci in a chemically defined medium," *J Infect Dis*, Vol. 163, no. 3, pp. 534–41, 1991.

102. Sutherland, I., "Biofilm exopolysaccharides: a strong and sticky framework," *Microbiology (Reading)*, Vol. 147, no. Pt 1, pp. 3–9, 2001.

103. Ica, T., V. Caner, O. Istanbullu, H. D. Nguyen, B. Ahmed, D. R. Call, and H. Beyenal, "Characterization of mono- and mixed-culture campylobacter jejuni biofilms," *Appl Environ Microbiol*, Vol. 78, no. 4, pp. 1033–8, 2012.

104. Gupta, P., S. Sarkar, B. Das, S. Bhattacharjee, and P. Tribedi, "Biofilm, pathogenesis and prevention—a journey to break the wall: a review," *Archives of Microbiology*, Vol. 198, no. 1, pp. 1–15, 2016.

105. Hall, C. W., and T. F. Mah, "Molecular mechanisms of biofilm-based antibiotic resistance and tolerance in pathogenic bacteria," *FEMS Microbiology Reviews*, Vol. 41, no. 3, pp. 276–301, 2017.

106. Joo, H. S., and M. Otto, "Molecular basis of in vivo biofilm formation by bacterial pathogens," *Chemistry & Biology*, Vol. 19, no. 12, pp. 1503–1513, 2012.

107. Decker, J. T., C. M. Magin, C. J. Long, J. A. Finlay, M. E. Callow, J. A. Callow, and A. B. Brennan, "Engineered antifouling microtopographies: An energetic model that predicts cell attachment," *Langmuir*, Vol. 29, no. 42, pp. 13023–13030, 2013.

108. Arciola, C. R., F. I. Alvi, Y. H. An, D. Campoccia, and L. Montanaro, "Implant infection and infection resistant materials: A mini review," *The International Journal of Artificial Organs*, Vol. 28, no. 11, pp. 1119–1125, 2005.

109. Percival, S. L., "Importance of biofilm formation in surgical infection," *British Journal of Surgery*, Vol. 104, no. 2, pp. e85–e94, 2017.

110. Shepard, J., W. Ward, A. Milstone, T. Carlson, J. Frederick, E. Hadhazy, and T. Perl, "Financial impact of surgical site infections on hospitals: The hospital management perspective," *JAMA Surgery*, Vol. 148, no. 10, pp. 907–914, 2013.

111. Harkins, C. P., B. Pichon, M. Doumith, J. Parkhill, H. Westh, A. Tomasz, H. de Lencastre, S. D. Bentley, A. M. Kearns, and M. T. G. Holden, "Methicillin-resistant staphylococcus aureus emerged long before the introduction of methicillin into clinical practice," *Genome biology*, Vol. 18, no. 1, pp. 130–130, 2017.

112. Davies, D., "Understanding biofilm resistance to antibacterial agents," *Nature Reviews Drug Discovery*, Vol. 2, no. 2, pp. 114–122, 2003.

113. Vickery, K., H. Hu, A. S. Jacombs, D. A. Bradshaw, and A. K. Deva, "A review of bacterial biofilms and their role in device-associated infection," *Healthcare infection*, Vol. 18, no. 2, pp. 61–66, 2013.

114. Hota, S., Z. Hirji, K. Stockton, C. Lemieux, H. Dedier, G. Wolfaardt, and M. A. Gardam, "Outbreak of multidrug-resistant pseudomonas aeruginosa colonization and infection secondary to imperfect intensive care unit room design," *Infection Control & Hospital Epidemiology*, Vol. 30, no. 1, pp. 25–33, 2009.

115. Dancer, S., "Importance of the environment in meticillin-resistant staphylococcus aureus acquisition: The case for hospital cleaning," *The Lancet infectious diseases*, Vol. 8, pp. 101–13, 2008.

116. Carling, P. C., and J. M. Bartley, "Evaluating hygienic cleaning in health care settings: what you do not know can harm your patients," *Am J Infect Control*, Vol. 38, no. 5 Suppl 1, pp. S41–50, 2010.

117. Dickinson, M. H., "Bionics: Biological insight into mechanical design," *Proceedings of the National Academy of Sciences*, Vol. 96, no. 25, p. 14208, 1999.

118. Junior, W. K., and A. S. Guanabara, "Methodology for product design based on the study of bionics," *Materials & design*, Vol. 26, no. 2, pp. 149–155, 2005.

119. Glinel, K., P. Thebault, V. Humblot, C. M. Pradier, and T. Jouenne, "Antibacterial surfaces developed from bio-inspired approaches," *Acta Biomaterialia*, Vol. 8, no. 5, pp. 1670–1684, 2012.

120. Petronis, S., K. Berntsson, J. Gold, and P. Gatenholm, "Design and microstructuring of pdms surfaces for improved marine biofouling resistance," *J Biomater Sci Polym Ed*, Vol. 11, no. 10, pp. 1051–72, 2000.

121. Sakamoto, A., Y. Terui, C. Horie, T. Fukui, T. Masuzawa, S. Sugawara, K. Shigeta, T. Shigeta, K. Igarashi, and K. Kashiwagi, "Antibacterial effects of protruding and recessed shark skin micropatterned surfaces of polyacrylate plate with a shallow groove," *FEMS Microbiology Letters*, Vol. 361, no. 1, pp. 10–16, 2014.

122. Xu, B., Q. Wei, M. R. Mettetal, J. Han, L. Rau, J. Tie, R. M. May, E. T. Pathe, S. T. Reddy, L. Sullivan, A. E. Parker, D. H. Maul, A. B. Brennan, and E. E. Mann, "Surface micropattern reduces colonization and medical device-associated infections," *J Med Microbiol*, Vol. 66, no. 11, pp. 1692–1698, 2017.

123. Liu, Q., L. Brookbank, A. Ho, J. Coffey, A. B. Brennan, and C. J. Jones, "Surface texture limits transfer of s. aureus, t4 bacteriophage, influenza b virus and human coronavirus," *PLOS ONE*, Vol. 15, no. 12, p. e0244518, 2020.

124. Mobini, S., C. A. Kuliasha, Z. A. Siders, N. A. Bohmann, S. M. Jamal, J. W. Judy, C. E. Schmidt, and A. B. Brennan, "Microtopographical patterns promote different responses in fibroblasts and schwann cells: A possible feature for neural implants," *Journal of Biomedical Materials Research Part A*, Vol. 109, no. 1, pp. 64–76, 2021.

125. Chien, H. W., X. Y. Chen, W. P. Tsai, and M. Lee, "Inhibition of biofilm formation by rough shark skin-patterned surfaces," *Colloids and Surfaces B: Biointerfaces*, Vol. 186, p. 110738, 2020.

126. Chien, H. W., X. Y. Chen, and W. P. Tsai, "Poly(methyl methacrylate)/titanium dioxide (pmma/tio2) nanocomposite with shark-skin structure for preventing biofilm formation," *Materials Letters*, Vol. 285, p. 129098, 2021.

127. Jang, H. H., J. S. Park, and B. Choi, "Flexible piezoresistive pulse sensor using biomimetic pdms mold replicated negatively from shark skin and pedot:pss thin film," *Sensors and Actuators A: Physical*, Vol. 286, pp. 107–114, 2019.

128. Lin, Y. T., Y. S. Ting, B. Y. Chen, Y. W. Cheng, and T. Y. Liu, "Bionic shark skin replica and zwitterionic polymer brushes functionalized pdms membrane for anti-fouling and wound dressing applications," *Surface and Coatings Technology*, Vol. 391, p. 125663, 2020.

129. Azad, A. K., N. Sermsintham, S. Chandrkrachang, and W. F. Stevens, "Chitosan membrane as a wound-healing dressing: Characterization and clinical application," *Journal of Biomedical Materials Research Part B: Applied Biomaterials*, Vol. 69B, no. 2, pp. 216–222, 2004.

130. Tabesh, E., H. Salimijazi, M. Kharaziha, and M. Hejazi, "Antibacterial chitosan-copper nanocomposite coatings for biomedical applications," *Materials Today: Proceedings*, Vol. 5, no. 7, Part 3, pp. 15806–15812, 2018.

131. Rabea, E. I., M. E. T. Badawy, C. V. S. G. Smagghe, and W. Steurbaut, "Chitosan as antimicrobial agent: Applications and mode of action," *Biomacromolecules*, Vol. 4, no. 6, pp. 1457–1465, 2003.

132. Anitha, A., S. Sowmya, P. T. S. Kumar, S. Deepthi, K. P. Chennazhi, H. Ehrlich, M. Tsurkan, and R. Jayakumar, "Chitin and chitosan in selected biomedical applications," *Progress in Polymer Science*, Vol. 39, no. 9, pp. 1644–1667, 2014.

133. Pranantyo, D., L. Q. Xu, E. T. Kang, and M. B. Chan-Park, "Chitosan-based peptidopolysaccharides as cationic antimicrobial agents and antibacterial coatings," *Biomacromolecules*, Vol. 19, no. 6, pp. 2156–2165, 2018.

134. Wu, M., R. Kempaiah, P. J. J. Huang, V. Maheshwari, and J. Liu, "Adsorption and desorption of dna on graphene oxide studied by fluorescently labeled oligonucleotides," *Langmuir*, Vol. 27, no. 6, pp. 2731–2738, 2011.

135. Suk, J. W., R. D. Piner, J. An, and R. S. Ruoff, "Mechanical properties of monolayer graphene oxide," *Langmuir*, Vol. 4, no. 11, pp. 6557–6564, 2010.

136. Li, J., X. Zeng, T. Ren, and E. V. der Heide, "The preparation of graphene oxide and its derivatives and their application in bio-tribological systems," *Lubricants*, Vol. 2, no. 3, 2014.

137. Eda, G., and M. Chhowalla, "Chemically derived graphene oxide: Towards large-area thin-film electronics and optoelectronics," *Advanced Materials*, Vol. 22, no. 22, pp. 2392–2415, 2010.

138. Barbolina, I., C. R. Woods, N. Lozano, K. Kostarelos, K. S. Novoselov, and I. S. Roberts, "Purity of graphene oxide determines its antibacterial activity," *2D Materials*, Vol. 3, no. 2, p. 025025, 2016.

139. Zhou, X., and Z. Liu, "A scalable, solution-phase processing route to graphene oxide and graphene ultralarge sheets," *Chemical Communications*, Vol. 46, no. 15, pp. 2611–2613, 2010.

140. Liu, S., T. H. Zeng, M. Hofmann, E. Burcombe, J. Wei, R. Jiang, J. Kong, and Y. Chen, "Antibacterial activity of graphite, graphite oxide, graphene oxide, and reduced graphene oxide: Membrane and oxidative stress," *ACS Nano*, Vol. 5, no. 9, pp. 6971–6980, 2011.

141. Natarajan, K., S. Singh, T. R. J. Burke, D. Grunberger, and B. B. Aggarwal, "Caffeic acid phenethyl ester is a potent and specific inhibitor of activation of nuclear transcription factor nf-kappa b," *Proc Natl Acad Sci U S A*, Vol. 93, no. 17, pp. 9090–5, 1996.

142. Yang, C., J. Wu, R. Zhang, P. Zhang, J. Eckard, R. Yusuf, X. Huang, T. G. Rossman, and K. Frenkel, "Caffeic acid phenethyl ester (cape) prevents transformation of human cells by arsenite (as) and suppresses growth of as-transformed cells," *Toxicology*, Vol. 213, no. 1-2, pp. 81–96, 2005.

143. Alici, O., H. S. Kavakli, C. Koca, N. D. Altintas, M. Aydin, and S. Alici, "Value of caffeic acid phenethyl ester pretreatment in experimental sepsis model in rats," *Mediators of Inflammation*, Vol. 2015, p. 810948, 2015.

144. Meyuhas, S., M. Assali, M. Huleihil, and M. Huleihel, "Antimicrobial activities of caffeic acid phenethyl ester," 2015.

145. Catauro, M., M. G. Raucci, D. de Marco, and L. Ambrosio, "Release kinetics of ampicillin, characterization and bioactivity of tio2/pcl hybrid materials synthesized by sol-gel processing," *J Biomed Mater Res A*, Vol. 77, no. 2, pp. 340–50, 2006.

146. Wu, J., C. Su, L. Jiang, S. Ye, X. Liu, and W. Shao, "Green and facile preparation of chitosan sponges as potential wound dressings," *ACS Sustainable Chemistry & Engineering*, Vol. 6, no. 7, pp. 9145–9152, 2018.

147. Zapata, M. E. V., J. H. M. Hernandez, C. D. G. Tovar, C. H. V. Llano, J. A. D. Escobar, B. Vázquez-Lasa, J. S. Román, and L. Rojo, "Novel bioactive and antibacterial acrylic bone cement nanocomposites modified with graphene oxide and chitosan," *Int J Mol Sci*, Vol. 20, no. 12, 2019.

148. Pandele, A. M., S. Dinescu, M. Costache, E. Vasile, C. Obreja, H. Iovu, and M. Ionita, "Preparation and in vitro, bulk, and surface investigation of chitosan/graphene oxide composite films," *Polymer Composites*, Vol. 34, no. 12, pp. 2116–2124, 2013.

149. Yuan, Y., P. Zhang, Y. Yang, X. Wang, and X. Gu, "The interaction of schwann cells with chitosan membranes and fibers in vitro," *Biomaterials*, Vol. 25, no. 18, pp. 4273–4278, 2004.

150. Su, J., Z. Du, L. Xiao, F. Wei, Y. Yang, M. Li, Y. Qiu, J. Liu, J. Chen, and Y. Xiao, "Graphene oxide coated titanium surfaces with osteoimmunomodulatory role to enhance osteogenesis," *Materials science & engineering. C, Materials for biological applications*, Vol. 113, p. 110983, 2020.

151. Kumar, S., and J. Koh, "Physiochemical and optical properties of chitosan based graphene oxide bionanocomposite," *International Journal of Biological Macromolecules*, Vol. 70, pp. 559–564, 2014.

152. Nanda, S. S., D. K. Yi, and K. Kim, "Study of antibacterial mechanism of graphene oxide using raman spectroscopy," *Scientific reports*, Vol. 6, no. 1, p. 28443, 2016.

153. Qian, X. W., N. Li, Q. Z. Wang, and S. C. Ji, "Chitosan/graphene oxide mixed matrix membrane with enhanced water permeability for high-salinity water desalination by pervaporation," *Desalination*, Vol. 438, pp. 83–96, 2018.

154. Wang, Z., A. A. Volinsky, and N. D. Gallant, "Crosslinking effect on polydimethylsiloxane elastic modulus measured by custom-built compression instrument," *Journal of Applied Polymer Science*, Vol. 131, no. 22, 2014.

155. Issa, Y., D. C. Watts, P. A. Brunton, C. M. Waters, and A. J. Duxbury, "Resin composite monomers alter mtt and ldh activity of human gingival fibroblasts in vitro," *Dental Materials*, Vol. 20, no. 1, pp. 12–20, 2004.

156. Salgado, C. L., E. M. S. Sanchez, J. F. Mano, and A. M. Moraes, "Characterization of chitosan and polycaprolactone membranes designed for wound repair application," *Journal of Materials Science*, Vol. 47, no. 2, pp. 659–667, 2012.

157. Rodrigues, S., M. Dionísio, C. R. López, and A. Grenha, "Biocompatibility of chitosan carriers with application in drug delivery," *J Funct Biomate*, Vol. 3, no. 3, pp. 615–41, 2012.

158. Hobro, A. J., and N. I. Smith, "An evaluation of fixation methods: Spatial and compositional cellular changes observed by raman imaging," *Vibrational Spectroscopy*, Vol. 91, pp. 31–45, 2017.

159. Campos, M. D., P. C. Zucchi, A. Phung, S. N. Leonard, and E. B. Hirsch, "The activity of antimicrobial surfaces varies by testing protocol utilized," *PLOS ONE*, Vol. 11, no. 8, pp. e0160728– e0160728, 2016.

160. Kun, E., and K. Marossy, "Evaluation methods of antimicrobial activity of plastics," *Materials Science Forum*, Vol. 729, pp. 430–435, 2013.

161. Trafny, E. A., R. Lewandowski, I. Zawistowska-Marciniak, and M. Stepinska, "Use of mtt assay for determination of the biofilm formation capacity of microorganisms in metalworking fluids," *World Journal of Microbiology and Biotechnology*, Vol. 29, no. 9, pp. 1635–1643, 2013.

162. Karakecili, A. G., T. T. Demirtas, C. Satriano, M. Gümüsderelioglu, and G. Marletta, "Evaluation of l929 fibroblast attachment and proliferation on arg-gly-asp-ser (rgds)-immobilized chitosan in serum-containing/serum-free cultures," *Journal of Bioscience and Bioengineering*, Vol. 104, no. 1, pp. 69–77, 2007.

163. Sangsanoh, P., O. Suwantong, A. Neamnark, P. Cheepsunthorn, P. Pavasant, and P. Supaphol, "In vitro biocompatibility of electrospun and solvent-cast chitosan substrata towards schwann, osteoblast, keratinocyte and fibroblast cells," *European Polymer Journal*, Vol. 46, no. 3, pp. 428–440, 2010.

164. Bagheripour, E., A. R. Moghadassi, S. M. Hosseini, B. V. der Bruggen, and F. Parvizian, "Novel composite graphene oxide/chitosan nanoplates incorporated into pes based nanofiltration membrane: Chromium removal and antifouling enhancement," *Journal of Industrial and Engineering Chemistry*, Vol. 62, pp. 311–320, 2018.

165. Liu, W., W. D. Wu, C. Selomulya, and X. D. Chen, "Uniform chitosan microparticles prepared by a novel spray-drying technique," *International Journal of Chemical Engineering*, Vol. 2011, p. 267218, 2011.

166. Rivero, S., M. A. García, and A. Pinotti, "Physical and chemical treatments on chitosan matrix to modify film properties and kinetics of biodegradation," *Journal of Materials Physics and Chemistry*, Vol. 1, no. 3, pp. 51–57, 2013.

167. Maraschin, T. G., R. d S Correa, L. F. Rodrigues, N. M. Balzarettid, J. A. Malmonge, G. B. Galland, and N. R. d S Basso, "Chitosan nanocomposites with graphene-based filler," *Materials Research*, Vol. 22, 2019.

168. Kumar, P., P. Huo, R. Zhang, and B. Liu, "Antibacterial properties of graphene-based nanomaterials," *Nanomaterials*, Vol. 9, no. 5, p. 737, 2019.

169. Hasan, J., S. Jain, R. Padmarajan, S. Purighalla, V. K. Sambandamurthy, and K. Chatterjee, "Multiscale surface topography to minimize adherence and viability of nosocomial drug-resistant bacteria," *Materials & design*, Vol. 140, pp. 332–344, 2018.

170. Helbig, R., D. Günther, J. Friedrichs, F. Rößler, A. Lasagni, and C. Werner, "The impact of structure dimensions on initial bacterial adhesion," *Biomaterials Science*, Vol. 4, no. 7, pp. 1074–1078, 2016.

171. Krishnamoorthy, K., N. Umasuthan, R. Mohan, J. Lee, and S. J. Kim, "Investigation of the antibacterial activity of graphene oxide nanosheets," *Science of Advanced Materials*, Vol. 4, no. 11, pp. 1111– 1117, 2012.

172. Mazaheri, M., O. Akhavan, and A. Simchi, "Flexible bactericidal graphene oxide–chitosan layers for stem cell proliferation," *Applied Surface Science*, Vol. 301, pp. 456–462, 2014.

173. Zhao, X., Z. Wei, Z. Zhao, Y. Miao, Y. Qiu, W. Yang, X. Jia, Z. Liu, and H. Hou, "Design and development of graphene oxide nanoparticle/chitosan hybrids showing ph-sensitive surface charge-reversible ability for efficient intracellular doxorubicin delivery," *ACS Applied Materials & Interfaces*, Vol. 10, no. 7, pp. 6608–6617, 2018.

174. Girase, B., J. S. Shah, and R. D. K. Misra, "Cellular mechanics of modulated osteoblasts functions in graphene oxide reinforced elastomers," *Advanced Engineering Materials*, Vol. 14, no. 4, pp. B101–B111, 2012.

175. Wilson, N. R., P. A. Pandey, R. Beanland, R. J. Young, I. A. Kinloch, L. Gong, Z. Liu, K. Suenaga, J. P. Rourke, S. J. York, and J. Sloan, "Graphene oxide: Structural analysis and application as a highly transparent support for electron microscopy," *ACS Nano*, Vol. 3, no. 9, pp. 2547–2556, 2009.

176. Francolini, I., E. Perugini, I. Silvestro, M. Lopreiato, A. S. d'Abusco, F. Valentini, E. Placidi, F. Arciprete, A. Martinelli, and A. Piozzi, "Graphene oxide oxygen content affects physical and biological properties of scaffolds based on chitosan/graphene oxide conjugates," *Materials*, Vol. 12, no. 7, p. 1142, 2019.

177. Gong, Y., Y. Yu, H. Kang, X. Chen, H. Liu, Y. Zhang, Y. Sun, and H. Song, "Synthesis and characterization of graphene oxide/chitosan composite aerogels with high mechanical performance," *Polymers*, Vol. 11, no. 5, p. 777, 2019.

178. Zhao, D., Q. Tian, M. Wang, and Y. Jin, "Study on the hydrophobic property of sharkskininspired micro-riblets," *Journal of Bionic Engineering*, Vol. 11, no. 2, pp. 296–302, 2014.

179. Bhushan, B., "Biomimetics inspired surfaces for drag reduction and oleophobicity/philicity," *Beilstein journal of nanotechnology*, Vol. 2, pp. 66–84, 2011.

180. Kim, T. W., "Simulation for contact angle of droplet on riblet surface," *Tribology and Lubricants*, Vol. 33, 2017.

181. May, R. M., M. G. Hoffman, M. J. Sogo, A. E. Parker, G. A. O'Toole, A. B. Brennan, and S. T. Reddy, "Micro-patterned surfaces reduce bacterial colonization and biofilm formation in vitro: Potential for enhancing endotracheal tube designs," *Clin Transl Med*, Vol. 3, p. 8, 2014.

182. Song, F., H. Koo, and D. Ren, "Effects of material properties on bacterial adhesion and biofilm formation," *J Dent Res*, Vol. 94, no. 8, pp. 1027–34, 2015.

183. Chang, Y. R., E. R. Weeks, and W. A. Ducker, "Surface topography hinders bacterial surface motility," *ACS Applied Materials & Interfaces*, Vol. 10, no. 11, pp. 9225–9234, 2018.

184. Gurunathan, S., J. W. Han, A. A. Dayem, V. Eppakayala, and J. H. Kim, "Oxidative stress-mediated antibacterial activity of graphene oxide and reduced graphene oxide in pseudomonas aeruginosa," *Int J Nanomedicine*, Vol. 7, pp. 5901–5914, 2012.

185. Zhang, Y., D. Zhai, M. Xu, Q. Yao, H. Zhu, J. Chang, and C. Wu, "3d-printed bioceramic scaffolds with antibacterial and osteogenic activity," *Biofabrication*, Vol. 9, no. 2, p. 025037, 2017.

186. Chaudhary, J. K., and P. C. Rath, "Microgrooved-surface topography enhances cellular division and proliferation of mouse bone marrow-derived mesenchymal stem cells," *PLOS ONE*, Vol. 12, no. 8, p. e0182128, 2017.

187. Zareidoost, A., M. Yousefpour, B. Ghaseme, and A. Amanzadeh, "The relationship of surface roughness and cell response of chemical surface modification of titanium," *Journal of Materials Science: Materials in Medicine*, Vol. 23, no. 6, pp. 1479–1488, 2012.

188. Rzepecka-Stojko, A., A. Kabala-Dzik, A. Mozdzierz, R. Kubina, R. D. Wojtyczka, R. Stojko, A. Dziedzic, Z. Jastrzebska-Stojko, M. Jurzak, E. Buszman, and J. Stojko, "Caffeic acid phenethyl ester and ethanol extract of propolis induce the complementary cytotoxic effect on triple-negative breast cancer cell lines," *Molecules*, Vol. 20, no. 5, 2015.

189. Wang, H., and M. Xu, "A biomimetic approach toward the fabrication of epithelial-like tissue," *In Bio-inspired Materials for Biomedical Engineering*, pp. 175–194, 2014.

190. Lieder, R., M. Darai, G. Orlygsson, and O. E. Sigurjonsson, "Solution casting of chitosan membranes for in vitro evaluation of bioactivity," *Biol Proced Online*, Vol. 15, no. 1, p. 11, 2013.

191. Ahmed, E. M., "Hydrogel: Preparation, characterization, and applications: A review," *Journal of Advanced Research*, Vol. 6, no. 2, pp. 105–121, 2015.

192. Bahram, M., N. Mohseni, and M. Moghtader, "An introduction to hydrogels and some recent applications," 2016.

193. Derman, S., "Caffeic acid phenethyl ester loaded plga nanoparticles: Effect of various process parameters on reaction yield, encapsulation efficiency, and particle size," *Journal of Nanomaterials*, Vol. 2015, p. 341848, 2015.

194. Zhang, D., S. Yang, Y. Chen, S. Liu, H. Zhao, and J. Gu, "(60)co -ray irradiation crosslinking of chitosan/graphene oxide composite film: Swelling, thermal stability, mechanical, and antibacterial properties," *Polymers*, Vol. 10, no. 3, p. 294, 2018.

195. Kiuchi, H., W. Kai, and Y. Inoue, "Preparation and characterization of poly(ethylene glycol) crosslinked chitosan films," *Journal of Applied Polymer Science*, Vol. 107, no. 6, pp. 3823–3830, 2008.

196. Matienzo, L. J., and S. K. Winnacker, "Dry processes for surface modification of a biopolymer: Chitosan," *Macromolecular Materials and Engineering*, Vol. 287, no. 12, pp. 871–880, 2002.

197. Fernández-Pan, I., K. Ziani, R. Pedroza-Islas, and J. I. Maté, "Effect of drying conditions on the mechanical and barrier properties of films based on chitosan," *Drying Technology*, Vol. 28, no. 12, pp. 1350– 1358, 2010.

198. Geninatti, T., G. Bruno, B. Barile, R. L. Hood, M. Farina, J. Schmulen, G. Canavese, and A. Grattoni, "Impedance characterization, degradation, and in vitro biocompatibility for platinum electrodes on biomems," *Biomedical Microdevices*, Vol. 17, no. 1, p. 24, 2015.

199. Smolińska, E., M. Moskot, J. Jakobkiewicz-Banecka, G. Wegrzyn, B. Banecki, A. Szczerkowska-Dobosz, D. Purzycka-Bohdan, and M. Gabig-Ciminska, "Molecular action of isoflavone genistein in the human epithelial cell line hacat," *PLOS ONE*, Vol. 13, no. 2, p. e0192297, 2018.

200. López-García, J., M. Lehocký, P. Humpolíček, and P. Sáha, "Hacat keratinocytes response on antimicrobial atelocollagen substrates: Extent of cytotoxicity, cell viability and proliferation," *J Funct Biomater*, Vol. 5, no. 2, pp. 43–57, 2014.

201. Toker, M., S. Rostami, M. Kesici, O. Gul, O. Kocaturk, S. Odabas, and B. Garipcan, "Decellularization and characterization of leek: a potential cellulose-based biomaterial," *Cellulose*, Vol. 27, no. 13, pp. 7331–7348, 2020.

202. Jella, K. K., S. Rani, L. O'Driscoll, B. McClean, H. J. Byrne, and F. M. Lyng, "Exosomes are involved in mediating radiation induced bystander signaling in human keratinocyte cells," *Radiat Res*, Vol. 181, no. 2, pp. 138–45, 2014.

203. Andrea, L., I. Marica, and R. Anamarija, "Lysozyme-induced degradation of chitosan: The characterisation of degraded chitosan scaffolds," *Journal of Tissue Repair and Regeneration*, Vol. 1, no. 1, pp. 12–22, 2017.

204. Mi, F. L., Y. C. Tan, H. C. Liang, R. N. Huang, and H. W. Sung, "In vitro evaluation of a chitosan membrane cross-linked with genipin," *Journal of Biomaterials Science, Polymer Edition*, Vol. 12, no. 8, pp. 835– 850, 2001.

205. Erdemli, H. K., S. Akyol, F. Armutcu, and O. Akyol, "The possible preventive effect of caffeic acid phenethyl ester (cape) against myringosclerosis," *Eur Arch Otorhinolaryngol*, Vol. 273, no. 3, pp. 789–90, 2016.

206. Kalinnikov, V. T., Z. A. Ezhova, N. A. Zakharov, and E. M. Koval', "Synthesis and physicochemical study of chitosan-containing calcium hydroxylapatites," *Russian Journal of Inorganic Chemistry*, Vol. 53, no. 3, pp. 357–361, 2008.

207. Queiroz, A. C., J. D. Santos, F. J. Monteiro, I. R. Gibson, and J. CKnowles, "Adsorption and release studies of sodium ampicillin from hydroxyapatite and glass-reinforced hydroxyapatite composites," *Biomaterials*, Vol. 22, no. 11, pp. 1393–1400, 2001.

208. Xu, Y., S. Sheng, X. Liu, C. Wang, W. Xiao, J. Wang, and F. A. Wu, "Cooperative reinforcement of ionic liquid and reactive solvent on enzymatic synthesis of caffeic acid phenethyl ester as an in vitro inhibitor of plant pathogenic bacteria," *Molecules*, Vol. 22, no. 1, 2017.

209. Venkatesan, J., R. Jayakumar, A. Mohandas, I. Bhatnagar, and S. K. Kim, "ntimicrobial activity of chitosan-carbon nanotube hydrogels," *Materials*, Vol. 7, pp. 3946–3955, 2014.

210. Erramilli, S., and J. Genzer, "Influence of surface topography attributes on settlement and adhesion of natural and synthetic species," *Soft Matter*, Vol. 15, no. 20, pp. 4045–4067, 2019.

211. Zhang, X., C. Huang, Y. Zhao, and X. Jin, "Ampicillin-incorporated alginate-chitosan fibers from microfluidic spinning and for vitro release," *Journal of Biomaterials Science, Polymer Edition*, Vol. 28, no. 13, pp. 1408–1425, 2017.

212. Nijampatnam, B., D. H. Nadkarni, H. Wu, and S. E. Velu, "Antibacterial and antibiofilm activities of makaluvamine analogs," *Microorganisms*, Vol. 2, no. 3, pp. 128–39, 2014.

213. Alves, P., J. M. Moreira, J. M. Miranda, and F. J. Mergulhão, "Analysing the initial bacterial adhesion to evaluate the performance of antifouling surfaces," *Antibiotics*, Vol. 9, no. 7, 2020.

214. Edmiston, J. C., C. Krepel, R. Marks, P. Rossi, J. Sanger, M. Goldblatt, M. B. Graham, S. Rothenburger, J. Collier, and G. Seabrook, "Microbiology of explanted suture segments from infected and non-infected surgical cases," *Journal of Clinical Microbiology*, Vol. 51, 2012.

215. Ercan, U. K., F. Ibis, C. Dikyol, N. Horzum, O. Karaman, C. Yıldırım, E. Cukur, and E. A. Demirci, "Prevention of bacterial colonization on non-thermal atmospheric plasma treated surgical sutures for control and prevention of surgical site infections," *PLOS ONE*, Vol. 13, no. 9, pp. e0202703–e0202703, 2018.

216. Bhore, S. J., and F. H. Shah, "Construction of efficient and effective transformation vectors for palmitoyl-acyl carrier protein thioesterase gene silencing in oil palm," *Bioinformation*, Vol. 6, no. 6, pp. 212–220, 2011.

217. Varma, R., and S. Vasudevan, "Extraction, characterization, and antimicrobial activity of chitosan from horse mussel modiolus modiolus," *ACS Omega*, Vol. 5, no. 32, pp. 20224–20230, 2020.

218. Xu, P., H. Uyama, J. E. Whitten, S. Kobayashi, and D. L. Kaplan, "Peroxidase-catalyzed in situ polymerization of surface orientated caffeic acid," *J Am Chem Soc*, Vol. 127, no. 33, pp. 11745–53, 2005.

219. Divya, K., D. Rana, S. Alwarappan, M. S. S. A. Saraswathi, and A. Nagendran, "Investigating the usefulness of chitosan based proton exchange membranes tailored with exfoliated molybdenum disulfide nanosheets for clean energy applications," *Carbohydrate Polymers*, Vol. 208, pp. 504–512, 2019.

220. Doğan, M., "Preparation of chitosan nanoparticles and characterization studies," *Cumhuriyet Medical Journal*, 2020.

221. Vijayalakshmi, V., P. A. H. Kousar, and D. Sukhi, "Optimization and characterization of chitosan based nanocarrier for the application of cancer drug delivery," *JCR*, Vol. 7, no. 7, p. 762, 2020.

222. Xu, J., N. Cai, W. Xu, Y. Xue, Z. Wang, Q. Dai, and B. Yu, "Mechanical enhancement of nanofibrous scaffolds through polyelectrolyte complexation," *Nanotechnology*, Vol. 24, p. 025701, 2012.

223. Ciro, Y., J. Rojas, J. Oñate-Garzon, and C. H. Salamanca, "Synthesis, characterisation and biological evaluation of ampicillin–chitosan–polyanion nanoparticles produced by ionic gelation and polyelectrolyte complexation assisted by high-intensity sonication," *Polymers*, Vol. 11, no. 11, p. 1758, 2019.

224. Ignatova, M., N. Manolova, I. Rashkov, and N. Markova, "Antibacterial and antioxidant electrospun materials from poly(3-hydroxybutyrate) and polyvinylpyrrolidone containing caffeic acid phenethyl ester – "in" and "on" strategies for enhanced solubility," *International Journal of Pharmaceutics*, Vol. 545, no. 1, pp. 342–356, 2018.

225. Arasoglu, T., S. Derman, and B. Mansuroglu, "Comparative evaluation of antibacterial activity of caffeic acid phenethyl ester and plga nanoparticle formulation by different methods," *Nanotechnology*, Vol. 27, no. 2, p. 025103, 2015.

226. Lee, H. S., S. Y. Lee, S. H. Park, J. H. Lee, S. K. Ahn, Y. M. Choi, D. J. Choi, and J. H. Chang, "Antimicrobial medical sutures with caffeic acid phenethyl ester and their in vitro/in vivo biological assessment," *MedChemComm*, Vol. 4, no. 5, pp. 777–782, 2013.

227. Takaisi-Kikuni, N. B., and H. Schilcher, "Electron microscopic and microcalorimetric investigations of the possible mechanism of the antibacterial action of a defined propolis provenance," *Planta Med*, Vol. 60, no. 3, pp. 222–227, 1994.

228. Damiri, Y., Y. Bachra, C. Bounacir, A. Laaraibi, and M. Berrada, "Synthesis and characterization of lyophilized chitosan-based hydrogels cross-linked with benzaldehyde for controlled drug release," *Journal of Chemistry*, Vol. 2020, p. 8747639, 2020.

229. Gull, N., S. M. Khan, M. T. Z. Butt, S. Khalid, M. Shafiq, A. Islam, S. Asim, S. Hafeez, and R. U. Khan, "In vitro study of chitosan-based multi-responsive hydrogels as drug release vehicles: a preclinical study," *RSC Advances*, Vol. 9, no. 53, pp. 31078–31091, 2019.

230. VanEpps, J. S., and J. G. Younger, "Implantable device-related infection," *Shock*, Vol. 46, no. 6, pp. 597–608, 2016.

231. Wang, J., P. Bhargava, Y. Yu, A. N. Sari, H. Zhang, N. Ishii, K. Yan, Z. Zhang, Y. Ishida, K. Terao, S. C. Kaul, E. Miyako, and R. Wadhwa, "Novel caffeic acid phenethyl ester-mortalin antibody nanoparticles offer enhanced selective cytotoxicity to cancer cells," *Cancers*, Vol. 12, no. 9, 2020.

232. Su, Z. Z., J. Lin, M. Prewett, N. I. Goldstein, and P. B. Fisher, "Apoptosis mediates the selective toxicity of caffeic acid phenethyl ester (cape) toward oncogene-transformed rat embryo fibroblast cells," *Anticancer Res*, Vol. 15, no. 5b, pp. 1841–8, 1995.

233. Zhou, D., and X. Weng, "A novel butylated caffeic acid derivative protects hacat keratinocytes from squalene peroxidation-induced stress," *Skin Pharmacology and Physiology*, Vol. 32, no. 6, pp. 307–317, 2019.

234. Lee, Y. J., P. H. Liao, W. K. Chen, and C. C. Yang, "Preferential cytotoxicity of caffeic acid phenethyl ester analogues on oral cancer cells," *Cancer Letters*, Vol. 153, no. 1, pp. 51–56, 2000.

235. Lim, K. M., S. Bae, J. E. Koo, E. S. Kim, O. N. Bae, and J. Y. Lee, "Suppression of skin inflammation in keratinocytes and acute/chronic disease models by caffeic acid phenethyl ester," *Archives of Dermatological Research*, Vol. 307, no. 3, pp. 219–227, 2015.

236. Ferraz, R., J. Costa-Rodrigues, M. H. Fernandes, M. M. Santos, I. M. Marrucho, L. P. Rebelo, C. Prudencio, J. P. Noronha, Z. Petrovski, and L. C. Branco, "Antitumor activity of ionic liquids based on ampicillin," *ChemMedChem*, Vol. 10, no. 9, pp. 1480–3, 2015.

237. Balupillai, A., R. P. Nagarajan, K. Ramasamy, K. Govindasamy, and G. Muthusamy, "Caffeic acid prevents uvb radiation induced photocarcinogenesis through regulation of pten signaling in human dermal fibroblasts and mouse skin," *Toxicology and Applied Pharmacology*, Vol. 352, pp. 87–96, 2018.

238. Kuo, S. M., S. J. Chang, T. W. Chen, and T. C. Kuan, "Guided tissue regeneration for using a chitosan membrane: an experimental study in rats," *J Biomed Mater Res A*, Vol. 76, no. 2, pp. 408–15, 2006.

239. Yasayan, G., "Chitosan films and chitosan/pectin polyelectrolyte complexes encapsulating silver sulfadiazine for wound healing," *stanbul Journal of Pharmacy*, Vol. 50, 2020.

240. El-Sherbiny, I. M., and H. D. Smyth, "Novel cryomilled physically cross-linked biodegradable hydrogel microparticles as carriers for inhalation therapy," *J Microencapsul*, Vol. 27, no. 8, pp. 657–68, 2010.